FINAL REPORT

Project Title: Adaptive Nodal Transport Methods for Reactor Transient Analysis

Covering Period: June 4, 2001 through June 3, 2005

Date of Report: August 31, 2005

Recipient: Purdue University
400 Central Drive, West Lafayette, Ind 47907-1290

Award Number: DE-FG07-01ID14106

Subcontractors:

Other Partners: E. Lewis

Contact(s): T. Downar, 765-494-5752, downar@ecn.purdue.edu

Project Objective: Develop methods for adaptively treating the angular, spatial, and time dependence of the neutron flux in reactor transient analysis. These methods were demonstrated in the DOE transport nodal code VARIANT and the US NRC spatial kinetics code, PARCS.

Background: The work proposed here was to investigate methods that will allow higher order, multigroup transport methods to be used for practical reactor transient analysis. The first phase of the work performed during FY2002 was the development of adaptive PN methods and the initial work on error estimation methods. The second phase of the work performed during FY2003 was to develop optimal preconditioning and to implement the adaptive methods in PARCS and VARIANT for both cartesian and cylindrical geometries. Some modification of the work scope was necessary when it became apparent that the current formulation of the nodal transport equations in PARCS and VARIANT were numerically unstable when adaptive methods were applied. During the past year work focused on the development of stable nodal transport methods in PARCS and VARIANT. The final phase of the work to be performed in the Fall '04 will be to verify and validate the codes using established benchmark problems.

Status: The following final report is submitted to describe the work performed under this contract. The first part of the report describes the work performed on the PARCS code and the second part of the report describes the work performed on the VARIANT code and the comparison of the results from the two codes.

PART I: ADAPTIVE NEUTRON TRANSPORT METHODS IN PARCS

1. Introduction

The diffusion approximation has successfully been used for the analysis of the current generation of Light Water Reactors (LWRs) because the transport equation is very costly to solve for reactor core-sized problems. During the past twenty years advanced nodal methods such as the nodal expansion method (NEM) [Finnemann, 1977], the analytic nodal method (ANM) or the nodal integration method (NIM) [Fischer, 1981], and the analytic function expansion method (AFEN) [Noh, 1995] have been successfully developed to spatially discretize the diffusion equation. These coarse-mesh or nodal approaches were preferred in order to save CPU time and memory. Considerable effort had been invested in improving the accuracy of nodal methods and these advanced nodal methods became capable of estimating an eigenvalue within tens of pcm with a fuel assembly size of nodes. During the past few years, however, there has been some concern that the methods that have been developed for uranium fueled LWRs do not perform satisfactorily when applied to the same cores fueled with Mixed Oxide (MOX), or more generally to cores with very heterogeneous loadings. Several researchers carefully examined the source of the large errors in modeling heterogeneous core configurations.

The specific approximations which contribute to the errors observed in nodal diffusion methods can be identified into four primary effects: a spatial discretization effect, a spatial homogenization effect, a group collapsing effect, and a transport effect. The quantification analysis of the four effects under various possible environments is very important to isolate the source of errors and to provide direction for improving in core calculations. In the analysis here the spatial discretization effect is not included since it has been well investigated by many researchers. Instead, the analysis will focus on group, transport, and spatial homogenization effects.

2. Background Study

In order to analyze the three effects, TWODANT, the Los Alamos discrete ordinate transport code [Alcouffe, 1995], is utilized. The conventional diffusion and simplified P_3 (SP_3) methods are also used for comparison, which will be described in detail later. Fuel combinations such as UOX/UOX show small spectrum changes, and the diffusion approximation is still accurate in these configurations. In this thesis very different materials in characteristics are used such as MOX, reflector (water) or UOX with large amounts of neutron absorber. The various geometry configurations used are shown in Figs. 2.1 through 2.5. The compositions and geometries tested are mainly based on possible combinations of the KAIST benchmark problem which will be discussed in detail in Chapter 8. The geometry in Fig. 2.1 is somehow not realistic, but it will assist in verifying what happens in core peripheries where there are interfaces between fuels and reflector. In Fig. 2.2, MOX and UOX are neighboring as often seen in MOX

loaded reactors, and in Fig. 2.3 the same geometry is used as in a diagonal direction of the KAIST benchmark core. Fig. 2.4 is the same as Fig. 2.3 except that it is composed of many different pins. The two-dimensional configuration in Fig. 2.5 will be used to examine the spatial heterogeneity effect.

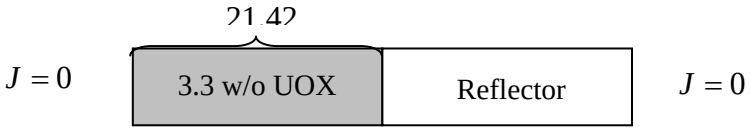

Figure 2.1 1-D Geometry Configuration of Case A

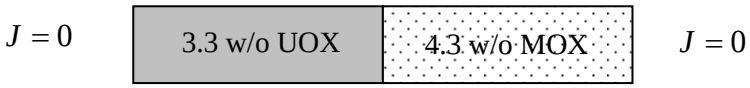

Figure 2.2 1-D Geometry Configuration of Case B

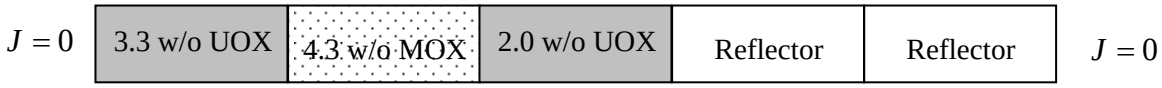

Figure 2.3 1-D Geometry Configuration of Case C

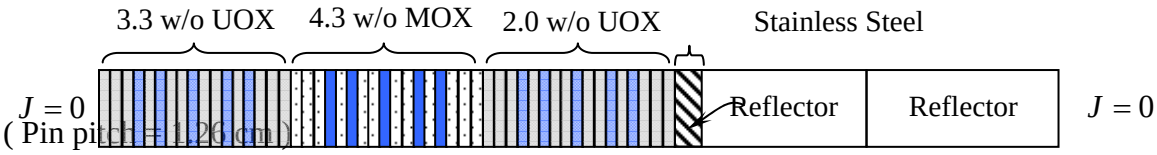

Figure 2.4 1-D Geometry Configuration of Case D (Heterogeneous Pins)

The tests performed here are summarized in Table 2.1. For the transport effect, Cases A through D have been tested changing the order of the angular approximation in the S_N and P_N methods. For the group effect, 7-group cross sections are condensed to 4 and 2 groups in single fuel assembly calculations with zero-current boundary conditions, which is a conventional method of homogenization. For the spatial homogenization, two-dimensional heterogeneous fuel assemblies (FAs) shown in Fig. 2.5 are homogenized in the same manner used for the group homogenization. The assembly discontinuity factor (ADF) is also calculated to account for the discrepancy between homogeneous and heterogeneous configurations, which is also one of the conventional procedures. Note that since there is no theoretical discrepancy between P_N and SP_N in one-dimensional geometry, SP_N is meaningful only for Case E.

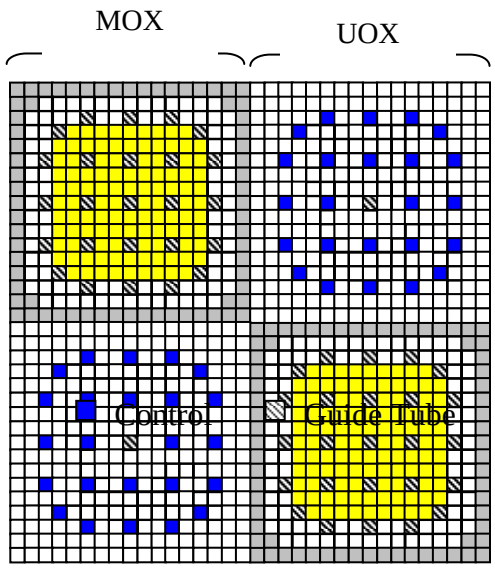

MOX (boundary: 4.3w/o, middle: 7.0 w/o, center: 8.7 w/o)
UOX (3.3 w/o + B_4C Control Rods)

Figure 2.5 2-D Geometry Configuration of Case E

Table 2.1 Test Cases for Separate Effects

Effect	Description	Case
Transport	Change the order of angles only (S_{16}, P_1, SP_3) (7-G homogeneous cross sections)	A, B, C, D
Group Homogenization	Change the number of groups only (S_{16}) (2, 4, 7 groups homogeneous cross sections)	B (w/ different composition)
Spatial Homogenization	Change the spatial configurations only (S_{16}, P_1, SP_3) (7-G homogeneous, heterogeneous cross sections)	E

Transport Effect

Brantley and Larsen performed some tests with the modified OECD-L336 MOX benchmark problem for the transport effect and showed ~33 pcm and 1.68 % errors between S_{16} and P_1 in eigenvalue and average assembly power, respectively; ~11 pcm and 0.16 % between S_{16} and SP_3 [Brantley, 2000]. According to their results, the transport effect, which can be estimated from the errors between S_{16} and P_1, is not that large, but it showed that SP_3 has very good agreement with S_{16}.

As summarized in Table 2.2, the difference of eigenvalues between S_{16} and P_1 is over 840 pcm in Cases A and D and are 50 pcm and 68 pcm in Cases B and C, respectively. These differences are reduced to less than 100 pcm or a few pcm when using P_3. Even though Cases A and D show much larger deviations in P_1 calculations, it should be noted that these conditions are somewhat different from practical conditions. Pin powers resulting from SP_3 are also reduced to one-half or one-third of the P_1 results. Figs. 2.6, 2.7, and 2.8 show power distributions and differences of P_1 and P_3 from S_{16} for the cases discussed here.

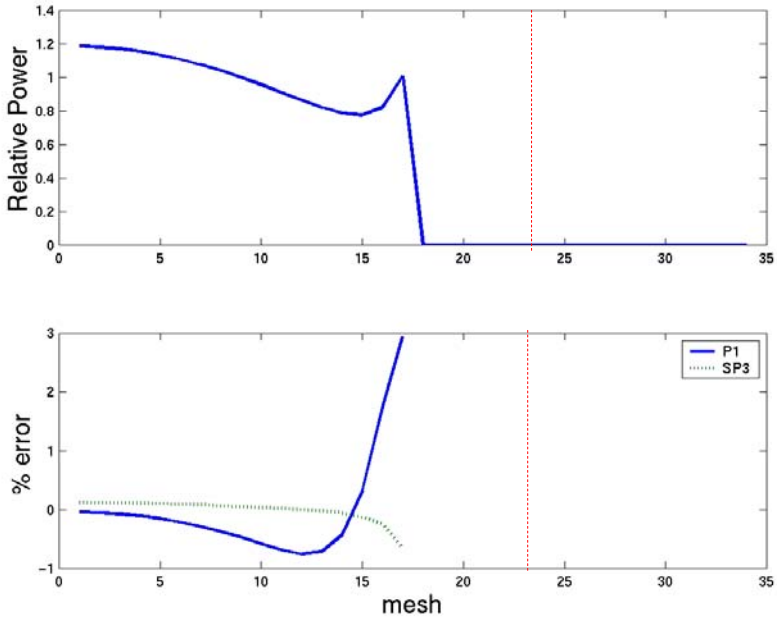

Figure 2.6 Power Difference of P_1 and SP_3 Methods againt S_{16} (Case A)

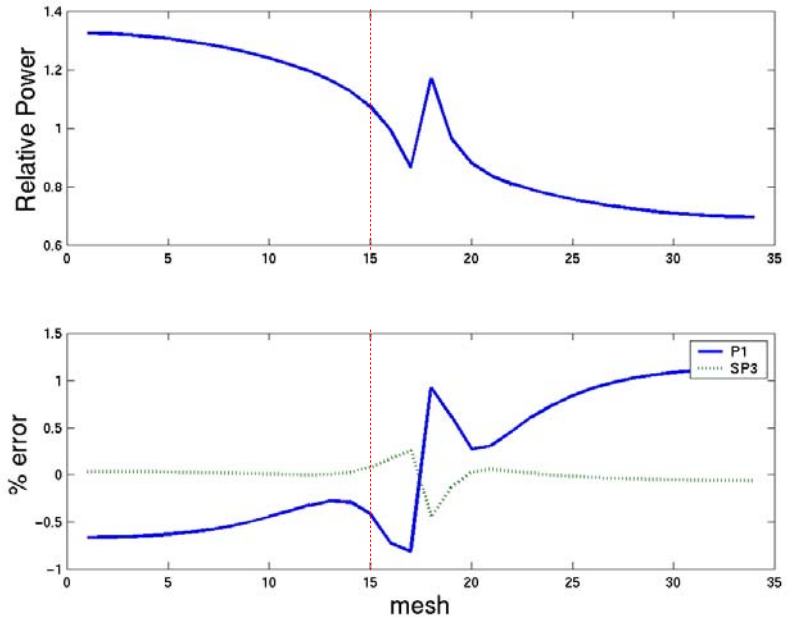

Figure 2.7 Power Difference of P_1 and SP_3 Methods againt S_{16} (Case B)

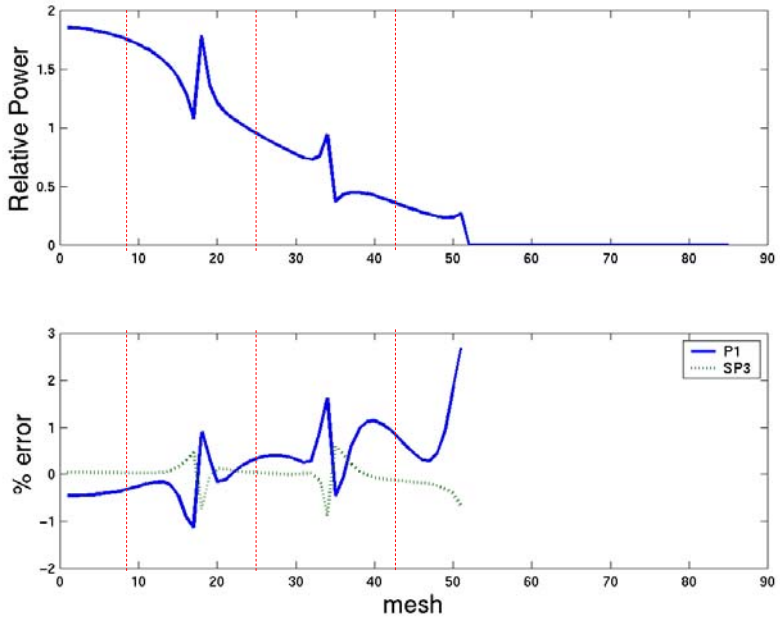

Figure 2.8 Power Difference of P_1 and SP_3 Methods againt S_{16} (Case C)

Table 2.2 Comparison of Eigenvalue and Powers for Transport Effects

CASE		**Eigenvalue** (Δpcm)	**% Error of Local Power**	
			RMS	**Maximum**
CASE A	**S_{16}**	1.07110	**-**	**-**
	P_1	(-879)	**0.9**	**2.9**
	SP_3	(-47)	**0.2**	**-0.7**
CASE B	**S_{16}**	1.18499	**-**	**-**
	P_1	(-50)	**0.7**	**1.1**
	SP_3	(-4)	**0.1**	**0.5**
CASE C	**S_{16}**	1.17265	**-**	**-**
	P_1	(-68)	**0.7**	**2.7**

	SP_3	(-2)	**0.3**	**0.9**
CASE D	**S_{16}**	0.81368	**-**	**-**
	P_1	(-840)	**4.1**	**12.6**
	SP_3	(-121)	**1.3**	**5.2**

*** 7-group calculation**

Group Effect

Palmtag discussed energy group homogenization in his thesis and quantified the errors caused by the spectral differences between UOX and MOX [Palmtag, 1997]. According to his results, eigenvalue errors ranged from 200 to 500 pcm; assembly power errors between 1 % and 2 %, and pin-power errors between 2.6 % and 4.6 % in 2-group calculations. The similar tests have been performed here with Case B changing enrichments. The trends shown in Tables 2.3 and 2.4 are somehow consistent to his results even though the magnitude of errors is a little smaller. In Table 2.3, 97-group S_2 calculations are used as references for 8-group, 4-group, and 2-group calculations. Note that a 8-group structure is used just for this analysis instead of a 7-group one because 7 group results are often not distinguishable from 2-group results. Fig. 2.9 illustrates the energy cutoffs used in condensing groups here. Eigenvalue errors are ranging from 100 to 300 pcm in 2-group calculations. In Table 2.4 in which the configuration of Case B is used as it is, group condensing is performed from 7 to 2 groups using S_{16} 7-group fluxes of single fuel assembly geometry with zero-current boundary condition. Since this is a specific case in which a FA with 2.0 w/o UOX and a FA zoned with 4.3 w/o, 7.3 w/o and 8.7 w/o Pu-total are neighboring, it shows an eigenvalue difference of 73 pcm and RMS and maximum pin power errors of 1.2 % and 2.4 %, respectively, in 2-group calculations.

Spatial Homogenization Effect

The spatial homogenization effect can be seen in Table 2.5. In order to see the spatial homogenization effect only, the same number of energy groups (7 groups) is used for both heterogeneous and homogeneous calculations. The results show that just the spatial homogenization causes an error of 500 ~ 800 pcm without any consideration of the assembly discontinuity factor (ADF). However, when the ADF is used, the eigenvalue error is reduced to less than 100 pcm and assembly power errors become very smaller, especially, in the SP_3 calculation. The discontinuity factor was first proposed by Koebke to preserve the reaction rates between heterogeneous and homogeneous geometries based upon the equivalence theory [Keobke, 1980], and it was later generalized to the assembly discontinuity factor [Smith, 1986]. The results

note that the ADF is essential to preserving good accuracy when using homogenized cross sections. It is well defined for the diffusion approximation, but not for the SP_N approximation. Details of the ADF for the SP_N approximation will also be discussed in Appendix B. The results show that P_1 or SP_3 calculation with the ADF has very good agreement in terms of eigenvalue and assembly power. Even though they are not shown in the table, the error of local pin powers reconstructed by the modulation technique should be discussed together with assembly average power.

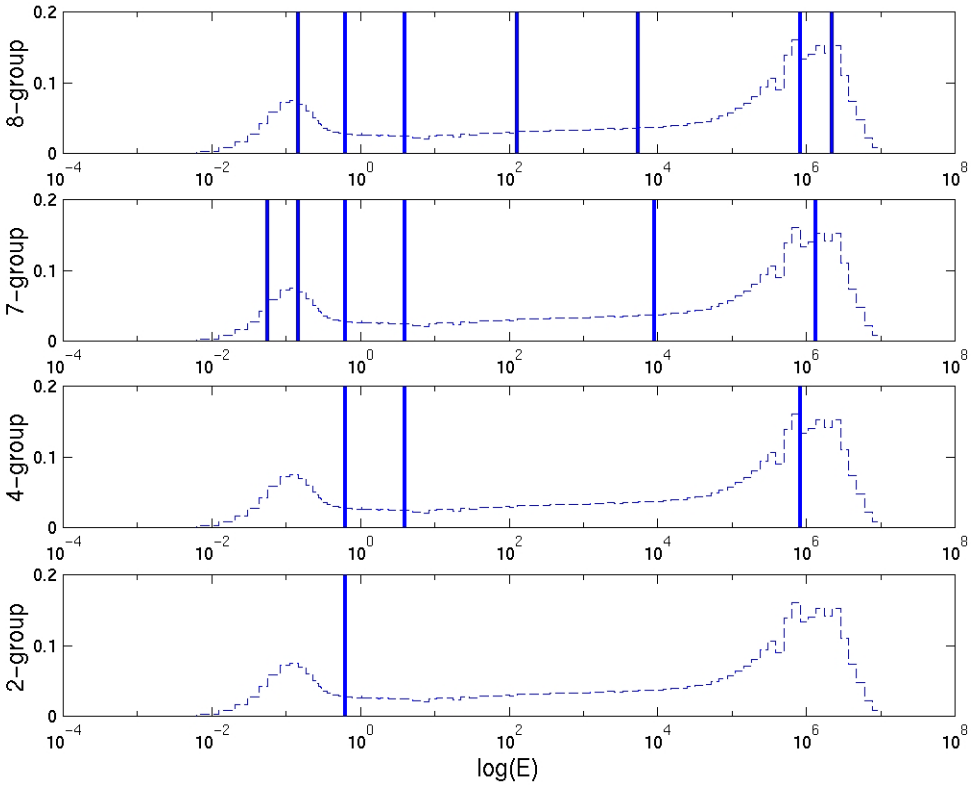

Figure 2.9 Energy Cutoffs for Group Condensation

Table 2.3 Comparison of Eigenvalue with Change of MOX and UOX Enrichments

Energy	UOX	MOX		
		4 w/o	8 w/o	12 w/o
8-Group	2 w/o	34*	55	39
	3 w/o	13	37	44
	4 w/o	51	51	57
	5 w/o	65	60	58
4-Group	2 w/o	22	26	2
	3 w/o	55	26	28
	4 w/o	82	60	63
	5 w/o	107	80	76
2-Group	2 w/o	87	138	188
	3 w/o	157	141	212
	4 w/o	222	194	261
	5 w/o	271	229	285

*** Δpcm from 97-group S_2 calculation**

Table 2.4 Comparison of Eigenvalue and Powers for Group Effects (Case B)

Group	Eigenvalue (Δk-eff, pcm)	% Error of Local Power	
		RMS	Maximum
7	1.14319	-	-
2	(73)	1.2	2.4

* S_{16} calculation

Table 2.5 Comparison of Spatial Homogenization Effects (Case E)

Configuration		Eigenvalue (Δk-eff, pcm)	% Error of FA Average Power	
			RMS	**Maximum**
S_{16}		1.03373	**-**	**-**
P_1	**HET**	(-1009)	-	-
	HOM (No ADF)	(-786)	5.6	7.2
	HOM (ADF)	(-90)	**0.9**	**1.1**
SP_3	**HET**	(52)	**-**	**-**
	HOM (No ADF)	(-490)	**3.7**	**4.8**
	HOM (ADF)	(60)	**0.01**	**-0.01**

* HET: Heterogeneous cross section, HOM: Homgeneous cross section
* difference : pcm

2.2 Motivation

According to the qualitative analyses for MOX-loaded test problems performed in the previous section it can be concluded that group homogenization and transport effects cause substantial errors in terms of eigenvalue and power, and spatial homogenization is more related to the loss of accuracy in estimating local pin powers. Therefore, the transport, group, and spatial homogenization effects need to be more accurately approximated in very heterogeneous cores. Even though there have been many ad-hoc methods to reduce errors, more fundamental remedies are necessary to effectively treat various core conditions. One possibility is to explicitly use the multigroup transport equation with heterogeneous geometry. As shown in the results, the SP_3 approximation includes most of the transport effect. Other researchers have also shown the simililar results with respect to the SP_3 approximation [Larsen, 1996], [Brantley, 2000], [Mengelle, 1999], [Tatsumi, 2000]. Therefore, with current computational power, the multigroup SP_3 approximation with heterogeneous geometry can be considered as a viable option to achieve the most accurate results within reasonable computation time. Even though the accuracy gain from the multigroup pin-by-pin SP_3 calculation is small for some cases, it would still be meaningful in that the near-reference solution for steady-state and transient conditions can be achived.

However, the multigroup pin-by-pin SP_3 calculation is still very costly particularly when solving the transient problem. The motivation of the work here is to identify methods that make

it practical to perform steady-state and transient caculations using the multigroup SP_3 approximation with heterogeneous geometry.

The conventional methods to solve the multigroup pin-by-pin equation are the fine-mesh finite difference method (FDM) with efficient linear solvers such as Krylov subspace methods and some acceleration methods such as Chebyshev, coarse-mesh rebalacing (CMR), and multi-grid methods. In the work here, the multi-level acceleration based upon the global/local iteration is introduced and coupled with the multigroup pin-by-pin SP_3 formulation to show better performance compared to the conventional methods.

3. NEUTRON TRANSPORT EQUATION

The methods used to solve the transport equations can be categorized as either stochastic or deterministic methods. While a stochastic method implies using the Monte Calro method, a deterministic method can involve either differential or integral methods depending upon the manner to deal with the angular variable. There are several alternative methods in integral transport methods: collision probability method, characteristics method, etc. The differenial transport method typically implies either the spherical hamonics method (P_N) or the discrete ordinate method (S_N). Each method has some advantages and disadvantages, but among them the differential transport methods are most commomly used for practical large-scale reactor problems due to computational efficiency.

In this section, the P_N method is briefly introduced; it starts with one-dimensional geometry since it is useful to obtain analytic insight in the nature of the solution of the transport equation.

3.1 P_N Method

The Boltzmann transport equation was proposed more than one century ago to describe dilute gases. It is also very useful to describe neutron transport behavior [Duderstadt, 1979]. The following is the Boltzmann neutron transport equation without an external neutron source in the steady state:

$$\Omega \cdot \nabla \psi(r,\Omega,E) + \Sigma_t(r,E)\psi(r,\Omega,E) = \int d\Omega' \int dE' \Sigma_s(r,\Omega' \to \Omega, E' \to E)\psi(r,\Omega',E') + \frac{1}{4\pi} S_f(r,E), \quad (3.1)$$

where $S_f(r,E) = \chi(E)\int dE' \nu\Sigma_f(r,E')\phi(r,E')$, $\phi(r,E) = \int d\Omega' \psi(r,\Omega',E)$.

The equation above can be solved with the spherical harmonics method (P_N) which is developed by expansion of the angular flux and the differential scattering cross sections in Legendre polynomials [Henry, 1975]:

$$\psi(r,\Omega,E)=\sum_{n=0}^{\infty}\sum_{m=-n}^{n}\phi_n^m(r,E)Y_n^m(\Omega), \tag{3.2}$$

where $Y_n^m(\Omega)=Y_n^m(\theta,\varphi)=\left[\frac{(2n+1)(n-m)!}{(n+m)!}\right]^{1/2}P_n^m(\mu)\exp(im\varphi)$,

$P_n^m(\mu)=$ associated Legendre polynomials, $\mu=\cos\theta$.

Using the orthogonal property of the spherical harmonics, the coefficients of Eq. (3.2) are determined as:

$$\phi_n^m(r,E)=\int d\Omega Y_n^m(\Omega)\psi(r,\Omega,E). \tag{3.3}$$

Since the angular flux is independent of the azimuthal angle in a one-dimensional geometry, the angular flux can be expressed as:

$$\Omega\cdot\nabla\psi(r,\Omega,E)\rightarrow\mu\frac{\partial}{\partial x}\psi(r,\Omega,E), \tag{3.4}$$

Therefore, the form of the P_N method can be easily introduced using a one-dimensional form written as follows:

$$\mu\frac{\partial\psi(x,\mu,E)}{\partial x}+\Sigma_t(x,E)\psi(x,\mu,E)= \int d\Omega'\int dE'\,\Sigma_s(x,\Omega'\cdot\Omega,E'\rightarrow E)\psi(x,\mu',E')+\frac{1}{2}S_f(x,E), \tag{3.5}$$

where $S_f(x,E)=\chi(E)\int dE'\,\nu\Sigma_f(x,E')\phi(x,E')$,

$\Omega'\cdot\Omega=\mu_0=\cos\theta_0=\cos\theta\cos\theta'-\sin\theta\sin\theta'\cos(\varphi-\varphi')$.

And the following coefficients are determined by using the orthogonal property of Legendre polynomials:

$$\phi_n(x,E) = \int d\mu \psi(x,\mu,E) P_n(\mu), \tag{3.6}$$

$$\Sigma_{sn}(x,E' \to E) = 2\pi \int d\mu_0 \Sigma_s(x,\mu_0,E' \to E) P_n(\mu_0), \tag{3.7}$$

where $P_n(\mu_0) = P_n(\mu)P_n(\mu') + 2\sum_{m=1}^{n} \frac{(n-m)!}{(n+m)!} P_n^m(\mu) P_n^m(\mu') \cos(m(\varphi - \varphi'))$.

Therefore, Eq.(3.5) is rewritten using moments and Legendre polynomials as:

$$\begin{aligned} \mu \frac{\partial}{\partial x} \sum_{n=0}^{N} \frac{(2n+1)}{2} P_n(\mu)\phi_n(x,E) + \Sigma_t(x,E) \sum_{n=0}^{N} \frac{(2n+1)}{2} P_n(\mu)\phi_n(x,E) = \\ \int dE' \sum_{n=0}^{N} \frac{(2n+1)}{2} \Sigma_{sn}(x,E' \to E) P_n(\mu)\phi_n(x,E') + \frac{1}{2} S_f(x,E). \end{aligned} \tag{3.8}$$

Using the recursion relationship of the Legendre polynomials:

$$(2n+1)\mu P_n(\mu) = (n+1)P_{n+1}(\mu) + nP_{n-1}(\mu), \tag{3.9}$$

One can arrive at (N+1) sets of coupled partial differential equations for the expansion coefficients $\phi_n(x,E)$:

$$\begin{aligned} \frac{(n+1)}{(2n+1)} \frac{\partial \phi_{n+1}(x,E)}{\partial x} + \frac{n}{(2n+1)} \frac{\partial \phi_{n-1}(x,E)}{\partial x} + \Sigma_t(x,E)\phi_n(x,E) \\ = \int dE' \Sigma_{sn}(x,E' \to E)\phi_n(x,E') + \frac{\delta_{0n}}{2} S_f(x,E). \end{aligned} \tag{3.10}$$

For convenience in deriving multi-group one-dimensional P_N equations, the energy ranges are divided into G discrete intervals. Eq. (3.10) can be rewritten with these discrete groups:

$$\begin{aligned} \frac{(n+1)}{(2n+1)} \frac{d\phi_{n+1g}(x)}{dx} + \frac{n}{(2n+1)} \frac{d\phi_{n-1g}(x)}{dx} + \Sigma_{tng}(x)\phi_{ng}(x) \\ = \sum_{g'} \Sigma_{sngg'}(x)\phi_{ng'}(x) + \frac{\delta_{0n}}{2} S_{fg}(x), \end{aligned} \tag{3.11}$$

where $\phi_{ng}(x) = \int_g \phi_n(x,E)dE$, $\Sigma_{tng}(x) = \dfrac{\int_g \Sigma_t(x,E)\phi_n(x,E)dE}{\phi_{ng}(x)}$,

$$\Sigma_{sngg'}(x) = \frac{\int_g dE \int_{g'} \Sigma_{sn}(x, E' \to E)\phi_n(x,E')dE'}{\phi_{ng'}(x)}, \quad \nu\Sigma_{fg}(x) = \frac{\int_g \nu\Sigma_f(x,E)\phi(x,E)dE}{\phi_g(x)}.$$

While all cross sections in the first P_N equation are flux weighted, an exact calculation of total and scattering cross sections of the higher P_N equations requires that $\phi_n(x,E)$ with $n>0$ be known. Instead of introducing different total cross sections in all moment equations, Σ_{t0g}, which is weighted by flux, is used in the left hand side of the higher moment equations. Modification of diagonal elements of scattering cross sections is then required:

$$\Sigma'_{sngg}(x) = \Sigma_{sngg}(x) - (\Sigma_{tng}(x) - \Sigma_{t0g}(x)). \tag{3.12}$$

Then, Eq. (3.11) can be written as:

$$\frac{(n+1)}{(2n+1)}\frac{d\phi_{n+1g}(x)}{dx} + \frac{n}{(2n+1)}\frac{d\phi_{n-1g}(x)}{dx} + \Sigma_{rng}(x)\phi_{ng}(x) = \sum_{g' \neq g} \Sigma_{sngg'}(x)\phi_{ng'}(x) + \frac{\delta_{0n}}{2} S_{fg}(x). \tag{3.13}$$

where $\Sigma_{rng}(x) = \Sigma_{t0g}(x) - \Sigma'_{sngg}(x)$.

A reflective boundary condition obviously requires that all odd moments of the flux vanish:

$$\phi_n(x_s, E) = 0, \quad for\ odd\ n, \tag{3.14}$$

where x_s is x at a surface.

The exact interface condition of continuity of angular flux cannot be satisfied exactly by the flux approximation for infinite N. Therefore, the first N+1 Legendre moments of this relation are required to be satisfied:

$$\phi_n(x_s^-, E) = \phi_n(x_s^+, E),\ n = 0,1,2,...,N, \tag{3.15}$$

where x_s^+ and x_s^- are x from right or left side of a surface s, respectively.

3.2 Multidimensional Simplified P_N Method

The original approach of the SP_N approximation is a simple generalization of the one-dimensional P_N equations to the multidimensional P_N equations. The result is (N+1)-coupled SP_N equations in the three-dimensional geometry. First of all, a procedure for producing three-dimensional P_1 equations from the one-dimensional P_1 equations can be defined as follows:

1) Replace the operator $\partial / \partial x$ in the one-dimensional $n = 0$ equation with the divergence operator ∇,
2) Replace the operator $\partial / \partial x$ in the one-dimensional $n = 1$ equation with the gradient operator ∇,
3) Consider the zeroth-order Legendre moment of the angular flux ϕ_0 as a scalar,
4) Consider the first-order Legendre moment of the angular flux ϕ_1 as a vector.

For the SP_N equations, the relations of P_1 between one-dimensional and multi-dimensional geometries are extrapolated to P_N when N > 1.

1) Replace the operator $\partial / \partial x$ in the one-dimensional equation for even n with the divergence operator ∇,
2) Replace the operator $\partial / \partial x$ in the one-dimensional equation for odd n with the gradient operator ∇,
3) Consider the even-order Legendre moments of the angular flux as scalars,
4) Consider the odd-order Legendre moments of the angular flux as vectors.

With the procedure above, the final form is obtained as:

$$\frac{(n+1)}{(2n+1)} \nabla \cdot \phi_{n+1} + \frac{n}{(2n+1)} \nabla \cdot \phi_{n-1} + \Sigma_t \phi_n = s_n, \quad \text{n = even,} \tag{3.16a}$$

$$\frac{(n+1)}{(2n+1)} \nabla \phi_{n+1} + \frac{n}{(2n+1)} \nabla \phi_{n-1} + \Sigma_t \phi_n = s_n, \quad \text{n = odd.} \tag{3.16b}$$

The general matrix form of the SP_N equations is shown in Eq. (3.17). Their boundary conditions can also be obtained from those for the one-dimensional P_N equations. The advantages of the SP_N equations are that inspite of some approximations in their formulation they have significantly improved computational efficiency compared to the S_N method or the original P_N method, and they maintain the rotational invariance of the P_N equations which the S_N eqautions do not have.

$$\begin{bmatrix} \Sigma_{r0} & \nabla\cdot & & & & & & & \\ \frac{1}{3}\nabla & \Sigma_{t1} & \frac{2}{3}\nabla & & & & & & \\ & \frac{2}{5}\nabla\cdot & \Sigma_{t2} & \frac{3}{5}\nabla\cdot & & & & & \\ & & \frac{3}{7}\nabla & \Sigma_{t3} & \frac{4}{7}\nabla & & & & \\ & & & \frac{4}{9}\nabla\cdot & \Sigma_{t4} & \frac{5}{9}\nabla\cdot & & & \\ & & & & \frac{5}{11}\nabla & \Sigma_{t5} & \frac{6}{11}\nabla & & \\ & & & & & \cdot & & \cdot & \\ & & & & & & \cdot & & \cdot \\ & & & & & & & \frac{N}{2N+1}\nabla & \Sigma_{tN} \end{bmatrix} \begin{bmatrix} \phi_0 \\ \phi_1 \\ \phi_2 \\ \phi_3 \\ \phi_4 \\ \phi_5 \\ \cdot \\ \cdot \\ \cdot \\ \phi_N \end{bmatrix} = \begin{bmatrix} s_0 \\ s_1 \\ s_2 \\ s_3 \\ s_4 \\ s_5 \\ \cdot \\ \cdot \\ \cdot \\ s_N \end{bmatrix} . \quad (3.17)$$

Note that N is normally odd, and accordingly N-1 becomes even. The number of first-order differential equations is reduced by one-half in second-order differential equations with the assumption of $s_i = 0$ $(i \geq 1)$. For simplicity, Eq. (3.17) can be reduced to (N+1)/2 number of second-order differential equations as shown in Eq. (3.18).

It should be noted that the general SP_N equations are asymptotic corrections to the P_1 theory. For planar geometry problems, these corrections exactly reduce to the P_N equations. In practice, the SP_N equations are most accurate for problems that are reasonably close to being diffusive in nature or for problems that have strong transport regions in which the solution behaves nearly one-dimensionally and has weak tangential derivatives at material interfaces. However, for problems that have strong multidimensional transport effects, such as voids, streaming regions, or geometically complex spatial inhomogeneous, the SP_N solutions are less accurate [Larsen, 1996].

$$\begin{bmatrix} b_0 & c_0 & & & & & & & & \\ a_2 & b_2 & c_2 & & & & & & & \\ & a_4 & b_4 & c_4 & & & & & & \\ & & \cdot & \cdot & \cdot & & & & & \\ & & & \cdot & \cdot & \cdot & & & & \\ & & & & a_n & b_n & c_n & & & \\ & & & & & \cdot & \cdot & \cdot & & \\ & & & & & & \cdot & \cdot & \cdot & \\ & & & & & & & \cdot & \cdot & \cdot \\ & & & & & & & & a_{N-1} & b_{N-1} \end{bmatrix} \begin{bmatrix} \phi_0 \\ \phi_2 \\ \phi_4 \\ \cdot \\ \cdot \\ \phi_n \\ \cdot \\ \cdot \\ \cdot \\ \phi_{N-1} \end{bmatrix} = \begin{bmatrix} s_0 \\ 0 \\ 0 \\ \cdot \\ \cdot \\ 0 \\ \cdot \\ \cdot \\ \cdot \\ 0 \end{bmatrix}, \qquad (3.18)$$

where $b_0 = -D_1\nabla^2 + \Sigma_r$, $c_0 = -2D_1\nabla^2$,

$$a_2 = -\frac{2}{5}D_1\nabla^2,\ b_2 = -\left(\frac{4}{5}D_1 + \frac{3}{5}D_3\right)\nabla^2 + \Sigma_{t2},\ c_2 = -\frac{4}{5}D_3\nabla^2,$$

$$a_n = -\frac{n}{2n-1}D_{n-1}\nabla^2,\ b_n = -\left(\frac{n^2}{(2n+1)(n-1)}D_{n-1} + \frac{n+1}{2n+1}D_{n+1}\right)\nabla^2 + \Sigma_{tn},$$

$$c_n = -\frac{n+2}{2n+1}D_{n+1}\nabla^2,$$

$$D_m \equiv \frac{m}{(2m+1)\Sigma_{tm}},\quad m = odd\ \ number,\ n = even\ number.$$

4. NONLINEAR FORMULATION OF THE SP_3 EQUATION

4.1 Nonlinear Approach

Smith first introduced the nonlinear iteration method to reduce the computer memory storage requirement and to increase the computational efficiency [Smith, 1983]. The global problem is solved with the coarse-mesh finite difference (CMFD) method while the local calculation is performed based on the "two-node" problem. From the higher-order acurate solution with the "two-node" problem, the correction factor can be computed at every node interface to construct the following CMFD formulation:

$$J^g_{i,i+1} = -\tilde{D}^g_{i,i+1}(\phi^g_{i+1} - \phi^g_i) - \hat{D}^g_{i,i+1}(\phi^g_{i+1} + \phi^g_i), \qquad (4.1)$$

where $\tilde{D}^g_{i,i+1} = \dfrac{2D_i D_{i+1}}{(D_i + D_{i+1})\Delta}$, Δ = node size.

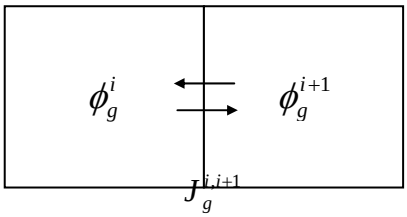

Figure 4.1 Two-Node Calculation

Aragones and Ahnert proposed an interesting idea which is basically the same as Smith but uses the interface flux discontinuity factor (IFDF) instead of the additive correction term shown in Eq. (4.1) [Aragones, 1986]. Their CMFD formulation is somewhat different:

$$J^g_{i,i+1} = -\alpha^g_{i,i+1}(r^g_{i,i+1}\phi^g_{i+1} - \phi^g_i), \tag{4.2}$$

where $r^g_{i,i+1} = \dfrac{f^g_i}{f^g_{i+1}}$, $\alpha^g_{i,i+1} = \dfrac{2D^g_i D^g_{i+1}}{(D^g_i r^g_{i,i+1} + D^g_{i+1})\Delta}$.

The IFDF here accounts for the difference between coarse mesh and fine mesh, the so-called coarse-mesh effect, as well as the difference between the homogeneous geometry and the heterogeneous geometry, the so-called heterogeneity effect. Another distinction from the Smith's formulation is that the local problem is constructed not with "two-node" but with "one-node". They have a correction factor per interface in common.

Recently, Moon, et al. suggested the so-called "two-node two-factor" approach which uses two correction factors from each side at an interface [Moon, 1999]. The correction factors are calculated based on the "two-node" problem which uses the higher-order solution.

$$J^g_{i,i+1} = -\tilde{\tilde{D}}^g_{i,i+1}(\phi^g_{i+1} - \phi^g_i) - \hat{\tilde{D}}^g_{i,i+1}(\phi^g_{i+1} + \phi^g_i), \tag{4.3}$$

where $\tilde{\tilde{D}}^g_{i,i+1} = \dfrac{2(D^g_i D^g_{i+1} + \hat{D}^g_i \hat{D}^g_{i+1})}{(D^g_i + D^g_{i+1} - \hat{D}^g_i + \hat{D}^g_{i+1})\Delta}$, $\hat{\tilde{D}}^g_{i,i+1} = \dfrac{2(D^g_i \hat{D}^g_{i+1} + \hat{D}^g_i D^g_{i+1})}{(D^g_i + D^g_{i+1} - \hat{D}^g_i + \hat{D}^g_{i+1})\Delta}$.

This is similar to the Smith's idea in the sense of using the "two-node" problem and is similar to the Aragones' idea in the way that it defines the two correction factors.

Shin, et al. presented the "one-node two-factor" idea which is based on the same equation as in Eq. (4.3) [Shin, 1999]. The distinction from the Moon's approach is that the two correction factors for each interface are calculated based on the "one-node" problem instead of the "two-node" problem, which is similar to the Aragones' formulation. However, this is distinguished from the Aragones' approach in that it uses the partial incoming currents as boundary conditions for the "one-node" problem.

To summarize nonlinear formulations historically, they are basically the same in the sense that they are correcting the neutron current term so that the CMFD current is equivalent to the reference current which is determined by the higher-order nodal methods or the fine-mesh finite difference methods. The principle distinction among the formulations is that some use one correction factor and some use two correction factors, and some calculate corrections factors with the "one-node" problem and some obtain correction factors with the "two-node" problem. Of course, the boundary condition for the local problem is different depending upon the type of local problem used (i.e. "one-node" or "two-node"). No matter which method is used in the local problem, it is obvious that they all construct a simple CMFD matrix in the global problem which can be easily solved with higher-order accuracy. Each has its own advantages and disadvantages compared to the others. For example, the "one-node" as a local problem is better than the "two-node" in terms of computation efficiency, but it is relatively less stable compared to the "two-node" in terms of convergence. One correction factor might be better than two factors in that the "one-factor" equation, Eq. (4.1), requires a smaller number of floating operations and has a smaller number of degrees of freedom to determine the CMFD diffusion coefficients compared to the "two-factor" equation. However, even though the "two-node" approach is free to use either the "one-factor" method or the "two-factor" method, the "one-node" approach is limited to using the two correction factors because the partial current boundary condition should be determined with two degrees of freedoms. In this report, the "one-node two-factor" approach is chosen since it provides a convenient combination of computational efficiency for the implementation of SP_3 as will be described in the next section.

However, it is first worthwhile to first examine Aragones' nonlinear formulation in more detail. Even though it appears to use the "one-node one-factor" approach, it actually employs the "one-node two-factor" approach to provide the interface flux boundary conditions in the local problem as in Shin's formulation. As mentioned already, the differences between the two approaches are a form of correction factors which yield a different form of the CMFD current equation and boundary conditions for the local problem. In his paper, Aragones discussed a linear discontinuous finite difference formulation which allows the accurate and stable reduction in directions (transport to diffusion), spatial mesh (fine to coarse mesh), and groups (multigroup to few or one group). Unlike other approaches, the IFDF is used to correct the current instead of the additional corrective term, which includes both the coarse-mesh effect and the heterogeneity effect.

It is also interesting to examine the stability condition for the interface correction factors. The IFDF is defined as:

$$r_{i,i+1}^{g} = \frac{\phi_i^g - h_i J_{i,i+1}^g / 2D_i^g}{\phi_{i+1}^g + h_{i+1} J_{i,i+1}^g / 2D_{i+1}^g}. \tag{4.4}$$

Based on the concept that convergence and stability of the iterative solution of the linear equations are preserved as long as the diagonal dominance is preserved, α of Eq. (4.2) and $r_{i,i+1}^g$ of Eq. (4.4) should be non-negative and bounded:

$$\alpha_{i,i+1}^g > 0\,, \quad r_{i,i+1}^g > 0\,. \tag{4.5}$$

As a result, the following condition can be imposed as a lower bound for the averaged diffusion coefficients for each node and group:

$$D_i^g > \frac{h_i}{2\phi_i^g} \max(-J_{i-1,i}^g,\, J_{i,i+1}^g)\,, \tag{4.6}$$

where $J_{i-1,i}^g$ = current for group g at a left surface of a node i,

$J_{i,i+1}^g$ = current for group g at a right surface of a node i.

It is noted in the Aragones' paper that the lower bound for diffusion coefficients with respect to currents and fluxes are always fulfilled in PWR calculations. This bounding analysis of diffusion coefficients can be applied to the other approaches as will be discussed later for SP_3.

Overall, the correction factors are defined depending upon the global and local configurations, as shown in Fig. 4.2. For example, the correction factor, f_h, connects a heterogenous geometry to a homogeneous one; f_s, fine-mesh to coarse-mesh; f_g, many groups to a few groups; f_a, transport to diffusion. In the conventional two-group calculation, normally the heterogeneity and group factors, $f_h * f_g$, are calculated off-line in a single fuel assembly configuration with the name of the assembly discontinuity factor (ADF). The spatial correction factor, f_s, is calculated on-line during the global/local iteration for acceleration, which corresponds to $\hat{D}$ in the previous discussion.

The nonlinear global/local method has been successfully applied to the diffusion equation by several other researchers. In this report, the application is expanded to the transport problem. In the following sections, the formulations of the multidimensional SP_3 method are briefly discribed for steady-state and transient conditions, and then the nonlinear formulations are discussed on the basis of the "one-node two-factor" approach.

Parameter	Configuration	Correction Factor
Heterogeneity	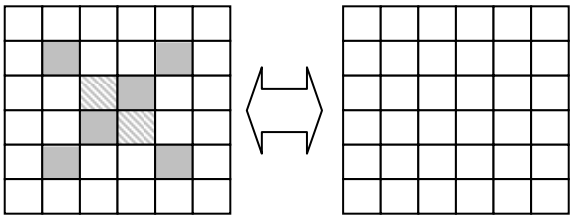 heterogeneous homogeneous	f_h
Space	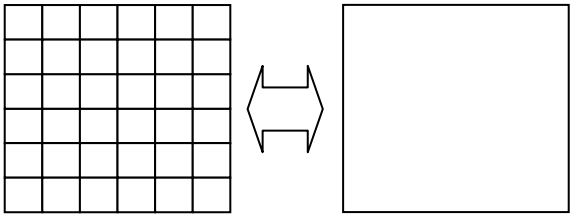 fine-mesh or higher-order One-mesh	f_s
Group	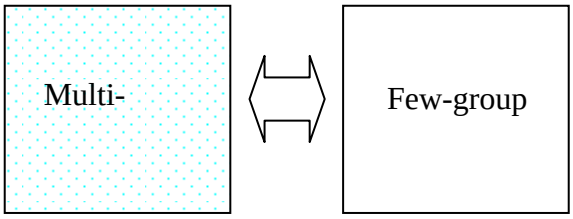 Multi- Few-group	f_g
Angle	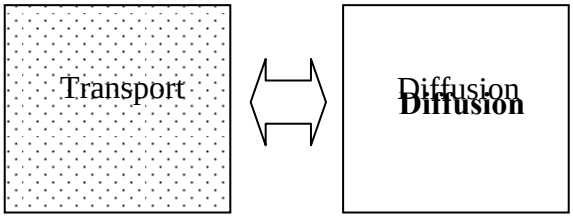 Transport Diffusion **Diffusion**	f_a

4.2 Two-Dimensional SP_3 Equation

4.2.1 Steady State Equation

The governing equations of the multidimensional SP_3 equation can be written as discussed in Section 3.2 with truncation of orders higher than three:

$$\nabla \cdot \phi_{1g} + \Sigma_{rg}\phi_{0g} = s_{0g}, \tag{4.7a}$$

$$\frac{2}{3}\nabla \phi_{2g} + \frac{1}{3}\nabla \phi_{0g} + \Sigma_{trg}\phi_{1g} = 0, \tag{4.7b}$$

$$\frac{3}{5}\nabla \cdot \phi_{3g} + \frac{2}{5}\nabla \cdot \phi_{1g} + \Sigma_{tg}\phi_{2g} = 0, \tag{4.7c}$$

$$\frac{3}{7}\nabla \phi_{2g} + \Sigma_{tg}\phi_{3g} = 0, \tag{4.7d}$$

where $s_{0g} = \sum_{g'} \Sigma_{sg'g}\phi_{0g'} + \frac{\chi_g}{k_{eff}} \sum_{g'} \nu\Sigma_{fg'}\phi_{0g'}$.

The most common methods used for a direct solution for the SP_N equations involve the elimination of odd-order angular moments to yield a set of coupled diffusion-like equations as shown below in a matrix-equation form in a given group:

$$\begin{bmatrix} -D_1\nabla^2 + \Sigma_r & -2D_1\nabla^2 \\ -\frac{2}{5}D_1\nabla^2 & -\left(\frac{3}{5}D_3 + \frac{4}{5}D_1\right)\nabla^2 + \Sigma_t \end{bmatrix} \begin{bmatrix} \phi_0 \\ \phi_2 \end{bmatrix} = S_0 \begin{bmatrix} 1 \\ 0 \end{bmatrix}, \tag{4.8}$$

where $D_1 \equiv \frac{1}{3\Sigma_{tr}}$, $D_3 \equiv \frac{3}{7\Sigma_t}$.

These are simply two coupled diffusion equations that can readily be solved with standard diffusion computer codes with appropriately defined diffusion coefficients.

For SP_3 boundary conditions, the Marshark boundary condition can be used in the same way as in P_1. For example, the equations for a right boundary become:

$$j_l^+ = \int_0^1 d\mu\, P_l(\mu)\psi(x_r, \mu), \quad j_l^- = \int_0^{-1} d\mu\, P_l(\mu)\psi(x_r, \mu), \tag{4.9}$$

where x_r = right surface, $\psi(x, \mu) = \sum_{l=0}^{3} \frac{(2l+1)}{2} P_l(\mu)\phi_l(x)$,

$$P_0(\mu)=1,\ P_1(\mu)=\mu,\ P_2(\mu)=\frac{1}{2}(3\mu^2-1),\ P_3(\mu)=\frac{1}{2}(5\mu^3-3\mu).$$

Applying P_1 and P_3 to Eq. (4.9) leads to the relationship between partial currents, surface fluxes and net currents:

$$j_1^{\pm}=\frac{1}{4}\phi_{0s}\pm\frac{1}{2}J_1+\frac{5}{16}\phi_{2s},\quad j_3^{\pm}=\frac{5}{16}\phi_{2s}\pm\frac{1}{2}J_3-\frac{1}{16}\phi_{0s}, \tag{4.10}$$

which have the additional contribution of the other moment unlike the boundary conditions of the P_1 equation.

4.2.2 Transient Equation

The time-dependent SP_3 equations are basically the same as Eq. (4.7) except for the additional time derivative terms in each equation:

$$\frac{1}{\upsilon}\frac{\partial\phi_{0g}}{\partial t}+\nabla\cdot\phi_{1g}+\Sigma_{rg}\phi_{0g}=s_{0tg}, \tag{4.11a}$$

$$\frac{1}{\upsilon}\frac{\partial\phi_{1g}}{\partial t}+\frac{2}{3}\nabla\phi_{2g}+\frac{1}{3}\nabla\phi_{0g}+\Sigma_{trg}\phi_{1g}=0, \tag{4.11b}$$

$$\frac{1}{\upsilon}\frac{\partial\phi_{2g}}{\partial t}+\frac{3}{5}\nabla\cdot\phi_{3g}+\frac{2}{5}\nabla\cdot\phi_{1g}+\Sigma_{tg}\phi_{2g}=0, \tag{4.11c}$$

$$\frac{1}{\upsilon}\frac{\partial\phi_{3g}}{\partial t}+\frac{3}{7}\nabla\phi_{2g}+\Sigma_{tg}\phi_{3g}=0, \tag{4.11d}$$

$$\frac{dC_k}{dt}=-\lambda_k C_k+\frac{\beta}{k_{eff}}\sum_{g'}\nu\Sigma_{fg'}\phi_{0g'}, \tag{4.11e}$$

where $s_{0tg}=\sum_{g'}\Sigma_{sg'g}\phi_{0g'}+\frac{\chi_g}{k_{eff}}(1-\beta)\sum_{g'}\nu\Sigma_{fg'}\phi_{0g'}+\chi_{dg}\sum_{k'}\lambda_k C_k$,

$\frac{dC_k}{dt}=-\lambda_k C_k+\frac{\beta}{k_{eff}}\sum_{g'}\nu\Sigma_{fg'}\phi_{0g'}$.

Similarly in the steady-state equation, inserting Eq. (4.11b) into Eq. (4.11a), and Eqs. (4.11b) and (4.11d) into Eq. (4.11c) yields the two time-dependent 2nd-order differential equations:

$$-\frac{1}{\upsilon\Sigma_{trg}}\frac{\partial}{\partial t}\left(\nabla\cdot\phi_{1g}\right)+\frac{1}{\upsilon}\frac{\partial\phi_{0g}}{\partial t}-\nabla\cdot\left(2D_{0g}\nabla\phi_{2g}+D_{0g}\nabla\phi_{0g}\right)+\Sigma_{rg}\phi_{0g}=s_{0tg}, \tag{4.12a}$$

$$-\frac{3}{5}\frac{1}{\upsilon\Sigma_{tg}}\frac{\partial}{\partial t}\left(\nabla\cdot\phi_{3g}\right)-\frac{2}{5}\frac{1}{\upsilon\Sigma_{trg}}\frac{\partial}{\partial t}\left(\nabla\cdot\phi_{1g}\right)+\frac{1}{\upsilon}\frac{\partial\phi_{2g}}{\partial t}$$
$$-\nabla\cdot\left(\frac{3}{5}D_2\nabla\phi_{2g}+\frac{4}{5}D_{0g}\nabla\phi_{2g}+\frac{2}{5}D_{0g}\nabla\phi_{0g}\right)+\Sigma_{tg}\phi_{2g}=0. \quad (4.12b)$$

As indicated in Eq. (4.12), time derivatives of divergences of the 1st- and 3rd-moments, which are the change of leakages of 0th- and 2nd-moments with time, are additional terms to be considered, compared to the conventional time-dependent diffusion equation.

In an actual calculation, the following equations are used with appropriate time discretization. Together with inserting the time derivative term $\left(\partial/\upsilon\partial t\right)^{n+1}$ into Σ^*_{sg}, the term s_{0tg} on the right hand side is also modified with the time derivative term $\left(\partial/\upsilon\partial t\right)^{n}$. Using the fully implicit method with the time indices, Eq. (4.11) can then be written as:

$$\nabla\cdot\phi_{1g}^{n+1}+\Sigma^*_{rg}\phi_{0g}^{n+1}=s_{0tg}^{n+1}+q_{0g}^{n}, \quad (4.13a)$$
$$\frac{2}{3}\nabla\phi_{2g}^{n+1}+\frac{1}{3}\nabla\phi_{0g}^{n+1}+\Sigma^*_{trg}\phi_{1g}^{n+1}=q_{1g}^{n}, \quad (4.13b)$$
$$\frac{3}{5}\nabla\cdot\phi_{3g}^{n+1}+\frac{2}{5}\nabla\cdot\phi_{1g}^{n+1}+\Sigma^*_{tg}\phi_{2g}^{n+1}=q_{2g}^{n}, \quad (4.13c)$$
$$\frac{3}{7}\nabla\phi_{2g}^{n+1}+\Sigma^*_{tg}\phi_{3g}^{n+1}=q_{3g}^{n}, \quad (4.13d)$$

where $\Sigma^*_{sg}=\Sigma_{sg}+\dfrac{1}{\upsilon\Delta t}$, $q_{ig}^{n}=\dfrac{1}{\upsilon}\dfrac{\phi_{ig}^{n}}{\Delta t}$,

$$s_{0tg}^{n+1}=\frac{1}{\upsilon_g\Delta t}\phi_{0g}^{n}+\sum_{g'}\Sigma_{sg'g}\phi_{0g'}^{n+1}+\frac{\chi_g}{k_{eff}}(1-\beta)\sum_{g'}\nu\Sigma_{fg'}\phi_{0g'}^{n+1}+\chi_{dg}\sum_{k'}\lambda_k C_k^{n+1}.$$

Eq. (4.13) can be reduced to the two second-order differential equations similar to the steady-state equations:

$$-\nabla\cdot\left(\frac{2}{3\Sigma^*_{trg}}\nabla\phi_{2g}^{n+1}+\frac{1}{3\Sigma^*_{trg}}\nabla\phi_{0g}^{n+1}-\frac{1}{\Sigma^*_{trg}}q_{1g}^{n}\right)+\Sigma^*_{rg}\phi_{0g}^{n+1}=s_{0tg}^{n+1}+q_{0g}^{n}, \quad (4.14a)$$
$$-\frac{3}{5}\nabla\cdot\left(\frac{3}{7\Sigma^*_{tg}}\nabla\phi_{2g}^{n+1}-\frac{1}{\Sigma^*_{tg}}q_{3g}^{n}\right)-\frac{2}{5}\nabla\cdot\left(\frac{2}{3\Sigma^*_{trg}}\nabla\phi_{2g}^{n+1}+\frac{1}{3\Sigma^*_{trg}}\nabla\phi_{0g}^{n+1}-\frac{1}{\Sigma^*_{trg}}q_{1g}^{n}\right)$$
$$+\Sigma^*_{tg}\phi_{0g}^{n+1}=q_{2g}^{n}. \quad (4.14b)$$

The equations above can be expressed in a simple matrix equation form without a group index to compare with the steady-state equation in Eq. (4.8):

$$\begin{bmatrix} -D_1^*\nabla^2+\Sigma_r^* & -2D_1^*\nabla^2 \\ -\frac{2}{5}D_1^*\nabla^2 & -\left(\frac{3}{5}D_3^*+\frac{4}{5}D_1^*\right)\nabla^2+\Sigma_t^* \end{bmatrix}\begin{bmatrix} \phi_0^{n+1} \\ \phi_2^{n+1} \end{bmatrix}=\begin{bmatrix} q_0^n-3D_1^*\nabla\cdot q_1^n+s_{0t}^{n+1} \\ q_2^n-\frac{6}{5}D_1^*\nabla\cdot q_1^n-\frac{7}{5}D_3^*\nabla\cdot q_3^n \end{bmatrix}, \quad (4.15)$$

where $D_1^* \equiv \frac{1}{3\Sigma_{tr}^*}$, $D_3^* \equiv \frac{3}{7\Sigma_t^*}$, $\Sigma_\alpha^* = \Sigma_\alpha + \frac{1}{\upsilon\Delta t}$, $q_i^n = \frac{1}{\upsilon}\frac{\phi_i^n}{\Delta t}$, n = time index.

The terms, $\nabla\cdot q_{ig}^n$ $(i=1,3)$, are additionally considered compared to the time-dependent diffusion equation, which correspond to the terms, $\partial\left(\nabla\cdot\phi_{ig}\right)/\partial t$ $(i=1,3)$, of Eq. (4.12). Since the terms $\nabla\cdot q_{ig}^n$ are the change of leakages with time, their contribution is relatively small compared to the change of the 0th- and 2nd-moments with time.

4.3 Nonlinear Formulation of the SP_3 Equation

While Smith first introduced the idea of nonlinear approach into the steady-state eigenvalue problem, it was Al-Chalabi and Joo that showed the nonlinear method was very efficient for transient fixed source problem, especially when used with the analytic nodal and the nodal expansion methods [Al-Chalabi, 1993], [Joo, 1997]. The conventional expression for the nonlinear CMFD method uses one correction factor as in Eq. (4.1). While $\tilde{D}_g^{i,i+1}$ is simply calculated based on properties of adjacent nodes, $\hat{D}_g^{i,i+1}$ is determined by comparing the CMFD currents with higher-order solution currents. The conventional approach for the nonlinear method is based on the "two-node" problem shown in Fig. 4.1 where the node average fluxes of adjacent nodes serve as boundary conditions.

For practical core problems, "two-node" problems for every surface would be solved to obtain higher-order solution currents. One of the higher-order solvers such as ANM, NEM, AFEN, fine-mesh finite difference method (FMFD), etc., can be used to solve the "two-node" problem and to provide higher-order accurate currents for the given boundary conditions.

For the application of the nonlinear method to the SP_3 equation Moon's approach [Moon, 1999] for the P_1 equation is useful in which he uses two correction factors when applying the nonlinear CMFD method to the AFEN method. In his approach the correction factors are determined by solving a "one-node" problem with a higher-order method. The advantage of this approach is to achieve better computational efficiency compared to the conventional method

which uses one correction factor based on a "two-node" problem because higher-order currents at all surfaces are determined at a time.

There are several variations to formulate the nonlinear "one-node" equation. The first is to define current and surface correction factors for each interface as follows:

$$J_g = -\tilde{D}_{cg}^{i,i+1}(\phi_g^{i+1} - \phi_g^i) - \hat{D}_{cg}^{i,i+1}(\phi_g^{i+1} + \phi_g^i), \tag{4.16a}$$

$$\phi_{sg} = \frac{D_g^{i+1}\phi_g^{i+1} + D_g^i\phi_g^i}{D_g^{i+1} + D_g^i} - \hat{D}_{sg}^{i,i+1}(\phi_g^{i+1} + \phi_g^i), \tag{4.16b}$$

where ϕ_{sg} = surface flux for group g,

$\hat{D}_{cg}$ = current correction factor for group g,

$\hat{D}_{sg}$ = surface correction factor for group g.

The other is to introduce different current correction factors for two sides at each interface:

$$J_{lg}^{i+1}\frac{\Delta}{2} = -D_g^{i+1}(\phi_g^{i+1} - \phi_{gs}) - \hat{D}_g^{i+1}(\phi_g^{i+1} + \phi_{gs}), \tag{4.17a}$$

$$J_{rg}^{i}\frac{\Delta}{2} = -D_g^{i}(\phi_{gs} - \phi_g^i) - \hat{D}_g^{i}(\phi_{gs} + \phi_g^i), \tag{4.17b}$$

where l and r denote left and right surface, respectively. Since $J_{lg}^{i+1} = J_{rg}^{i}$, Eq. (4.17) can be written as:

$$J_g^{i,i+1} = -\tilde{\tilde{D}}_g^{i,i+1}(\phi_g^{i+1} - \phi_g^i) - \hat{\hat{D}}_g^{i,i+1}(\phi_g^{i+1} + \phi_g^i), \tag{4.18a}$$

$$\phi_{sg}^{i,i+1} = \frac{\left(D_g^{i+1} + \hat{D}_g^{i+1}\right)\phi_g^{i+1} + \left(D_g^i - \hat{D}_g^i\right)\phi_g^i}{D_g^{i+1} + D_g^i - \hat{D}_g^{i+1} + \hat{D}_g^i}, \tag{4.18b}$$

where $\tilde{\tilde{D}}_g^{i,i+1} = \dfrac{2(D_g^i D_g^{i+1} + \hat{D}_g^i \hat{D}_g^{i+1})}{\Delta(D_g^{i+1} + D_g^i - \hat{D}_g^{i+1} + \hat{D}_g^i)}$, $\hat{\hat{D}}_g^{i,i+1} = \dfrac{2(D_g^i \hat{D}_g^{i+1} + \hat{D}_g^i D_g^{i+1})}{\Delta(D_g^{i+1} + D_g^i - \hat{D}_g^{i+1} + \hat{D}_g^i)}$.

The two correction factors, $\hat{D}_g^i$ and $\hat{D}_g^{i+1}$, at the same surface are used to calculate currents and surface fluxes which are used to provide partial current boundary conditions for a "one-node" problem.

As shown in Fig. 4.3, partial incoming currents become boundary conditions of a "one-node" problem. The two approaches have the same number of degree of freedom in common, which means that both approaches should basically give the same answers.

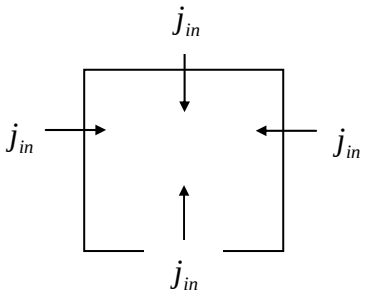

Figure 4.3 One-Node Calculation

Of many higher-order methods, the fine-mesh finite difference method has an advantage of being able to directly use a heterogeneous configuration, which means that there is no need for dehomogenization to obtain fuel pin fluxes and powers. When using the FMFD as a higher-order solver, it is necessary to connect the CMFD solutions to the FMFD quantities. Since the CMFD solutions are node- or surface-average values and the FMFD method requires local information, the boundary conditions of the "one-node" problem can be generated as follows:

$$j_g^{in}(x) = \bar{j}_g^{in}\, f(x), \tag{4.19}$$

where $\bar{j}_g^{in}$ = face-averaged partial incoming current from CMFD,

$j_g^{in}(x)$ = local distribution of partial incoming currents to be used for boundary conditions of FMFD,

$f(x)$ = shape function normalized to the average incoming current.

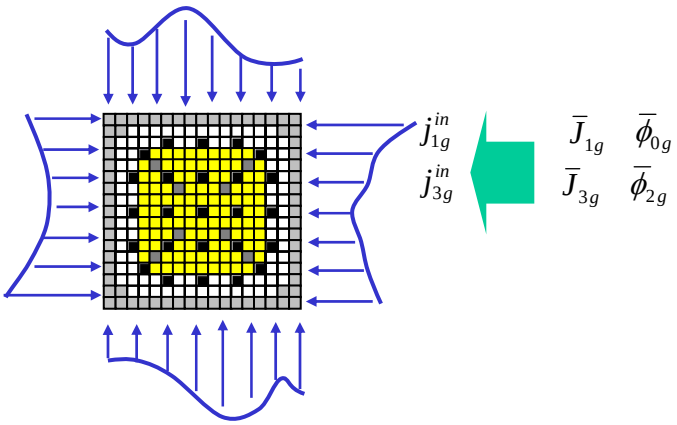

Figure 4.4 Local Boundary Conditions from CMFD Global Values

The procedure for the global/local iteration methods is as follows:

1) Run CMFD (global calculation).
2) Provide the incoming partial currents for every node.
3) Convert average quantities to local ones with the shape function for boundary conditions of "one-node" problems. Then, the local flux shape of the previous iteration can be used for the shape function.
4) Given the incoming partial currents, solve FMFD in each "one-node" problem (local calculation).
5) Sequentially sweep node by node using the outgoing partial currents of a node as the incoming boundary conditions of neighboring nodes.
6) Using the resulting surface currents and fluxes, calculate correction factors and homogenized cross sections.
7) Go back to 1) with updated correction factors and homogenized cross sections.
8) Repeat 2) through 6) until achieving the convergence criterion.

Since the global CMFD calculation is very efficient, the number of the local calculations constitutes the largest fraction of the computational time.

Since the nonlinear formulation has been applied to the P_1 equation, it should be straightforward to extend it to the P_3 equations in multidimensional geometry. However, the question arises about how to treat the higher-moment terms within the framework of the nonlinear formulation. For simplicity, the SP_3 equation shown in Eq. (4.8) is used in two-dimensional x-y geometry with the relationships between the odd and even moments:

$$\phi_{1g} = -\frac{1}{3\Sigma_{trg}}\nabla\Phi_g, \quad \phi_{3g} = -\frac{3}{7\Sigma_{tg}}\nabla\phi_{2g}, \tag{4.20}$$

where $\Phi_g = \phi_{0g} + 2\phi_{2g}$.

Similarly to Eq. (4.18), first and third moments can be written with the definitions of $\hat{\hat{D}}_{1g}^{i,i+1}$ and $\hat{\hat{D}}_{3g}^{i,i+1}$:

$$J_{1g}^{i,i+1} = -\tilde{\tilde{D}}_{1g}^{i,i+1}\left(\Phi_g^{i+1} - \Phi_g^i\right) - \hat{\hat{D}}_{1g}^{i,i+1}\left(\Phi_g^{i+1} + \Phi_g^i\right), \tag{4.21a}$$

$$J_{3g}^{i,i+1} = -\tilde{\tilde{D}}_{3g}^{i,i+1}\left(\phi_{2g}^{i+1} - \phi_{2g}^i\right) - \hat{\hat{D}}_{3g}^{i,i+1}\left(\phi_{2g}^{i+1} + \phi_{2g}^i\right), \tag{4.21b}$$

$$\phi_{0sg}^{i,i+1} = \frac{\left(D_{1g}^{i+1} + \hat{D}_{1g}^{i+1}\right)\phi_{0g}^{i+1} + \left(D_{1g}^{i} - \hat{D}_{1g}^{i}\right)\phi_{0g}^{i}}{D_{1g}^{i+1} + D_{1g}^{i} - \hat{D}_{1g}^{i+1} + \hat{D}_{1g}^{i}}, \tag{4.21c}$$

$$\phi_{2sg}^{i,i+1} = \frac{\left(D_{3g}^{i+1} + \hat{D}_{3g}^{i+1}\right)\phi_{2g}^{i+1} + \left(D_{3g}^{i} - \hat{D}_{3g}^{i}\right)\phi_{2g}^{i}}{D_{3g}^{i+1} + D_{3g}^{i} - \hat{D}_{3g}^{i+1} + \hat{D}_{3g}^{i}}, \tag{4.21d}$$

where $\tilde{\tilde{D}}_{1g}^{i,i+1} = \dfrac{2(D_{1g}^{i} D_{1g}^{i+1} + \hat{D}_{1g}^{i} \hat{D}_{1g}^{i+1})}{\Delta(D_{1g}^{i+1} + D_{1g}^{i} - \hat{D}_{1g}^{i+1} + \hat{D}_{1g}^{i})}$, $\hat{\tilde{D}}_{1g}^{i,i+1} = \dfrac{2(D_{1g}^{i} \hat{D}_{1g}^{i+1} + \hat{D}_{1g}^{i} D_{1g}^{i+1})}{\Delta(D_{1g}^{i+1} + D_{1g}^{i} - \hat{D}_{1g}^{i+1} + \hat{D}_{1g}^{i})}$,

$\tilde{\tilde{D}}_{3g}^{i,i+1} = \dfrac{2(D_{3g}^{i} D_{3g}^{i+1} + \hat{D}_{3g}^{i} \hat{D}_{3g}^{i+1})}{\Delta(D_{3g}^{i+1} + D_{3g}^{i} - \hat{D}_{3g}^{i+1} + \hat{D}_{3g}^{i})}$, $\hat{\tilde{D}}_{3g}^{i,i+1} = \dfrac{2(D_{3g}^{i} \hat{D}_{3g}^{i+1} + \hat{D}_{3g}^{i} D_{3g}^{i+1})}{\Delta(D_{3g}^{i+1} + D_{3g}^{i} - \hat{D}_{3g}^{i+1} + \hat{D}_{3g}^{i})}$,

$D_{1g}^{i} \equiv \dfrac{1}{3\Sigma_{trg}^{i}}$, $D_{3g}^{i} \equiv \dfrac{3}{7\Sigma_{tg}^{i}}$.

In order to determine $\hat{\tilde{D}}_{1g}^{i,i+1}$ and $\hat{\tilde{D}}_{3g}^{i,i+1}$ for the CMFD calculation at all node interfaces, the "one-node" problem can be solved, as shown below in Fig. 4.6, based on Eq. (4.21) with the incoming partial moment boundary conditions.

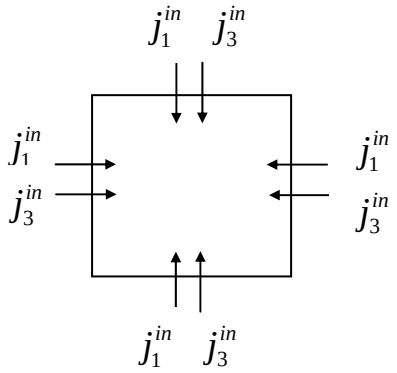

Figure 4.6 One-Node SP_3 Calculation

The incoming partial currents for the second moments can be determined by Eq. (4.10). Note that unlike 0^{th}-moments, 2^{nd}-moments are not always positive.

This nonlinear global/local formulation can also be applied to the S_N method to accelerate convergence since the source iteration of the S_N method has poor convergence when the scattering ratio is close to unity. The nonlinear formulation for the simplified even-parity S_N method ($SEPS_N$) is briefly described in Appendix A. It should be closely investigated in

comparison with some other conventional acceleration methods such as the diffusion synthesis acceleration method (DSA) [Alcouffe, 1977] which works very efficiently for the S_N method. Even though the global/local approach is similar in many respects to conventional acceleration methods, it should be emphasized that there are many attractive features in its application to the transient problem.

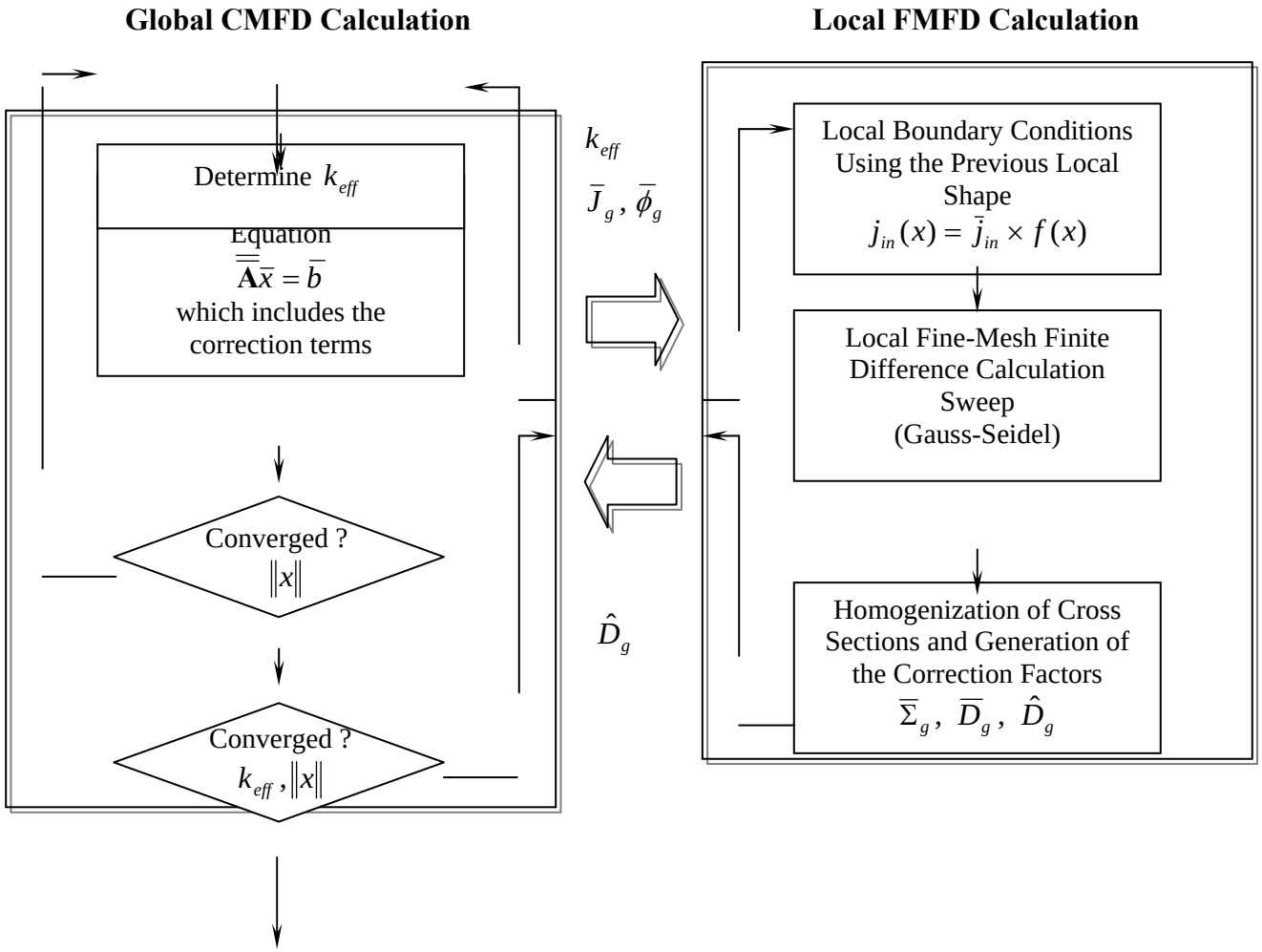

Figure 4.5 Flow for the Global/Local Acceleration

5. MULTIGROUP NODAL EXPANSION METHOD FOR SP_3

In the previous sections, the fine-mesh finite difference (FMFD) method has been discussed to solve the SP_3 equation, which can easily treat heterogeneous geometries within the fuel assembly (FA). However, when the heterogeous effect is not dominant, the FMFD solution can be inefficient in terms of accuracy and time. As in the conventional approach, the spatial homogenization and nodal solution is more favorable in terms of computation time and accuracy. Therefore, the multigroup nodal method for SP_3 is discussed in this section, and its adaptive use depending upon the characteristics of FAs and its surroundings will be discussed later in Section 7.

The nodal method has been widely used and has become the standard for core neutronics calculation since the early 1980s. As noted in the first section, there are several types of nodal methods with different basis functions: nodal expansion method (NEM), analytic nodal method (ANM), analytic function exansion nodal method (AFEN), nodal green function method (NGFM), etc. Among them, the NEM is known to be easy to derive but relatively less accurate than the others under the same number of calculation meshes. In this work, the NEM is utilized for the multigroup SP_3 equation since it is easy to implement for mutigroup applications and simple to apply to more than one moment.

In order to apply the nodal method to the SP_3 equation, Eq. (4.8) is rearranged to:

$$\begin{bmatrix} -D_1\nabla^2+\Sigma_r & -2\Sigma_r \\ -\frac{2}{3}\Sigma_r & -D_3\nabla^2+\Sigma_{rt} \end{bmatrix}\begin{bmatrix} \Phi_0 \\ \phi_2 \end{bmatrix} = S_0\begin{bmatrix} 1 \\ -\frac{2}{3} \end{bmatrix}, \tag{5.1}$$

where $\Phi_0 \equiv \phi_0 + 2\phi_2$, $\Sigma_{rt} \equiv \frac{5}{3}\Sigma_t + \frac{4}{3}\Sigma_r$, $J_1 = -D_1\nabla\Phi_0$, $J_3 = -D_3\nabla\phi_2$.

Eq.(5.1) is more convenient to apply the NEM compared to Eq. (4.8), for reasons that will become apparent later in this section. The Marshak boundary conditions in Eq. (4.10) also change corresponding to the definitions in Eq. (5.1):

$$j_1^{\pm} = \frac{1}{4}\Phi_{0s} \pm \frac{1}{2}J_1 - \frac{3}{16}\phi_{2s}, \quad j_3^{\pm} = \frac{7}{16}\phi_{2s} \pm \frac{1}{2}J_3 - \frac{1}{16}\Phi_{0s}. \tag{5.2}$$

Based on the boundary conditions above and the following relationship between net and partial moments:

$$J_1 = -D_1\nabla\Phi_0 = j_1^+ - j_1^-, \quad J_3 = -D_3\nabla\phi_2 = j_3^+ - j_3^-. \tag{5.3}$$

Eqs. (5.2) and (5.3) require that partial currents and surface fluxes at interfaces satisfy the following relations:

$$\Phi_{0s} = \frac{8}{25}\left[7\left(j_1^+ + j_1^-\right) + 3\left(j_3^+ + j_3^-\right)\right], \quad \phi_{2s} = \frac{8}{25}\left[\left(j_1^+ + j_1^-\right) + 4\left(j_3^+ + j_3^-\right)\right]. \tag{5.4}$$

The one-dimensional equation integrated over transverse directions within a given group can be expressed as:

$$\begin{bmatrix} -D_{1u}\dfrac{d^2}{du^2} + \Sigma_r & -2\Sigma_r \\ -\dfrac{2}{3}\Sigma_r & -D_{3u}\dfrac{d^2}{du^2} + \Sigma_{rt} \end{bmatrix} \begin{bmatrix} \Phi_{0u} \\ \phi_{2u} \end{bmatrix} = S_0 \begin{bmatrix} 1 \\ -\dfrac{2}{3} \end{bmatrix} - \begin{bmatrix} L_{1u} \\ L_{3u} \end{bmatrix}, \ (u = x, y, z), \tag{5.5}$$

where L_{iu} is the transverse leakage to the u-direction in i moment. As in the conventional NEM, the one-dimensional moments can be approximated in 4th-order polynomials:

$$\Phi_{0u}(u) = \sum_{i=0}^{4} a_i h_i(u), \quad \phi_{2u}(u) = \sum_{i=0}^{4} z_i h_i(u), \ \ (u = x, y, z), \tag{5.6}$$

where $h_0(u) = 1,\ h_1(u) = 2u - 1,\ h_2(u) = 6u(1-u) - 1,$

$h_3(u) = 6u(1-u)(2u-1),\ h_3(u) = 6u(1-u)(5u^2 - 5u + 1),\ \ 0 < u < 1.$

Coupling between Eqs. (5.2), (5.3), (5.4) and (5.6) yields the partial moment response equation as follows:

$$J_1^{out} = c_{\overline{\Phi}_0}\overline{\Phi}_0 + c_J J_1^{in} + c_A A + c_{\phi_{2s}}\phi_{2s}, \tag{5.7a}$$

$$J_3^{out} = g_{\overline{\phi}_2}\overline{\phi}_2 + g_J J_3^{in} + g_A A + g_{\Phi_{0s}}\Phi_{0s}, \tag{5.7b}$$

where $j_{1l}^{out} = c_1\overline{\Phi}_0 + c_2 j_{1l}^{in} + c_3 j_{1r}^{in} + c_1 a_4 - c_4 a_3 - c_5\phi_{2l} - c_6\phi_{2r},$

$j_{1r}^{out} = c_1\overline{\Phi}_0 + c_3 j_{1l}^{in} + c_2 j_{1r}^{in} + c_1 a_4 + c_4 a_3 - c_6\phi_{2l} - c_5\phi_{2r},$

$j_{3l}^{out} = g_1\overline{\phi}_2 + g_2 j_{3l}^{in} + g_3 j_{3r}^{in} + g_1 a_4 - g_4 a_3 - g_5\Phi_{0l} - g_6\Phi_{0r},$

$j_{3r}^{out} = g_1\overline{\phi}_2 + g_3 j_{3l}^{in} + g_2 j_{3r}^{in} + g_1 a_4 + g_4 a_3 - g_6\Phi_{0l} - g_5\Phi_{0r},$

$$a_1 = \frac{1}{2}\left(\Phi_{0r} - \Phi_{0l}\right) = j_{1r}^{out} + j_{1r}^{in} - j_{1l}^{out} - j_{1l}^{in} + \frac{3}{8}\left(\phi_{2r} - \phi_{2l}\right),$$

$$a_2 = \overline{\Phi}_0 - \frac{1}{2}\left(\Phi_{0r} + \Phi_{0l}\right) = \overline{\phi} - \left(j_{1r}^{out} + j_{1r}^{in} + j_{1l}^{out} + j_{1l}^{in} + \frac{3}{8}\left(\phi_{2r} + \phi_{2l}\right)\right),$$

$$z_1 = \frac{1}{2}\left(\phi_{2r} - \phi_{2l}\right) = \frac{4}{7}\left(j_{3r}^{out} + j_{3r}^{in} - j_{3l}^{out} - j_{3l}^{in}\right) + \left(\Phi_{0r} - \Phi_{0l}\right),$$

$$z_2 = \bar{\phi}_2 - \frac{1}{2}\left(\phi_{2r} + \phi_{2l}\right) = \bar{\phi}_2 - \left(\frac{4}{7}\left(j_{3r}^{out} + j_{3r}^{in} + j_{3l}^{out} + j_{3l}^{in}\right) + \left(\Phi_{0r} + \Phi_{0l}\right)\right),$$

$$c_1 = \frac{6D_1(1+4D_1)}{1+16D_1+48D_1^2}, \qquad c_2 = \frac{1-48D_1^2}{1+16D_1+48D_1^2}, \qquad c_3 = \frac{-8D_1}{1+16D_1+48D_1^2},$$

$$c_4 = \frac{6D_1(1+12D_1)}{1+16D_1+48D_1^2}, \quad c_5 = \frac{3D_1(1+6D_1)}{1+16D_1+48D_1^2}, \quad c_6 = \frac{3D_1}{2(1+16D_1+48D_1^2)},$$

$$g_1 = \frac{42D_3}{7+48D_3}, \quad g_2 = \frac{49-768D_1^2}{49+448D_1+768D_1^2}, \quad g_3 = \frac{224D_3}{49+448D_1+768D_1^2},$$

$$g_4 = \frac{42D_3}{7+16D_3}, \quad g_5 = \frac{4D_3(7+24D_1)}{49+448D_1+768D_1^2}, \quad g_6 = \frac{14D_3}{49+448D_1+768D_1^2}.$$

Since the surface moments appear on the right hand sides of the partial moment response equations as shown in Eq. (5.7), it is not easy to formulate and solve them. For simplicity, the following relationships are proposed here:

$$\tilde{j}_1^{\pm} = \frac{1}{4}\Phi_{0s} \pm \frac{1}{2}J_1, \quad \tilde{j}_3^{\pm} = \frac{7}{16}\phi_{2s} \pm \frac{1}{2}J_3. \tag{5.8}$$

These are truncated forms for the Marshak boundary conditions shown in Eq. (5.2). Therefore, they are not conventional partial moments but quantities satisfying the following conditions.

$$J_1 = -D_1\nabla\Phi_0 = \tilde{j}_1^{+} - \tilde{j}_1^{-}, \quad J_3 = -D_3\nabla\phi_2 = \tilde{j}_3^{+} - \tilde{j}_3^{-}, \tag{5.9}$$

and

$$\Phi_{0s} = 2\left(\tilde{j}_1^{+} + \tilde{j}_1^{-}\right), \quad \phi_{2s} = \frac{8}{7}\left(\tilde{j}_3^{+} + \tilde{j}_3^{-}\right). \tag{5.10}$$

Eq. (5.9) is the same as Eq. (5.3) and what is more, Eq. (5.10) is simpler than Eq. (5.4). With the variables defined above, reflective boundary conditions and incoming current boundary conditions need to be discussed. Reflective boundary conditions are the same as usual:

$$\tilde{j}_1^{+} = \tilde{j}_1^{-}, \quad \tilde{j}_3^{+} = \tilde{j}_3^{-}. \tag{5.11}$$

However, incoming current boundary conditions become different compared to the original ones since $\tilde{j}_1^{\pm}$ and $\tilde{j}_3^{\pm}$ are not real partial moments. Inserting Eqs. (5.9) and (5.10), using Eqs. (5.2) and (5.8) and $j_1^{in} = j_3^{in} = 0$ yields:

$$\tilde{j}_1^{+} = \frac{3}{109}\left(\tilde{j}_1^{-} + 8\tilde{j}_3^{-}\right), \quad \tilde{j}_3^{+} = \frac{3}{109}\left(14\tilde{j}_1^{-} + 3\tilde{j}_3^{-}\right). \tag{5.12}$$

Finally, the relations between artificial partial currents, net currents, and surface fluxes have the same form as in the NEM formulation of the diffusion equation with some additional consideration for the incoming boundary conditions as shown in Eq. (5.12). The final form of the partial moment response equation using $\tilde{j}^{\pm}$ then becomes the same as the conventional NEM formulation:

$$\tilde{J}_1^{out} = c_{\bar{\Phi}_0}\bar{\Phi}_0 + c_J\tilde{J}_1^{in} + c_A A, \tag{5.13a}$$

$$\tilde{J}_3^{out} = g_{\bar{\phi}_2}\bar{\phi}_2 + g_J\tilde{J}_3^{in} + g_A A, \tag{5.13b}$$

where
$$\tilde{j}_{1l}^{out} = c_1\bar{\Phi}_0 + c_2\tilde{j}_{1l}^{in} + c_3\tilde{j}_{1r}^{in} + c_1a_4 - c_4a_3,$$
$$\tilde{j}_{1r}^{out} = c_1\bar{\Phi}_0 + c_3\tilde{j}_{1l}^{in} + c_2\tilde{j}_{1r}^{in} + c_1a_4 + c_4a_3,$$
$$\tilde{j}_{3l}^{out} = g_1\bar{\phi}_2 + g_2\tilde{j}_{3l}^{in} + g_3\tilde{j}_{3r}^{in} + g_1a_4 - g_4a_3,$$
$$\tilde{j}_{3r}^{out} = g_1\bar{\phi}_2 + g_3\tilde{j}_{3l}^{in} + g_2\tilde{j}_{3r}^{in} + g_1a_4 + g_4a_3,$$
$$a_1 = \frac{1}{2}\left(\Phi_{0r} - \Phi_{0l}\right) = \tilde{j}_{1r}^{out} + \tilde{j}_{1r}^{in} - \tilde{j}_{1l}^{out} - \tilde{j}_{1l}^{in},$$
$$a_2 = \bar{\Phi}_0 - \frac{1}{2}\left(\Phi_{0r} + \Phi_{0l}\right) = \bar{\Phi}_0 - \left(\tilde{j}_{1r}^{out} + \tilde{j}_{1r}^{in} + \tilde{j}_{1l}^{out} + \tilde{j}_{1l}^{in}\right),$$
$$z_1 = \frac{1}{2}\left(\phi_{2r} - \phi_{2l}\right) = \frac{4}{7}\left(\tilde{j}_{3r}^{out} + \tilde{j}_{3r}^{in} - \tilde{j}_{3l}^{out} - \tilde{j}_{3l}^{in}\right),$$
$$z_2 = \bar{\phi}_2 - \frac{1}{2}\left(\phi_{2r} + \phi_{2l}\right) = \bar{\phi}_2 - \left(\frac{4}{7}\left(\tilde{j}_{3r}^{out} + \tilde{j}_{3r}^{in} + \tilde{j}_{3l}^{out} + \tilde{j}_{3l}^{in}\right)\right).$$

The definitions of the coefficients c_i and g_i are the same as in Eq. (5.7). However, the definitions of the low-order coefficients, a_1 and a_2, changed as seen in Eq. (5.13), which do not include surface moments on the right hand side.

One of the most important considerations in the transverse averaged one-dimensional approach is the approximation of the transverse leakage shapes. In this work here, the transverse leakage shape is approximated in a second-order polynomial for both 0th and 2nd moments as:

$$L_{0u}(u)=\sum_{i=0}^{2} b_i h_i(u), \quad L_{2u}(u)=\sum_{i=0}^{2} p_i h_i(u), \tag{5.14}$$

where $b_0=\bar{L}_{0u}$, $b_1=\frac{1}{2}\left(L_{0r}-L_{0l}\right)$, $b_2=\bar{L}_{0u}-\frac{1}{2}\left(L_{0ur}+L_{0ul}\right)$,

$p_0=\bar{L}_{2u}$, $p_1=\frac{1}{2}\left(L_{2r}-L_{2l}\right)$, $p_2=\bar{L}_{2u}-\frac{1}{2}\left(L_{2ur}+L_{2ul}\right)$.

The second-order polynomial approximation for the transverse leakage of the 0th moment has been well established for applying the NEM to the diffusion equation. However, a quadratic approximation is not adequate for the 2nd moment since the 2nd moment shape is dramatically changing near interfaces of very different materials. In the work here, a parabolic approximation, which is a rough approximation for the 2nd moment, will be used since the effect of the 2nd moments is relatively small in magnitude compared to the 0th moments and refining more meshes relieves dramatic change of the 2nd moment. If greater accuracy is desired in the future, better approximations for the transverse leakage of 2nd moments will be necessary.

The higher-order coefficients, a_3 and a_4, are determined by solving two more moment equations with the weighted residual method for Eq. (5.5) using $h_1(u)$ and $h_2(u)$, which are shown in Eq. (5.6), as weighting functions. The resulting equations then become:

$$(60\frac{D_u}{\Delta_u}+\Sigma_r)a_3=-\frac{5}{3}\Sigma_r a_1+S_{03}-\frac{5}{3}b_1+2\Sigma_r\left(\frac{5}{3}z_1+z_3\right), \tag{5.15a}$$

$$(140\frac{D_u}{\Delta_u}+\Sigma_r)a_4=\frac{7}{3}\Sigma_r a_2+S_{04}+\frac{7}{3}b_2+2\Sigma_r\left(-\frac{7}{3}z_2+z_4\right), \tag{5.15b}$$

$$(60\frac{D_u}{\Delta_u}+\Sigma_{rt})z_3=-\frac{5}{3}\Sigma_{rt}z_1+S_{23}-\frac{5}{3}p_1+2\Sigma_r\left(\frac{5}{3}a_1+a_3\right), \tag{5.15c}$$

$$(140\frac{D_u}{\Delta_u}+\Sigma_{rt})z_4=\frac{7}{3}\Sigma_{rt}z_3+S_{24}+\frac{7}{3}p_2+2\Sigma_r\left(-\frac{7}{3}a_2+a_4\right), \tag{5.15d}$$

where $S_{03}=\sum_{g'}\left(\frac{5}{3}a_1+a_3-2\left(\frac{5}{3}z_1+z_3\right)\right)\Sigma_{sg'g}+\frac{\chi_g}{k_{eff}}\sum_{g'}\left(\frac{5}{3}a_1+a_3-2\left(\frac{5}{3}z_1+z_3\right)\right)\nu\Sigma_{fg'}$,

$$S_{04} = \sum_{g'} \left(-\frac{7}{3} a_2 + a_4 + 2\left(\frac{7}{3} z_2 - z_4 \right) \right) \Sigma_{sg'g} + \frac{\chi_g}{k_{eff}} \sum_{g'} \left(-\frac{7}{3} a_2 + a_4 + 2\left(\frac{7}{3} z_2 - z_4 \right) \right) \nu\Sigma_{fg'},$$

$$S_{23} = -\frac{2}{3} S_{03}, \quad S_{24} = -\frac{2}{3} S_{04}.$$

By defining new variables, $\tilde{j}_1^{\pm}$ and $\tilde{j}_3^{\pm}$ in Eq. (5.8), all equations became simple and very similar to the conventional NEM equations for the diffusion equation. This means that the existing routines can be utilized for solving the multigroup SP_3 NEM with only minor modifications.

The transverse averaged one-dimensional equations, Eq. (5.5), are normally solved one direction at a time. However, when it is solved using the global/local acceleration method based upon the "one-node" approach for the multigroup solution, convergence problems are sometimes encountered. When the one-dimensional equation is solved for one direction, the leakages to the transverse directions should be approximated. Since the neutron balance of a node is not being satisfied in a multi-dimensional sense, convergence becomes difficult, particularly in multigroup problems. Therefore, a method was developed to solve multi-dimensional equations simultaneously such that the resulting solutions satisfy the nodal neutron balance.

Eq. (5.16) shows moment matrix equations in which 2-D or 3-D one-dimensional equations are solved at the same time, satisfying the nodal neutron balance in a node. As will be explained in the next sections, 0^{th} and 2^{nd} moments are not solved simultaneously, but determined sequentially for computational efficiency. In other words, a moment is used as a source of the other moment determined in the previous iteration step. As seen in Eq. (5.16), there are in fact 13 unknowns for a three-dimensional problem, which include currents and higher coefficients of the nodal expansion polynomials of each direction and node-average moments. The elements of the matrix of the left hand side of the equation are only property dependent, but those of the right hand side are composed of the fission source, partial moments which are boundary conditions, low-order coefficients of the nodal expansion polynomials of the other moments and transverse leakage coefficients.

Even though the performance of the multigroup SP_3 NEM at transient is interesting in terms of stability and accuracy, the transient formulation remains as future work.

$$\begin{bmatrix} 1 & 0 & c_4 & -c_1 & -c_1 \\ 0 & 1 & -c_4 & -c_1 & -c_1 \\ -\frac{5}{3}\Sigma_r & \frac{5}{3}\Sigma_r & \left(60\frac{D_{1u}}{\Delta_u}+\Sigma_r\right) & 0 & 0 \\ \frac{7}{3}\Sigma_r & \frac{7}{3}\Sigma_r & 0 & \left(140\frac{D_{1u}}{\Delta_u}+\Sigma_r\right) & -\frac{7}{3}\Sigma_r \\ \frac{1}{\Delta_u} & \frac{1}{\Delta_u} & 0 & 0 & \Sigma_r \end{bmatrix} \begin{bmatrix} \tilde{j}_{1l}^{out} \\ \tilde{j}_{1r}^{out} \\ a_3 \\ a_4 \\ \overline{\Phi}_0 \end{bmatrix} =$$

$$\begin{bmatrix} c_2\tilde{j}_{1l}^{in}+c_3\tilde{j}_{1r}^{in} \\ c_3\tilde{j}_{1l}^{in}+c_2\tilde{j}_{1r}^{in} \\ -\frac{5}{3}\Sigma_r\left(\tilde{j}_{1r}^{in}-\tilde{j}_{1l}^{in}\right)+S_{03}-\frac{5}{3}D_1b_1+2\Sigma_r\left(\frac{5}{3}z_1+z_3\right) \\ -\frac{7}{3}\Sigma_r\left(\tilde{j}_{1r}^{in}+\tilde{j}_{1l}^{in}\right)+S_{04}+\frac{7}{3}D_1b_2+2\Sigma_r\left(-\frac{7}{3}z_2+z_4\right) \\ \left(\tilde{j}_{1l}^{in}+\tilde{j}_{1r}^{in}\right)/\Delta_u+S_0+2\Sigma_r\overline{\phi}_2 \end{bmatrix}, \quad (5.16a)$$

$$\begin{bmatrix} 1 & 0 & z_4 & -z_1 & -z_1 \\ 0 & 1 & -z_4 & -z_1 & -z_1 \\ -\frac{5}{3}\Sigma_{rt} & \frac{5}{3}\Sigma_{rt} & \left(60\frac{D_{3u}}{\Delta_u}+\Sigma_{rt}\right) & 0 & 0 \\ \frac{7}{3}\Sigma_{rt} & \frac{7}{3}\Sigma_{rt} & 0 & \left(140\frac{D_{3u}}{\Delta_u}+\Sigma_{rt}\right) & -\frac{7}{3}\Sigma_{rt} \\ \frac{1}{\Delta_u} & \frac{1}{\Delta_u} & 0 & 0 & \Sigma_{rt} \end{bmatrix} \begin{bmatrix} \tilde{j}_{3l}^{out} \\ \tilde{j}_{3r}^{out} \\ z_3 \\ z_4 \\ \overline{\phi}_2 \end{bmatrix} =$$

$$\begin{bmatrix} z_2\tilde{j}_{3l}^{in}+z_3\tilde{j}_{3r}^{in} \\ z_3\tilde{j}_{3l}^{in}+z_2\tilde{j}_{3r}^{in} \\ -\frac{20}{21}\Sigma_{rt}\left(\tilde{j}_{3r}^{in}-\tilde{j}_{3l}^{in}\right)+S_{23}-\frac{5}{3}D_3p_1+\frac{2}{3}\Sigma_r\left(\frac{5}{3}a_1+a_3\right) \\ -\frac{4}{3}\Sigma_{rt}\left(\tilde{j}_{3r}^{in}+\tilde{j}_{3l}^{in}\right)+S_{24}+\frac{7}{3}D_3p_2+\frac{2}{3}\Sigma_r\left(-\frac{7}{3}a_2+a_4\right) \\ \left(\tilde{j}_{3l}^{in}+\tilde{j}_{3r}^{in}\right)/\Delta_u+\frac{2}{3}\left(\Sigma_r\overline{\Phi}_0-S_0\right) \end{bmatrix}. \quad (5.16b)$$

Note that these equations should consist of 13×13 matrices and 13×1 vectors for the 3-D problem by repeating components corresponding to $\left(\tilde{j}_{1l}^{out}, \tilde{j}_{1r}^{out}, a_3, a_4\right)$ and $\left(\tilde{j}_{3l}^{out}, \tilde{j}_{3r}^{out}, z_3, z_4\right)$ for the other directions, respectively.

6. NUMERICAL CONVERGENCE OF THE SP_3 EQUATION

6.1 Stability in the SP_3 equation

Before addressing the stability characteristics of the SP_3 equations, it is worthwhile to discuss a lower bound for the stable convergence in the P_1 formulation. For the "two-factor one-node" approach disscussed in Section 4, the CMFD formulation in Eq. (4.18a) is rewritten as:

$$J_{i,i+1}^{g} = -(\tilde{\tilde{D}}_{i,i+1}^{g} + \hat{\tilde{D}}_{i,i+1}^{g})(\phi_{i+1}^{g} - \alpha_{i,i+1}^{g}\phi_{i}^{g}), \tag{6.1}$$

where $\tilde{\tilde{D}}_{i,i+1}^{g} = \dfrac{2(D_i^g D_{i+1}^g + \hat{D}_i^g \hat{D}_{i+1}^g)}{(D_i^g + D_{i+1}^g - \hat{D}_i^g + \hat{D}_{i+1}^g)\Delta}$, $\hat{\tilde{D}}_{i,i+1}^{g} = \dfrac{2(D_i^g \hat{D}_{i+1}^g + \hat{D}_i^g D_{i+1}^g)}{(D_i^g + D_{i+1}^g - \hat{D}_i^g + \hat{D}_{i+1}^g)\Delta}$,

$\alpha_{i,i+1}^{g} = \dfrac{\tilde{\tilde{D}}_{i,i+1}^{g} - \hat{\tilde{D}}_{i,i+1}^{g}}{\tilde{\tilde{D}}_{i,i+1}^{g} + \hat{\tilde{D}}_{i,i+1}^{g}}$.

The fast convergence and stability of the iterative solution of the linear equation are assured as long as the diagonal dominance is maintained as discussed in Eq. (4.5). This yields the following conditions:

$$\tilde{\tilde{D}}_{i,i+1}^{g} + \hat{\tilde{D}}_{i,i+1}^{g} > 0, \tag{6.2a}$$

$$\tilde{\tilde{D}}_{i,i+1}^{g} - \hat{\tilde{D}}_{i,i+1}^{g} > 0, \tag{6.2b}$$

which, since $\tilde{\tilde{D}}_{i,i+1}^{g}$ is always positive, implies the following:

$$\tilde{\tilde{D}}_{i,i+1}^{g} > \left|\hat{\tilde{D}}_{i,i+1}^{g}\right|. \tag{6.3}$$

This prescribes a lower bound for the stable convergence of the P_1 nonlinear formulation. If this condition is met with sufficient margin, then convergence can be achieved. The adequacy of the margin is related to the diagonal dominance affecting the convergence efficiency.

The same analysis as performed for the P_1 formulation above can be applied for the nonlinear SP_3 formulation. Rearranging Eqs. (4.21a) and (4.21b) yields:

$$J_{1g}^{i,i+1} = -\left(\tilde{\tilde{D}}_{1g}^{i,i+1} + \hat{\hat{D}}_{1g}^{i,i+1}\right)\left(\Phi_g^{i+1} - \alpha_{i,i+1}^g \Phi_g^i\right), \tag{6.4a}$$

$$J_{3g}^{i,i+1} = -\left(\tilde{\tilde{D}}_{3g}^{i,i+1} + \hat{\hat{D}}_{3g}^{i,i+1}\right)\left(\phi_{2g}^{i+1} - \beta_{i,i+1}^g \phi_{2g}^i\right), \tag{6.4b}$$

where $\Phi_g^i = \phi_{0g}^i + 2\phi_{2g}^i$, $\alpha_{i,i+1}^g = \dfrac{\tilde{\tilde{D}}_{1g}^{i,i+1} - \hat{\hat{D}}_{1g}^{i,i+1}}{\tilde{\tilde{D}}_{1g}^{i,i+1} + \hat{\hat{D}}_{1g}^{i,i+1}}$, $\beta_{i,i+1}^g = \dfrac{\tilde{\tilde{D}}_{3g}^{i,i+1} - \hat{\hat{D}}_{3g}^{i,i+1}}{\tilde{\tilde{D}}_{3g}^{i,i+1} + \hat{\hat{D}}_{3g}^{i,i+1}}$.

Since Eq. (6.4) is the same as Eq. (6.1), the same idea can be applied to it. However, as far as Eq. (6.4) is concerned, no bound exists because the second moment does not always have the same sign. In addition, the correction factors for second moments, $\hat{\hat{D}}_{3g}^{i,i+1}$, are sometimes very large since the second moment is very small at a node center and dramatically changes at node interfaces. Even though the overall convergence behavior of the SP_3 equation is driven by the zeroth moment, the characteristics of second moment correction factors may disturb convergence when the zeroth and second moments are similar in magnitude.

From Eq. (4.8), the second-moment equation can be written:

$$-\left(\frac{3}{5}D_{3g} + \frac{4}{5}D_{1g}\right)\nabla^2\phi_{2g}(x) + \Sigma_{tg}\phi_{2g}(x) = -L_{0g}(x), \tag{6.5}$$

where $L_{0g}(x) = -\dfrac{2}{5}D_g\nabla^2\phi_{0g}(x)$.

The right hand side of Eq. (6.5) is considered as a source which represents a “in-leakage” of zeroth-moments. This means that when there is a positive “in-leakage”, the sources in the second moment equation are positive and otherwise they are negative. For example, when UOX and MOX fuel assemblies are adjacent as in Figs. 6.1, 6.2, and 6.3, the fast flux is relatively high in a MOX fuel assembly and low in a UOX fuel assembly. The situation is opposite for the thermal flux. Therefore, the thermal second moment is normally positive in a MOX region and negative in a UOX region. Figs. 6.1 through 6.3 show the zeroth and second moment distributions for several combinations of fuel assembly types. Note that especially at the interface where the gradient of current is large, there appear large peaks in the second moments, but they quickly show asymptotic behavior in the middle of assemblies.

One of the characteristics of the multi-level formulation for the "one-node" approach in the local calculation is to use the incoming partial currents as boundary conditions for a local problem. In contrast, the "two-node" approach uses node average fluxes of the two neighboring nodes as boundary conditions. It is interesting to compare the boundary conditions used in the "one-node" and "two-node" approaches on the convergence rate. Since node average fluxes are not changing dramatically in the course of convergence, the boundary conditions of the "two-node" approach are also not changing much, which improves convergence. However, since partial incoming currents generally converge more slowly than node average fluxes, the convergence of the "one-node" approach can be somewhat worse than the "two-node" approach. Therefore, a multiple (typically double) sweeping technique is used to obtain more rigorous partial current boundary conditions for "one-node" problems. Overall, the "one-node" approach is comparable or superior to the "two-node" one in terms of computation time because currents on all sides are determined simultaneously in the "one-node" approach. Furthermore, the "one-node" approach has additional favorable features which will be discussed in the following section.

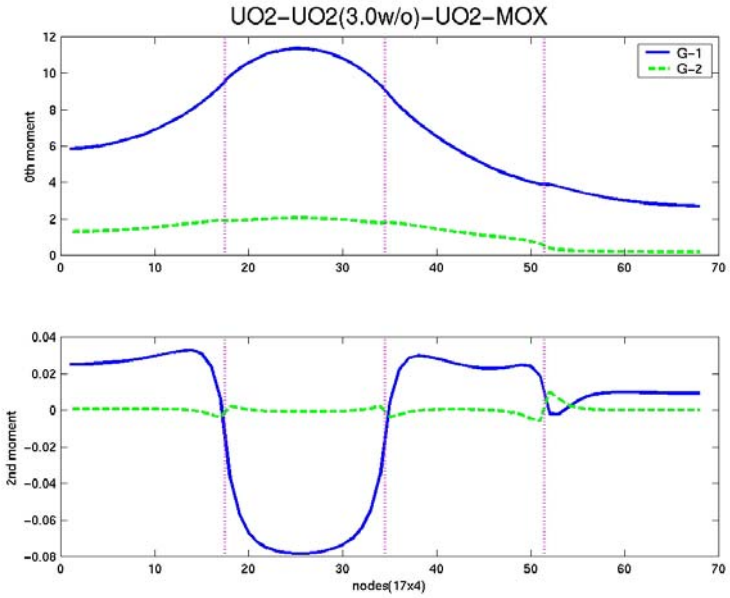

Figure 6.1 Zeroth- and Second-Moment Distributions for UOX(2w/o)-UOX(3w/o)-UOX(3w/o)-MOX(7w/o)

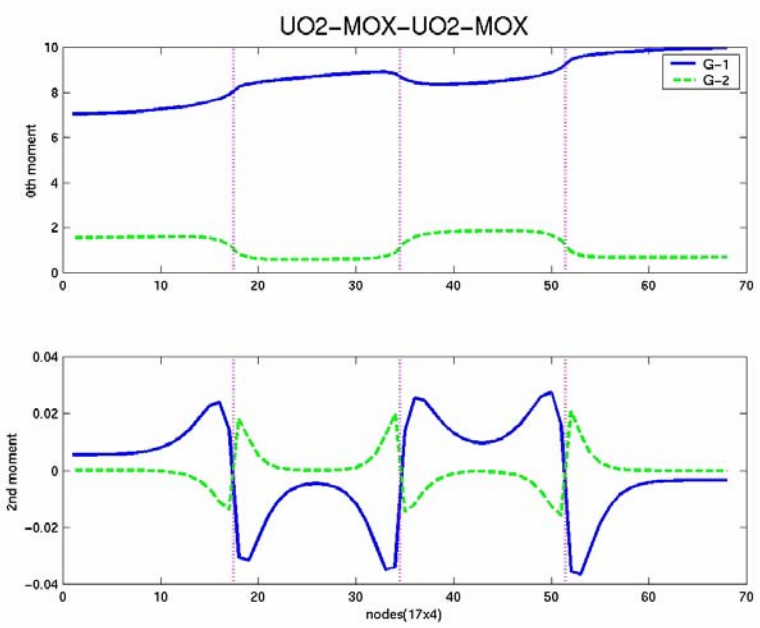

Figure 6.2 Zeroth- and Second-Moment Distributions for UOX(2w/o)-MOX(7w/o)-UOX(2w/o)-MOX(12w/o)

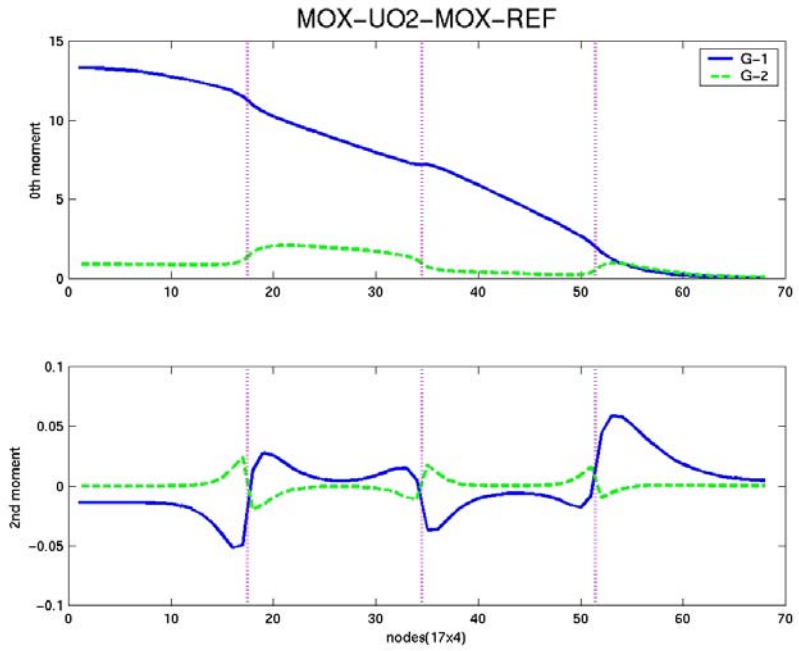

Figure 6.3 Zeroth- and Second-Moment Distributions for MOX(7w/o)-UOX(2w/o)-MOX(7w/o)-REF

6.2 Numerical Optimization

6.2.1 Ordering Analysis in the SP_3 calculation

There are several possible orderings of the SP_3 matrix. The ordering of the variables such as angle, group, and space does not change the numerical properties of the matrix, but it can have an influence on the state of convergence. The most typical ordering is to arrange the variables in (angle, space, group) order as depicted in Fig. 6.4: the angle is placed innermost and the group outermost in a vector. This forms 2×2 block matrices consisting of flux moments in the diagonal elements. Therefore, angle and space are normally solved at the same time in the inner iteration, and group is solved in a Gauss-Seidel manner in an outer loop. An alternative ordering is to have the (space, group, angle) ordering with angle outmost as shown in Fig. 6.5. In this case, the 0^{th}-moments are first determined, which are used as sources when solving the 2^{nd}-moment equation. Eq. (4.8) is thus rearranged as:

$$\begin{bmatrix} -D_1\nabla^2+\Sigma_r & 0 \\ 0 & -\left(\frac{3}{5}D_3+\frac{4}{5}D_1\right)\nabla^2+\Sigma_t \end{bmatrix}\begin{bmatrix}\phi_0\\ \phi_2\end{bmatrix} = D_1\nabla^2\begin{bmatrix}2\phi_2\\ \frac{2}{5}\phi_0\end{bmatrix}+S_0\begin{bmatrix}1\\0\end{bmatrix}, \qquad (6.6)$$

where $D_1 \equiv \frac{1}{3\Sigma_{tr}}$, $D_3 \equiv \frac{3}{7\Sigma_t}$.

Each method provides a different structure of A-matrices in the $Ax=b$ problem. For the purpose of illustration, the structures of the matrices are shown for one energy group as shown in Figs. 6.6 and 6.7. In the case of Fig. 6.6, the matrix is 2×2-block symmetric in which the zeroth- and second-moments are coupled. Alternately, the A-matrix in Fig. 6.7 is not symmetric, but it can be solved angle by angle in a Gauss-Seidel iteration. Table 6.1 shows the performance associated with ordering in terms of CPU time. While the original ordering, (angle, space, group), is about 7 times slower, compared to the P_1 solution, the second ordering, (space, group, angle), is only about two times slower.

Table 6.1 Comparison with Change of Ordering for SP_3

3x3 FAs,		SP_3

17x17 pins, 3x3/pin		Order-1	**Order-2**
K-eff	1.000868	1.001725	
CPU	1	6.8	1.5
Iteration	26	29	31

* order-1: (angle, space, group)
* order-2: (space, group, angle)

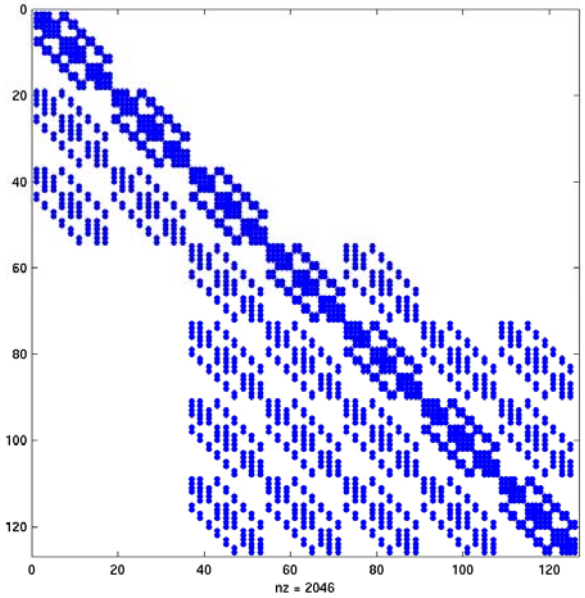

(2 angular moments, 5x5 nodes, 7 groups)
Figure 6.4 A-matrix with the (Angle, Space, Group) Ordering

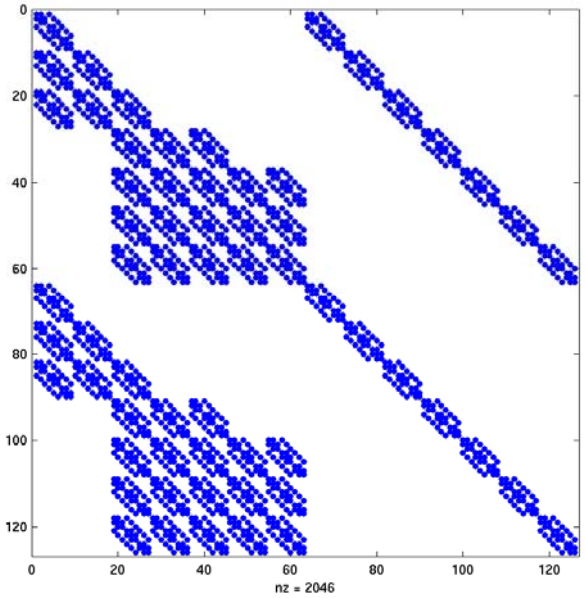

(5x5 nodes, 7 groups, 2 angular moments)

Figure 6.5 A-matrix with the (Space, Group, Angle) Ordering

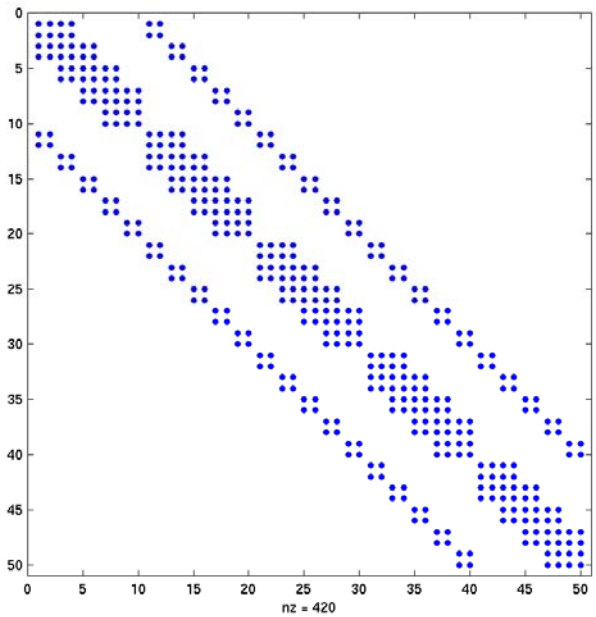

(2 angular moments, 5x5 nodes)

Figure 6.6 A-matrix with the (Angle, Space) Ordering for a Group

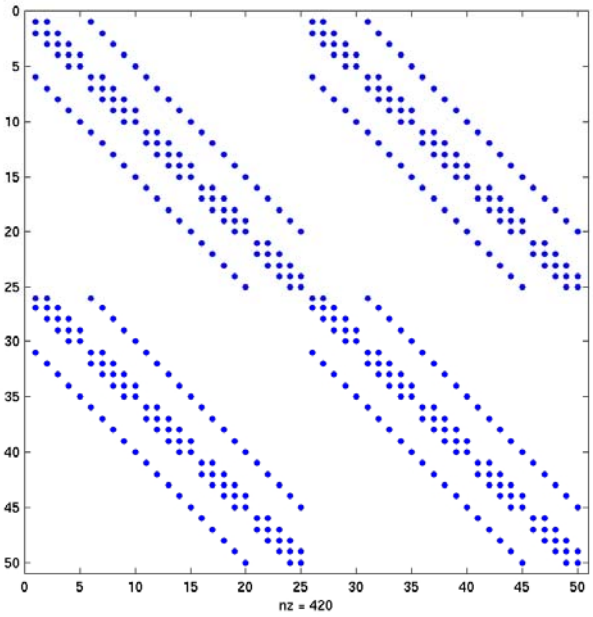

(5x5 nodes, 2 angular moments)
Figure 6.7 A-matrix with the (Space, Angle) Ordering for a Group

6.2.2 Group Collapse in the Global/Local Acceleration

Normally in a multigroup problem, the same number of energy groups is treated in the global and local calculations. For example, if seven groups are treated in the local one-node calculation, seven groups of corrective terms would be generated at every node interface and then used in the global calculation. However, it is possible to reduce the number of groups in the global calculation so that the existing two-group structure of the global routines of the code can be used as it is and the computation time for CMFD may be reduced. The idea is somewhat similar to that used in the popular coarse group rebalancing method (CGR).

In the CGR method, for example, the multigroup equation is reduced to the few-group equations by conserving all the reaction rates and leakage:

$$\nabla \cdot J_g + \Sigma_{rg}\phi = \sum_{g' \neq g} \Sigma_{sg'g}\phi_{g'} + \lambda \sum_{g'} \Sigma_{fg'}\phi_{g'} \quad \text{(g=1,…..,G).} \qquad (6.7)$$

The rebalancing equation is constructed in the following manner with so-called driving factors, d_g:

$$A\left(j_G^{out} d_G - \sum_n j_{nG}^{out} d_{nG} \right) + R_{rG} d_G = \sum_{G' \neq G} R_{sG'G} d_G + \lambda \sum_{G'} R_{fG'} d_{G'}, \qquad (6.8)$$

where $R_{kG} = \sum_{g' \in G} \Sigma_{kg'} \phi_{g'} V$, $j_G^{out} = \sum_{g' \in G} j_{g'}^{out}$,

d_G = driving factor, A = area, n = neighboring nodes.

Unlike the CGR method, in the method proposed here cross sections are condensed to two groups and correction factors are generated for only two groups, which is used in the global two-group diffusion calculation.

$$\nabla \cdot \bar{J}_G + \bar{\Sigma}_{rG} \bar{\phi}_G = \sum_{G' \neq G} \bar{\Sigma}_{sG'G} \bar{\phi}_{G'} + \lambda \sum_{G'} \bar{\Sigma}_{fG'} \bar{\phi}_{G'}, \quad (G = 1,2) \qquad (6.9)$$

where $\bar{\phi}_G = \sum_{g' \in G} \phi_{g'} V$, $\bar{\Sigma}_{kG} = \sum_{g' \in G} \Sigma_{kg'} \phi_{g'} V / \bar{\phi}_G$, $\bar{J}_G = \sum_{g' \in G} J_{g'} A$.

The CMFD current for coarse group G is defined in the same way as in Eq. (4.3) with the fixed number of groups:

$$\bar{J}_G^{i,i+1} = -\tilde{\tilde{D}}_G^{i,i+1} (\bar{\phi}_G^{i+1} - \bar{\phi}_G^{i}) - \hat{\hat{D}}_G^{i,i+1} (\bar{\phi}_G^{i+1} + \bar{\phi}_G^{i}), \ (G = 1,2) \qquad (6.10)$$

where $\tilde{\tilde{D}}_G^{i,i+1} = \dfrac{2(D_G^i D_G^{i+1} + \hat{D}_G^i \hat{D}_G^{i+1})}{\Delta(D_G^{i+1} + D_G^i - \hat{D}_G^{i+1} + \hat{D}_G^i)}$, $\hat{\hat{D}}_G^{i,i+1} = \dfrac{2(D_G^i \hat{D}_G^{i+1} + \hat{D}_G^i D_G^{i+1})}{\Delta(D_G^{i+1} + D_G^i - \hat{D}_G^{i+1} + \hat{D}_G^i)}$.

When prolongating the few-group values the shape functions which are used in restricting the fine-group values can be used in the following manner:

$$\bar{J}_g = \bar{J}_G \times f(g), \quad \bar{\phi}_g = \bar{\phi}_G \times h(g), \quad \bar{\phi}_{sg} = \bar{\phi}_{sG} \times w(g), \qquad (6.11)$$

where $f(g)$, $h(g)$, and $w(g)$ are the normalized fine-group shape functions for current, average flux, and surface flux, respectively.

A preliminary test of this idea with the global/local acceleration technique was successful. The global CMFD routine does not need to be changed even when increasing the

number of energy groups at the local level. It also provides improved computational efficiency since the two-group CMFD scheme with the ILU preconditioned BiCGSTAB method can always be used for multigroup problems. The detailed implementation and performance of this method will be discussed in the section 8.

7. MULTI-LEVEL ACCELERATION AND ADAPTIVE METHODS

7.1 Multi-Level Method

The heterogeneous FA configuration with pin-by-pin meshes obviates the use of the nodal approach which has only a few calculation meshes per FA. Even though the nonlinear formulation of the pin-by-pin multigroup SP_3 calculation relieves the computation burden for steady-state and transient calculations, it still requires a considerable amount of computing time, particularly, for three-dimensional whole core transient simulations. When comparing computation times between the conventional two-group nodal diffusion method and the heterogeneous multigroup SP_3 method, it can be noted that the computational time is significantly increased. The fine-mesh versus nodal increases by more than 100 times: the multigroup (n) versus two-group by a factor of more than $n/2$, and SP_3 versus diffusion by a factor of about 2 ~ 3.

As discussed in the previous sections, the global/local (two-level) acceleration method is useful for the CMFD diffusion calculation with FA-homogenized cross sections at the global level and the FMFD pin-by-pin SP_3 calculation at the local level. The global quantities such as eigenvalue and FA-averaged two-group fluxes are quickly converged in the global level, while the local quantities such as pin-by-pin multigroup moments within an assembly are relatively slowly converged in the local calculation. Because most of the computation time is determined by the local calculations, it is important to perform the minimum number of the local calculations and to have the local fission sources converged as fast as possible in order to reduce the computation time and achieve the better convergence.

One way to improve performance in terms of the computation time is to insert more levels between the global and local levels as in the conventional multi-level or multi-grid methods. In the report, the three-level method is proposed as shown in Figs. 7.1 and 7.2 in which an intermediate level with the two-group pin-by-pin (1 node/pin) diffusion calculation can be added. At the first step, the local level gives two-group pin-by-pin correction factors and cross sections for the intermediate level, and then the intermediate-level calculation is performed to provide coarse-mesh (e.g. 1 node/FA) correction factors and cross sections. The iteration between intermediate and global levels is performed until reaching a certain tolerance. In this iteration, there is no group and angle condensation, but only spatial homogenization. The solution algorithm then returns to the local level by prolongation with respect to group and space, and updates the distribution of fission sources and incoming currents at boundaries of local

problems. This process, local/intermediate and intermediate/global iterations, is repeated until eigenvalue and pin-by-pin fluxes are converged within given convergence criteria.

The following equations are solved at each level, which should be equivalent in terms of reaction rates and leakage:

$$\nabla \cdot J_g^{het}(r) + \Sigma_{tg}^{het}(r)\phi_g^{het}(r) = \sum_{g'=1}^{MG} \Sigma_{sg'g}^{het}(r)\phi_{g'}^{het}(r) + \frac{\chi_g^{het}}{k} \sum_{g'=1}^{MG} \nu\Sigma_{fg'}^{het}(r)\phi_{g'}^{het}(r), \quad (g = 1,...,MG), \tag{7.1a}$$

$$\nabla \cdot \bar{J}_g^{het}(r) + \bar{\Sigma}_{tg}^{het}(r)\bar{\phi}_g^{het}(r) = \sum_{g'=1}^{2} \bar{\Sigma}_{sg'g}^{het}(r)\bar{\phi}_{g'}^{het}(r) + \frac{1}{k} \sum_{g'=1}^{2} \overline{\nu\Sigma}_{fg'}^{het}(r)\bar{\phi}_{g'}^{het}(r), \quad (g = 1, 2), \tag{7.1b}$$

$$\nabla \cdot \bar{J}_g^{\mathrm{hom}}(r) + \bar{\Sigma}_{tg}^{\mathrm{hom}}(r)\bar{\phi}_g^{\mathrm{hom}}(r) = \sum_{g'=1}^{2} \bar{\Sigma}_{sg'g}^{\mathrm{hom}}(r)\bar{\phi}_{g'}^{\mathrm{hom}}(r) + \frac{1}{k} \sum_{g'=1}^{2} \overline{\nu\Sigma}_{fg'}^{\mathrm{hom}}(r)\bar{\phi}_{g'}^{\mathrm{hom}}(r), \quad (g = 1, 2), \tag{7.1c}$$

where $J_g^{het}(r), \phi_g^{het}(r)$: fine-mesh pin-by-pin multigroup SP_3 solutions,

$\bar{J}_g^{het}(r)$, $\bar{\phi}_g^{het}(r)$: pin-by-pin (1 node/pin) 2-group diffusion solutions,

$\bar{J}_g^{\mathrm{hom}}(r)$, $\bar{\phi}_g^{\mathrm{hom}}(r)$: coarse-mesh (e.g. 1 node/FA) 2-group diffusion solutions.

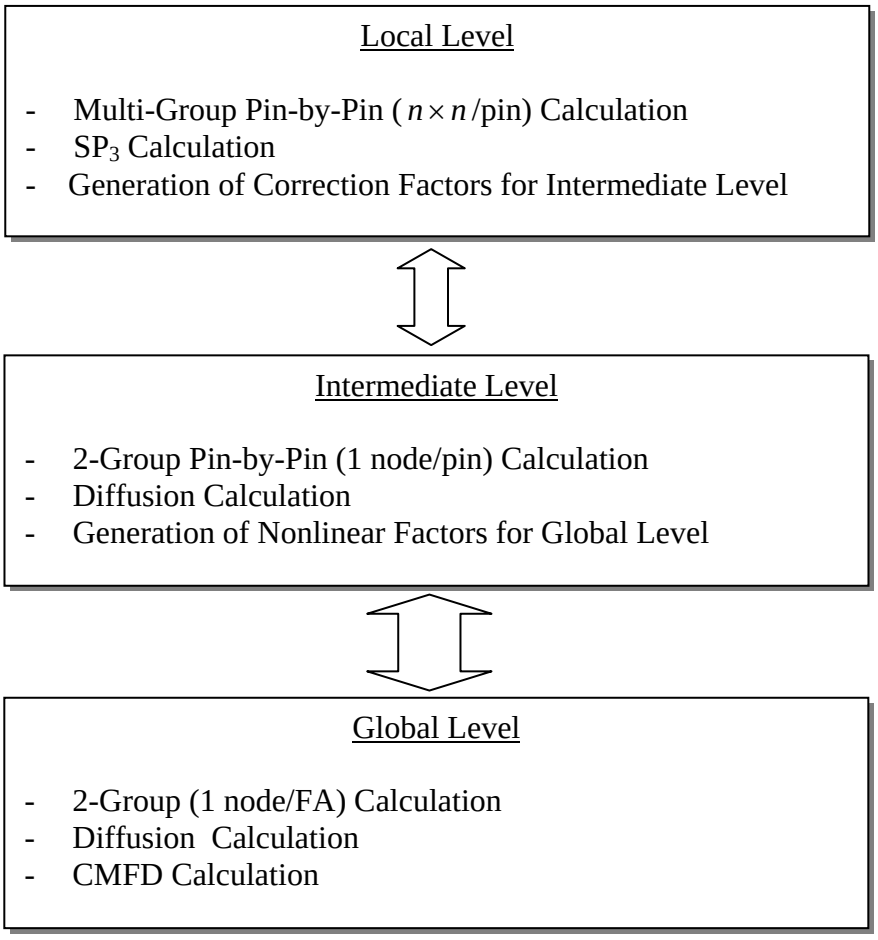

Figure 7.1 A Flow of Multi-Level Calculation

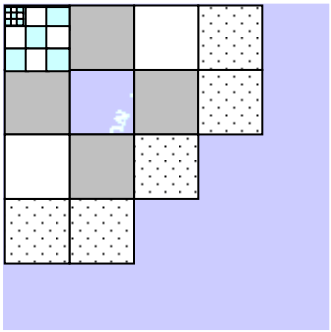

Multi-group
Fine-mesh
Pin-by-pin geometry
SP_3

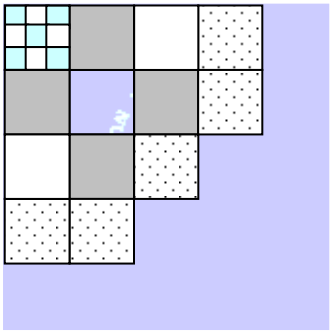

2-group
1 node/pin
Pin-by-pin geometry
Diffusion
Pinwise $\hat{\hat{D}}_{sg}$ (g=1,2)

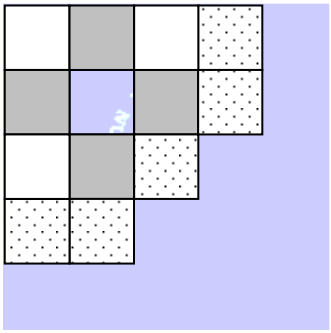

2-group
1 node/FA (e.g.)
Coarse-node homogeneous geometry
Diffusion
Coarse-nodewise $\hat{\hat{D}}_{sg}$

Figure 7.2 A Graphical View of Multi-Level Calculation

Eqs. (7.1a), (7.1b), and (7.1c) correspond to local, intermediate, and global levels, respectively. Once converged, all of them should have the same eigenvalues, reaction rates, and leakages in each group. In order to force the three equations above to have the same reaction rates and currents, the following relations are satisfied:

$$\overline{\Sigma}_{\alpha G}^{het} = \frac{\sum_{i\in P}\sum_{g'\in G}\Sigma_{\alpha g',i}\phi_{g',i}V_i}{\sum_{i\in P}\sum_{g'\in G}\phi_{g',i}V_i}, \quad \hat{D}_G^{het} = \frac{\overline{D}_G^{het}(\overline{\phi}_G - \overline{\phi}_{sG}) - \overline{J}_{sG}^{het}\Delta/2}{\overline{\phi}_G + \overline{\phi}_{sG}} \tag{7.2a}$$

$$\overline{\Sigma}_{\alpha G}^{\hom} = \frac{\sum_{j\in FA}\overline{\Sigma}_{\alpha g',j}^{het}\overline{\phi}_{g',j}^{het}V_j}{\sum_{j\in FA}\overline{\phi}_{g',j}^{het}V_j}, \quad \hat{D}_G^{\hom} = \frac{\overline{D}_G^{\hom}(\overline{\phi}_G^{\hom} - \overline{\phi}_{sG}^{\hom}) - \overline{J}_{sG}^{\hom}\Delta/2}{\overline{\phi}_G^{\hom} + \overline{\phi}_{sG}^{\hom}} \tag{7.2b}$$

where α = cross section type, P = pin, FA = fuel assembly.

Essentially, convergence can be further improved by using intermediate levels, depending upon the characteristics of problems. However, since the optimization of intermediate levels can be another substantial issue as in the conventional multi-level method, it is not further addressed in this report. The performance of only the three-level acceleration method will be discussed in section 8.

7.2 Adaptive Methods

For the heterogeneous configuration (pin-by-pin), the fine-mesh finite difference method is preferable to nodal methods. With the homogeneous configurations (FA-homogenized cross sections), however, it is obviously efficient to use the nodal method for the spatial discretization. As far as the number of energy group is concerned, the multigroup calculation is very effective when the actual spectrum is very different from the lattice spectrum used off-line for group collapsing. As discussed in Section 2, for example, the spectrum of the MOX/UOX combination is very different from the asymptotic spectrum which either of them has in a single fuel assembly calculation performed with the lattice code. However, the UOX/UOX combination, which has typically mild spectral transitions, may not need to be analyzed with multigroup or heterogeneous SP_3. For angle, an increasing order of angular approximation can basically be effective in places where the diffusion approximation fails, but it needs to be considered in association with the equivalence homogenization theory when homogenization is involved [Koebke, 1980] [Smith, 1986]. Therefore, it may not be necessary to apply the heterogeneous multigroup SP_3 approximation to all the nodes in the core. It would be more efficient to selectively apply the detailed approximation to the nodes as required, which is a primary motivation of an adaptive method.

The essential idea of an adaptive method is to use a suitable combination of different methods with respect to group, space and angle in one calculation: multigroup and 2-group, diffusion and SP_3, fine-mesh finite difference and nodal methods. Since there is no reference calculation, an appropriate approximation should be involved when expanding smaller information to larger information on space, energy, and angle: for example, between coarse-mesh and fine-mesh, 2-group and multi-group, and diffusion (one moment) and SP_3 (two moments).

In the "one-node" problem explained in section 4, incoming partial currents used as boundary conditions are the only information exchanged between nodes. Between coarse-mesh and fine-mesh nodes, the coarse outgoing partial currents of the coarse-mesh node need to be expanded to the fine incoming partial current of fine-mesh node, shown in Fig. 7.3.

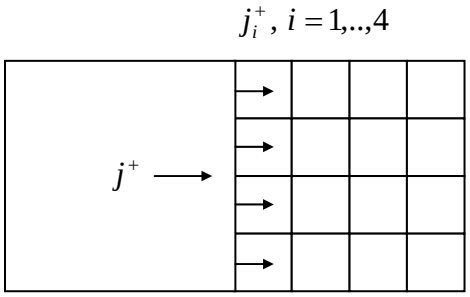

Figure 7.3 Partial Current Interaction at the Interface between Coarse-mesh and Fine-mesh Nodes

The incoming partial current can be approximated by a quadratic polynomial with known average, top, and bottom partial currents.

$$j^+(x) = \bar{j}^+ + a_1\xi_1(x) + a_2\xi_2(x), \quad (7.3)$$

where $\xi_1(x) = 2x-1,\ \xi_2(x) = 6x(1-x)-1,\ a_1 = \frac{1}{2}\left(j_T^+ - j_B^+\right),\ a_2 = \bar{j}^+ - \frac{1}{2}\left(j_T^+ + j_B^+\right),$

j_T^+ = partial current at top corner, j_B^+ = partial current at bottom corner.

The incoming partial current of the fine-mesh side is expressed as:

$$\begin{aligned} j_i^+ &= \int_{r_1}^{r_2} j^+(x)dx \\ &= j_B^+(r_2-r_1) + (3\bar{j}^+ - 2j_B^+ - j_T^+)(r_2^{\,2} - r_1^{\,2}) - (2\bar{j}^+ - j_B^+ - j_T^+)(r_2^{\,3} - r_1^{\,3}), \end{aligned} \quad (7.4)$$

where $r_i \in [0, 1]$.

The opposite direction, from fine-mesh to coarse mesh, is much simpler by using:

$$j^- = \frac{1}{\Delta} \sum_i j_i^- , \qquad (7.5)$$

where Δ = node size.

For angle, it is necessary to estimate higher-order current moments as boundary conditions. This is somewhat complicated since higher-order current moments are much more dramatically changing compared to the conventional current defined in the diffusion theory. The simple approach is to approximate all the incoming higher-order current moments by zero. If this assumption is applied to the nodes sufficiently far from the node of interest, it will not introduce any serious error. However, if the assumption is made at boundaries of the node of interest, it will cause some errors. It remains to be investigated how much error is introduced by this approximation.

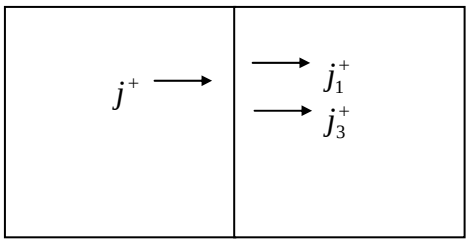

Figure 7.4 Partial Current Interaction at the Interface between diffusion and SP_3 Nodes

For energy group, few group information (two-group) needs to be expanded to multi-group without any reference fine-group structure. The fine-group structure of the incoming partial current is assumed to be the same as that of the outgoing partial current. As a first step, the fine-group structure is assumed to be flat or based on precalculated shapes, and then from the following steps, it is extended from the fine-group structure of the outgoing partial current.

$$j_g^+(r) = j_G^+ \times f_g(r), \quad g \in G, \qquad (7.6)$$

where $f_g(r)$ is a normalized distribution of $j_g^+(r)$.

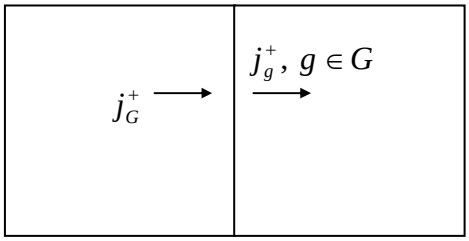

Figure 7.5 Partial Current Interaction at the Interface between Coarse and Fine Groups

Upon convergence, both the outgoing and incoming partial current would have the same fine-group structure.

Different order of approximations in terms of space, angular moment, and energy group can be mixed in the same core calculation with the projections of coarse-mesh to fine-mesh, first-order current moment to higher current moments, and two-group to multi-group. In the local calculation level, adaptive methods can be used to save computing time while maintaining similar accuracy to when more complicated local calculations were performed. Fig. 7.6 shows an example of combining different methods in a core calculation. Note that an additional advantage of this configuration is that no serious effort is necessary to construct the reflector cross sections since the reflector is explicitly modeled. The performance of this method will be discussed in more detail in Section 8.

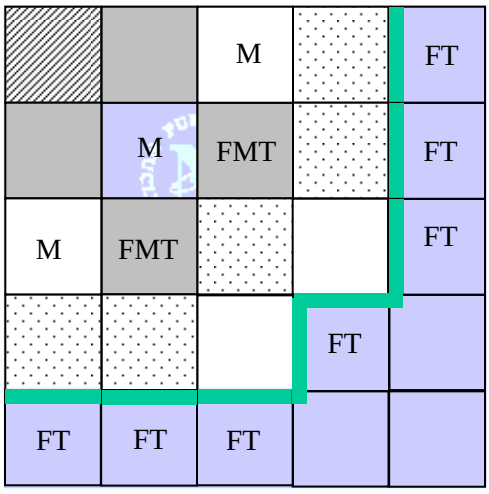

(F: Fine-mesh, M: Multi-group, T: Transport (SP_3), Others: 2-G, nodal, diffusion)
Figure 7.6 Adaptive Choice of Methods in a Core Calculation

8. VERIFICATION

8.1 Implementation

All the methods discussed here have been implemented in PARCS which already has the global/local iteration solver with the two-group diffusion method and higher-order spatial methods such as NEM and ANM for steady-state and transient conditions [Joo, 1998]. Since the new methods are based on a two-group diffusion acceleration at the global level, the existing global routine can be used with minor modifications. Fig. 8.1 depicts on how the newly implemented routines work in PARCS. The multigroup pin-by-pin FMFD, FA-homogeneous NEM, and the adaptive method are simply selected with input options.

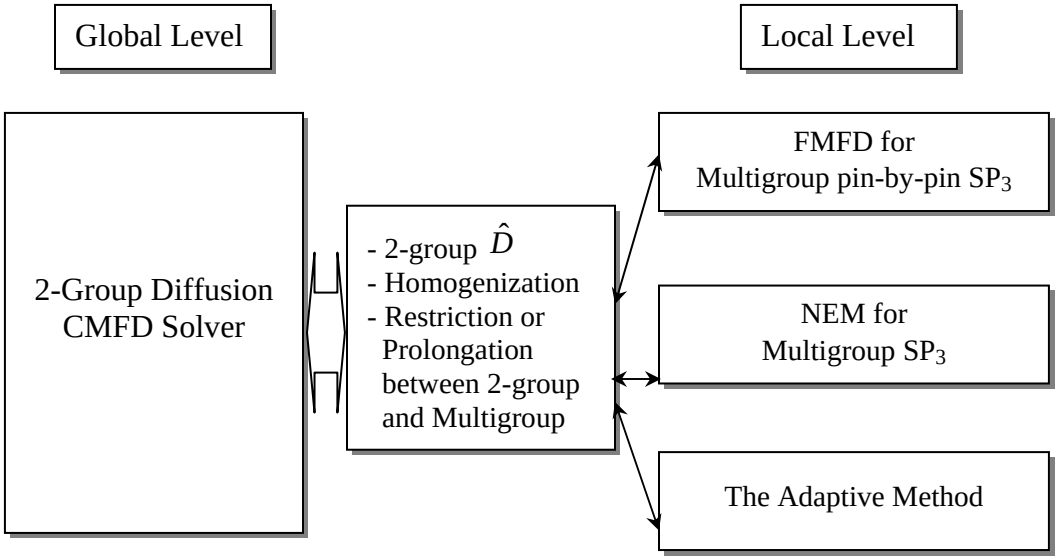

Figure 8.1 Diagram on the Methods Implemented into PARCS

In the global calculation, the BiCG stabilized (BiCGSTAB) algorithm with the blockwise incomplete LU (BILU) already implemented in PARCS is used for the CMFD calculation. In addition, the eigenvalue calculation is accelerated with the Wielandt shift method. In the local calculation when using fine-mesh FDM, the ILU-preconditioned CG method is used. The red-black Gauss-Seidel method is also employed for sweeping one-nodes.

8.2 Benchmark Problems

Two MOX benchmark problems are used to verify the methods proposed here: the OECD L336-C5 [Sartori, 1991] and the KAIST benchmark problems [Cho, 2000]. Even though the original L336-C5 problem has 2-group cross sections for homogeneous and heterogeneous

FA configurations, the cross sections of the KAIST benchmark problem are employed with the same L336-C5 core configuration in order to examine homogenization and transport effects in a multigroup structure. The KAIST benchmark problem has a larger-sized core with MOX, UOX, control rods, and burnable absorbers, and therefore more closely resembles a practical PWR model. The TWODANT code, a Los Alamos S_N code [Alcouffe, 1995], is used to first obtain the reference solutions and then to calculate homogenized cross sections. The details of each benchmark problem will be discussed in the following sections.

8.2.1 OECD L336-C5 Benchmark Problem

This benchmark problem has 2x2 fuel assemblies with UOX and MOX which are surrounded by water reflectors as shown in Fig. 8.2. Since the size of the core is small, the leakage of neutrons is very large. Therefore, there are large flux gradients at both the core boundary and at UOX/MOX interfaces. Two-group assembly or pin cross sections were originally provided for this problem. In the two-group calculation, however, the transport and homogenization effects will be small since the changes in the intermediate energy group range are smeared. Therefore, 7-group pin cross sections (see Table 8.1) and heterogeneous FA configurations (see Fig. 8.3) are used from the KAIST benchmark problem in order to create a more realistic problem and to examine all the effects discussed in Section 2.

When condensing 7-group cross sections to a few groups in order to investigate the group homogenization effect, the manner of generating few-group diffusion coefficients or transport-corrected cross sections is important since results can be very different depending upon the group condensation method. For the diffusion equation, the usual direct weighting of the multigroup diffusion coefficients is used, which preserves the fundamental-mode leakage:

$$\Sigma_{\alpha,I,G} = \frac{1}{V_I \, \phi_{I,G}} \sum_{i \in I} V_i \sum_{g \in G} \Sigma_{\alpha,i,g} \phi_{i,g} \, , \; D_{I,G} = \frac{1}{V_I \, \phi_{I,G}} \sum_{i \in I} V_i \sum_{g \in G} D_{i,g} \phi_{i,g} \, , \qquad (8.1)$$

where i, g = fine node and group indices, I, G = coarse node and group indices,
α = cross section type.

In the work here, the energy cutoffs shown in Table 8.1 are used for 2 groups and 4 groups. The higher order of S_N method in TWODANT is used to obtain the reference solution as well as FA-homogenized cross sections for each assembly. The preliminary calculations listed in Table 8.2 show a comparison of eigenvalues between the S_{16} method with pin-homogenized cross sections and different orders of methods with FA-homogenized cross sections, which gives a rough idea of group and space homogenization effects. The assembly discontinuity factors (ADFs) are also used in the calculations with FA-homogenized cross sections. It is noted in

Table 8.2 that the trend of differences between 2-group and 7-group calculations and between diffusion and SP_3 calculations is not predictable because of cancellation effects between the errors. However, the results shown in Table 8.2 at least imply that the substantial discrepancy in eigenvalue can be caused from group and spatial homogenization.

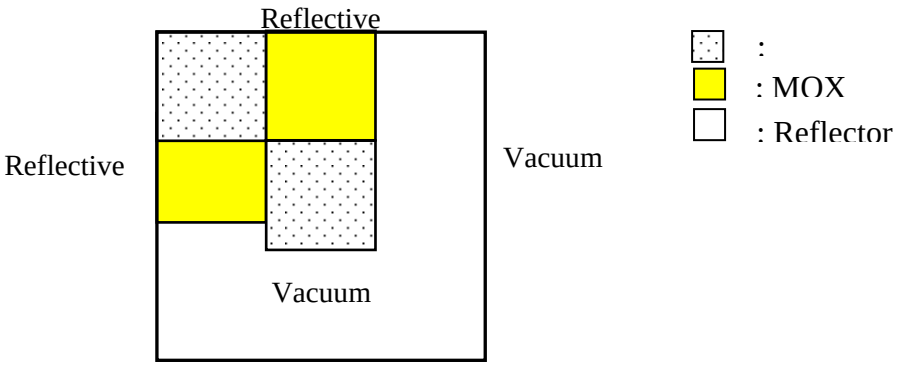

Figure 8.2 Geometry of the OECD L336 C-5 Benchmark Problem

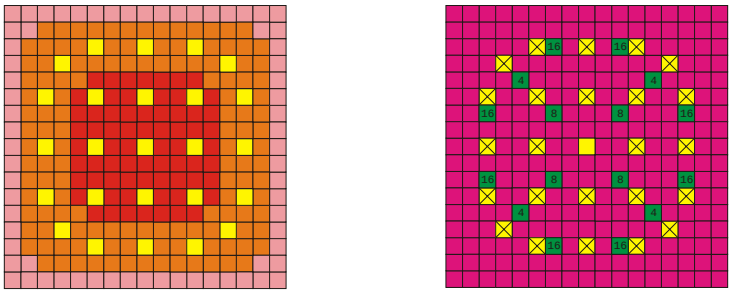

MOX FA UO_2

MOX (boundary: 4.3w/o, middle: 7.0 w/o, center: 8.7 w/o)
UOX (3.3 w/o)

Figure 8.3 Heterogeneous Configurations of MOX and UOX Fuel Assemblies

Table 8.1 Energy Cutoffs for 2 Groups and 7 Groups

7-Group	4-Group	2-Group	Cutoff Energy
1	1	1	~ 1.353 MeV
2	2		1.353 ~ 9.119 KeV
3			9.119 ~ 3.928 eV
4	3		3.928 ~ 0.625 eV
5	4	2	0..625 ~ 0.146 eV
6			0.146 ~ 0.057 eV
7			0.057 eV ~

Table 8.2 Comparison of Eigenvalues in the L336-C5 Benchmark Problem

FA	Method	Group	k-effective	Δ k-eff (pcm)
HET	S_{16}	7	0.95919	0
HOM	Diffusion	2	0.96019	99
		7	0.95710	-209
	SP_3	2	0.96210	291
		7	0.96039	119

8.2.2 KAIST Benchmark Problem

This benchmark problem is composed of various fuel types including MOX, in which 7-group cell-homogeneous and cell-heterogeneous cross sections are provided. Figs. 8.3 and 8.4 show the assembly and core geometries of the KAIST benchmark problem, respectively. Tables 8.1, 8.3 and 8.4 show energy cutoffs and specifications of the problem. The 7-group cell heterogeneous cross sections were first generated by condensing the HELIOS [Villarino, 1992] results with 34 groups. From these cell heterogeneous cross sections, the 7-group cell homogeneous cross sections were generated by the CRX code [Cho, 1996] which is based on the method of characteristics (MOC). Cell homogeneous cross sections are then given by each pin type. Instead of total cross sections and P_1 scattering cross sections, transport-corrected cross sections are given by the following definition:

$$\Sigma_{tr,g'\leftarrow g} = \Sigma_{0,g'\leftarrow g} - \delta_{g'g}\Sigma_{1g}, \tag{8.2}$$

where $\Sigma_{1g} = \sum_{g'=1}^{G} \Sigma_{1,g'\leftarrow g}$.

KAIST performed several types of calculations to examine errors in various modelling approximations [Cho, 2000]. First, CRX was run with pin-heterogeneous configurations (e.g. fuel, clad, gap, moderator, etc.), and these results were considered as a reference. The pin-homogeneous cross sections were then used for CRX and TWODANT. In short, the whole-core heterogeneous calculation was performed with CRX whose results were compared with TWODANT results in which S_8 was used with 2x2 meshes per pin. Furthermore, the heterogeneous calculation was also compared with 2-group AFEN [Noh, 1993] solutions which used the conventional procedure. They concluded that there were significant errors in the conventional procedure using the nodal method with 2-group cross sections generated in single fuel assembly calculations with reflective boundary conditions.

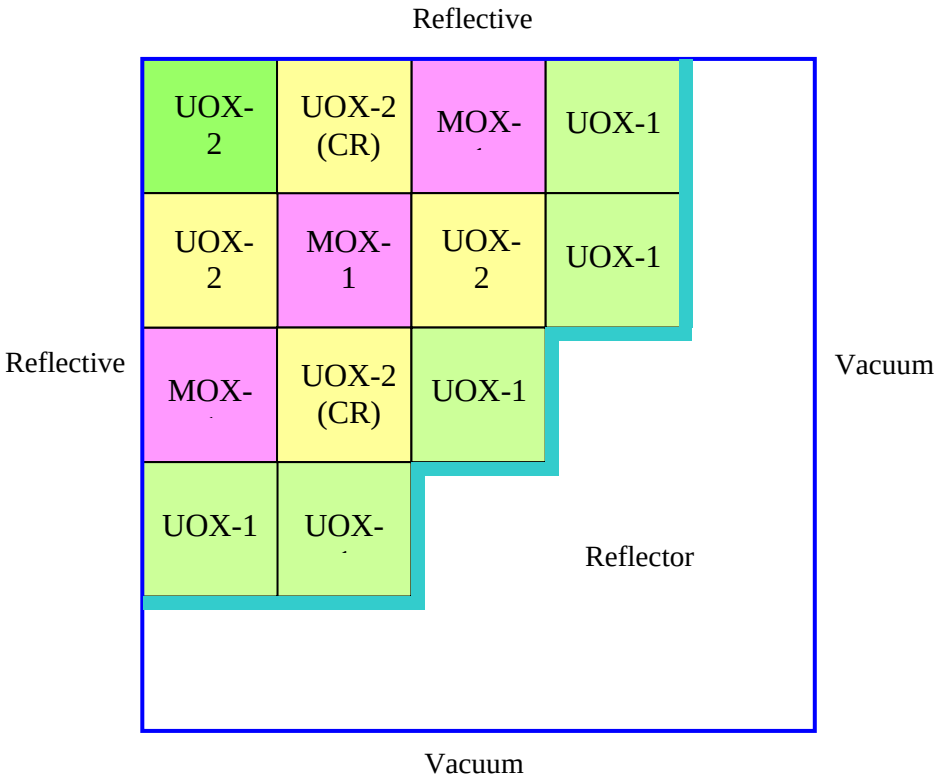

Figure 8.4 Configuration of the KAIST Benchmark Problem

In the work here, TWODANT was also used to solve the KAIST Benchmark problem. Several calculations were performed to examine the effect of the number of groups, order of angles and heterogeneity. Since a transport code similar to CRX was not available, the TWODANT solution was considered as the reference in the analysis here. FA-homogenized cross sections are generated with a single FA calculation and zero-current boundary condition. The two-group reflector cross sections were provided with the two-node (fuel assembly and reflector) calculation.

Table 8.5 summarizes comparison of eigenvalues between the S_{16} method with pin-homogenized cross sections and different orders of methods with FA-homogenized cross sections in the same way as performed for the L336-C5 benchmark problem. As observed in the

previous benchmark problem, the magnitude of differences between 2-group and 7-group calculations and between diffusion and SP_3 calculations changes unexpectedly. The same reason as in the L336-C5 results can be hold. As mentioned in the previous section, the results in Table 8.5 at least indicates that homogenization and transport consideration can cause substantial errors in eigenvalue.

Fig. 8.5 shows the pin power distribution of the KAIST MOX benchmark problem, which has large variations in pin powers due to MOX fuel loading. Figs. 8.6 through 8.8 show 1^{st}-, 4^{th}-, and 7^{th}-group flux distributions in which dramatic variations of fluxes can be observed at interfaces between MOX and UOX in the lowest group.

The original KAIST MOX benchmark problem was modified so that it becomes more simple and appropriate to analyze in this work. First, the baffle is removed from the core, and the core, which is composed of UOX FAs only, is constructed for the purpose of comparison with the MOX core in characteristics. All multigroup cross sections including partial cross sections and transient parameters are generated from HELIOS again since partial cross sections and transient parameters, which are very necessary for transient calculations, are not provided from the original KAIST benchmark problem. Figs. 8.9 and 8.10 show the modified MOX and UOX benchmark cores. It will be interesting to compare the magnitude of eigenvalue errors at stead-state conditions and to compare the transient behaviors between the two types of cores.

Table 8.3 Assembly Specification of the KAIST Benchmark

Lattice	17x17
Assembly Pitch	21.42 cm
GT / IT	24 / 1

Table 8.4 Fuel Types Loaded in the KAIST Benchmark

Fuel Assembly	Content	k-inf
UOX-1	2.0 w/o UO_2	1.10040

UOX-2 (BA_{16})	3.3 w/o UO_2, 16 BAs (GD + 0.711 w/o)	1.03171
UOX-2 (CR)	3.3 w/o UO_2, 24 Control Rods	0.80074
MOX-1	8.7 w/o (inner), 7.0 w/o(middle), 4.3 w/o (outer) Pu	1.16957
MOX-1 (BA_8)	8.7 w/o (inner), 7.0 w/o(middle), 4.3 w/o (outer) Pu, 8 BAs (GD + 0.711 w/o)	1.12814

Table 8.5 Comparison of Eigenvalues in the KAIST Benchmark Problem

FA	Method	Group	k-effective	Δ k-eff (pcm)
HET	S_{16}	7	0.95521	0
HOM	Diffusion	2	0.95799	278
		7	0.95379	-142
	SP_3	2	0.95909	388
		7	0.95567	46

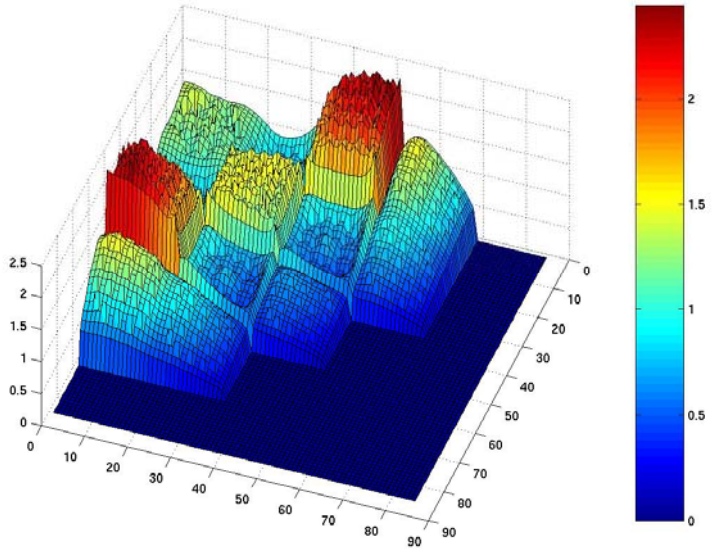

Figure 8.5 Pin Power Distribution of KAIST Benchmark Problem from TWODANT (S_8, 3x3 meshes/pin)

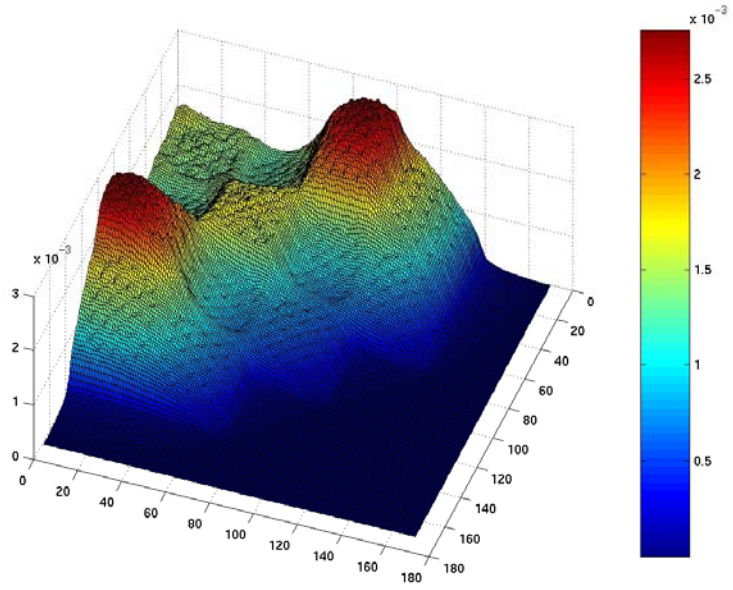

Figure 8.6 1st Group Flux Distribution of the KAIST Core

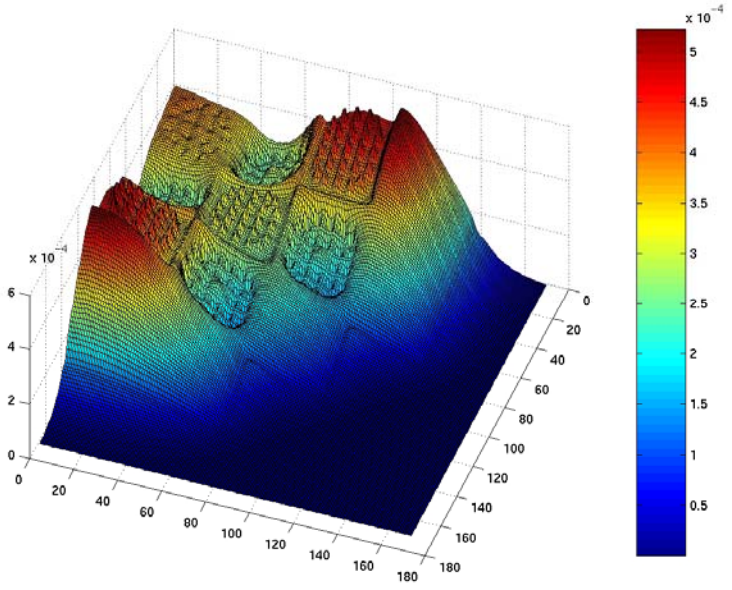

Figure 8.7 4th Group Flux Distribution of the KAIST Core

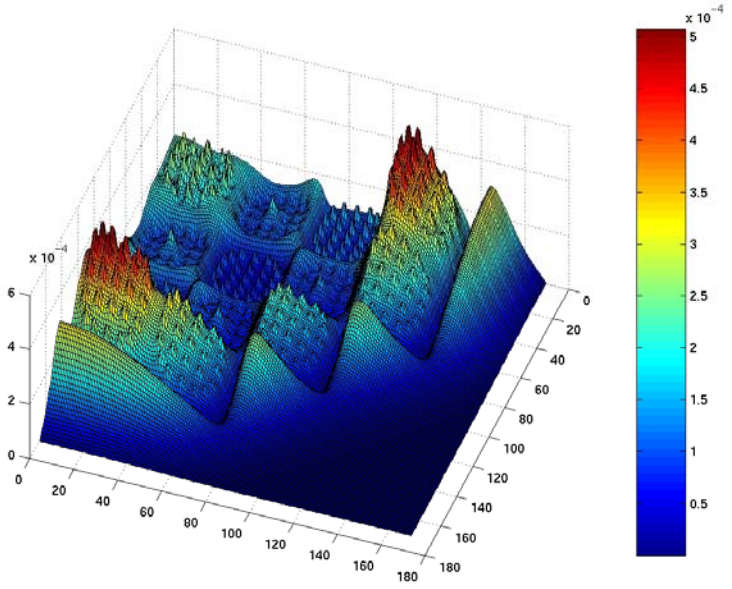

Figure 8.8 7th Group Flux Distribution of the KAIST Core

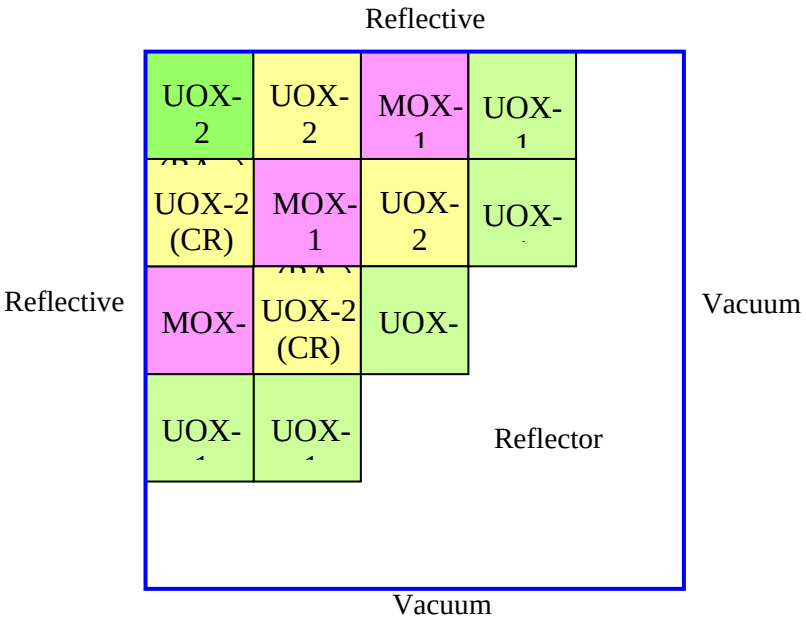

Figure 8.9 Configuration of the Modified KAIST Benchmark Problem (MOX Core)

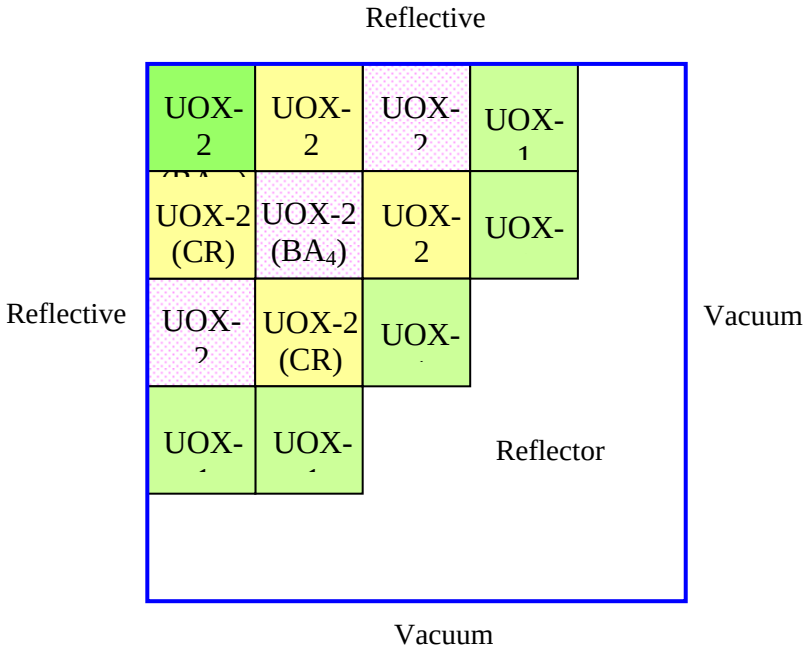

Figure 8.10 Configuration of the Modified KAIST Benchmark Problem (UOX Core)

8.3 Results

8.3.1 Steady-State

The advantages of the global/local acceleration method have been discussed in the previous sections: good performance in convergence, easy parallelization, better performance in solving transient problem, and flexibility in choosing linear solvers. It is worthwhile to investigate in detail the reasons for the advantageous computational efficiency of the two-level (global/local) acceleration method. The performance of the two-level method is compared with the coarse-mesh rebalancing (CMR) method which is one of the conventional acceleration methods, as summarized in Table 8.6.

Table 8.6 Methods Used for Performance Comparison

Method	**Global** (Coarse-Mesh Calculation)	**Local** (Fine-Mesh Calculation)
1	CMFD with $\hat{D}$ correction	"One-node" FDM
2	**CMFD with CMR**	Whore-core FDM

The global/local acceleration method (Method-1) is based on the "one-node" approach in which the fine-mesh finite-difference matrix is constructed for each local node (e.g. FA-size node which has fine calculation meshes) and solved by red-black Gauss-Seidel sweep. In the CMR method (Method-2), the fine-mesh finite-difference matrix is constructed for the whole problem (e.g. whole-core) and the CMR is then performed to set up the coarse-mesh finite-difference matrix.

Tables 8.7 and 8.8 show a comparison of results in terms of computation time for the two different benchmark problems at steady-state conditions. The results show that the performances of those two methods are comparable. Even though Method-1 shows the smallest number of iterations, the total computation time is similar to the other method since the time to solve the local problems is larger than the other method. Therefore, it can be concluded that the global/local acceleration method with the "one-node" scheme at the local level has a performance comparable to the CMR acceleration method for the eigenvalue problem. However, the "one-node" calculation is expected to have an advantage in the transient fixed-source problem which will be analyzed in the following section.

With the two-level (global/local) acceleration, the eigenvalue converges quickly in 3 ~ 4 iterations since the boundary information of the whole problem is quickly transferred throughout the core at the global calculation level. This is similar in characteristics to the techniques using coarser meshes such as the multi-grid method and the coarse-mesh rebalancing method. The only difference is that in the nonlinear global/local approach, the global level is independently solving the problem once correction factors are determined, but in the multi-grid method or the coarse-mesh method, the coarse-mesh calculations are always dependent upon the finer-mesh calculations through residuals or driving factors, respectively. Due to local changes in group fluxes, more iterations are required even though the eigenvalue is almost converged in a few iterations. In the case of SP_3, the convergence is a little slower since one more variable, the 2^{nd}-moment, must be somewhat converged at the same time. Overall, the increase in the number of groups and angles deteriorates convergence behavior. Tables 8.7 and 8.8 also show that SP_3 calculations are about 2 or 3 times slower than diffusion calculations.

Fig. 8.11 and Table 8.9 show comparison of convergences between the whole-core FDM used in PARCS and the two-level acceleration method. As briefly noted in Section 8.1, the FDM module in PARCS uses an efficient numerical combination of the block incomplete LU preconditioner and the BiCG-STAB algorithm as well as the Wielandt acceleration method. Due to the limitation of the FDM module of the PARCS code, only two-group diffusion results are compared. The results show that the two-level method is about four times faster than the FDM module with efficient numerical solvers.

The performance of the three-level acceleration method discussed in Section 7.1 was investigated with multigroup pin-by-pin SP_3 calculations. The results in Fig. 8.12 and Table 8.10 show the better performance of the three-level method compared to the two-level method. Since the two cases chosen here have the similar characteristics in a core size, the number of groups, and the number of spatial meshes, they showed similar results in performance.

Tables 8.11 and 8.12 show the accuracy of pin-by-pin SP_3 methods against more sophisticated transport methods with S_{16}. The ADFs are used in the calculations with FA-homogeneous cross sections. The results show that pin-by-pin 7-group SP_3 results have very good agreement with the reference, while few group results sometimes show good agreement in eigenvalue because of cancellation of errors among the various approximations. However, few group results do not have as good agreement with the reference in the power distribution as the pin-by-pin multigroup SP_3 results. Figs. 8.13 and 8.14 illustrate comparisons of power distributions among different approaches.

It can be summarized that the two-level (global/local) acceleration method for diffusion and SP_3 methods shows better performance compared to the whole-core FDM with the Wielandt acceleration but comparable performance to the CMR acceleration. In addition, the three-level acceleration method, which is applicable to multigroup pin-by-pin SP_3 method, has better

performance in convergence than the two-level acceleration method. As far as the accuracy is concerned, the pin-by-pin multi-group SP_3 method is in best agreement with the reference.

Table 8.7 Performance Comparison between Diffusion and SP_3 in the L336-C5 Benchmark Problem

Group	Mesh/pin	Item	Diffusion		SP_3
			2-Level [a]	CMR [b]	2-Level [a]
2	2x2	CPU	3.7	2.9	8.0
		Iteration	12	20	12
	3x3	CPU	8.2	5.4	22.2
		Iteration	13	15	14
4	2x2	CPU	8.5	8.8	33.2
		Iteration	14	19	16
7	2x2	CPU	32.1	24.5	81.8
		Iteration	22	21	14

a : Global calculation by CMFD and local calculation by one-node FMFD sweep
b : Global calculation by CMR and local calculation by whole-core FMFD matrix
* SUN Ultra2, 300MHz

Table 8.8 Performance Comparison between Diffusion and SP_3 in the KAIST Benchmark Problem

Group	Mesh/pin	Item	Diffusion		SP_3
			2-Level[a]	CMR[b]	2-Level[a]
2	2x2	CPU	10.3	13.6	24.9
		Iteration	13	27	13
	3x3	CPU	25.4	32.0	72.1
		Iteration	13	23	13
4	2x2	CPU	31.1	37.8	94.7
		Iteration	17	24	15
7	2x2	CPU	89.7	82.9	229.6
		Iteration	25	26	21

a : Global calculation by CMFD and local calculation by one-node FMFD sweep
b : Global calculation by CMR and local calculation by whole-core FMFD matrix
* SUN Ultra2, 300MHz

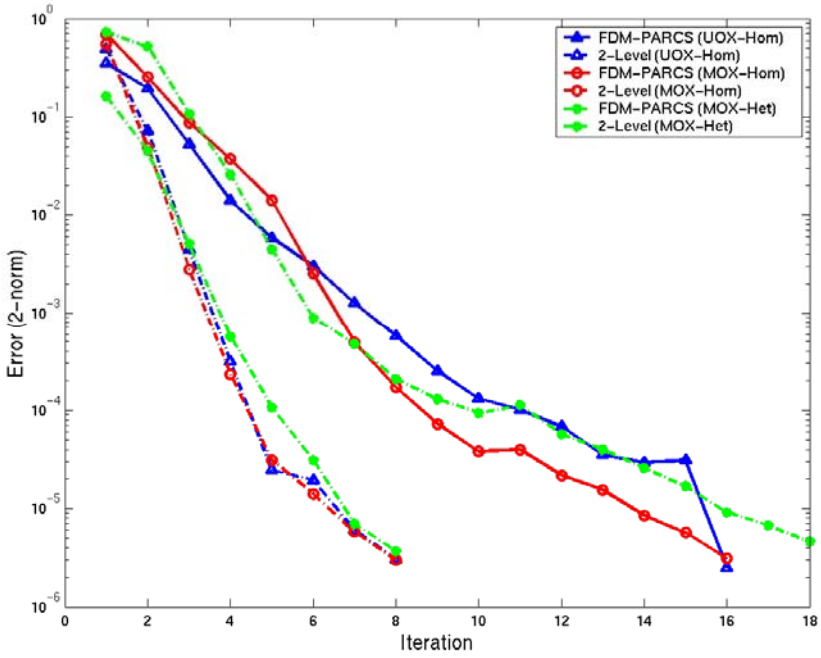

Figure 8.11 Convergence of Conventional FDM (PARCS) and Two-Level Acceleration Method

Table 8.9 Comparison of Computation Time between FDM (PARCS) and Two-Level Acceleration Method

Group	Method	Core	Cross Section	K-eff	CPU (sec)		
					FDM (PARCS)	2-Level	Ratio
2	Diffusion	MOX	FA-HOM	0.95799	76	19	4.0
			PIN-HOM	0.95730	85	24	3.5
		UOX	FA-HOM	0.95283	68	19	3.6

* 51x51 meshes/FA

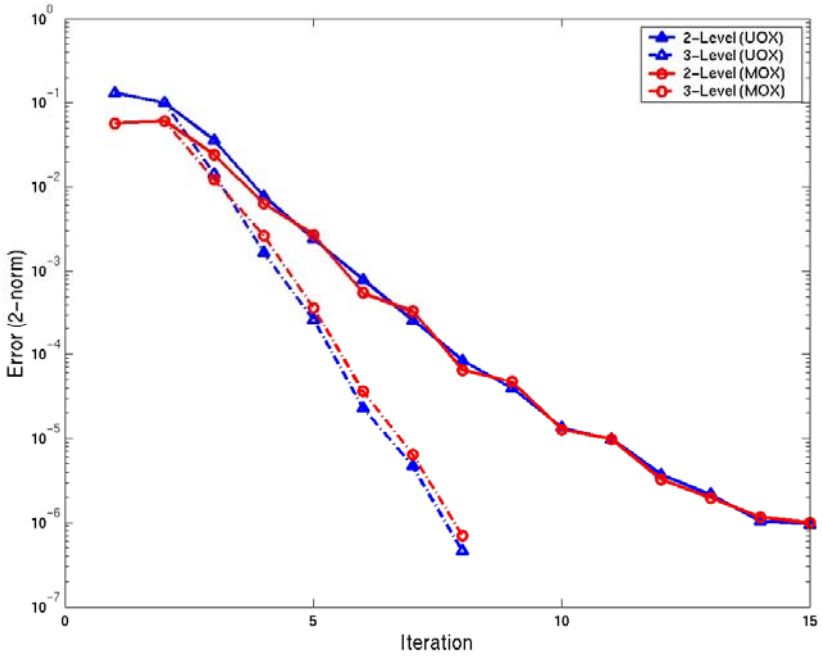

Figure 8.12 Convergence of Two-Level and Three-Level Acceleration Methods

Table 8.10 Comparison of Computation Times between Two-Level and Three-Level Acceleration Methods

Group	Method	Core	Cross Section	K-eff	CPU (sec)		
					2-Level	3-Level	Ratio
7	SP_3	MOX	PIN-Hom	0.95543	561	345	1.6
		UOX	PIN-Hom	0.95234	565	340	1.7

* 3x3 meshes/pin

Table 8.11 Comparison of Eigenvalue and Powers in the Modified KAIST Benchmark Problem (MOX Core)

Code	Group	Method	Cross Section	**K-eff** Delta-K (pcm)	FA Power (% Diff.)	
					Average	Maximum
TWODANT	7	S_{16}	PIN-Hom	0.95521	0	0
PARCS	2	Diffusion	**FA-Hom**	278	1.67	2.67
	7			-142	1.49	4.50
	2	SP_3	FA-Hom	388	1.46	2.30
	7			46	0.64	2.13
	7	SP_3	PIN-Hom	22	0.30	0.82

* PIN-Hom : Pin-homogenized cross sections
* FA-Hom : FA-homogenized cross sections

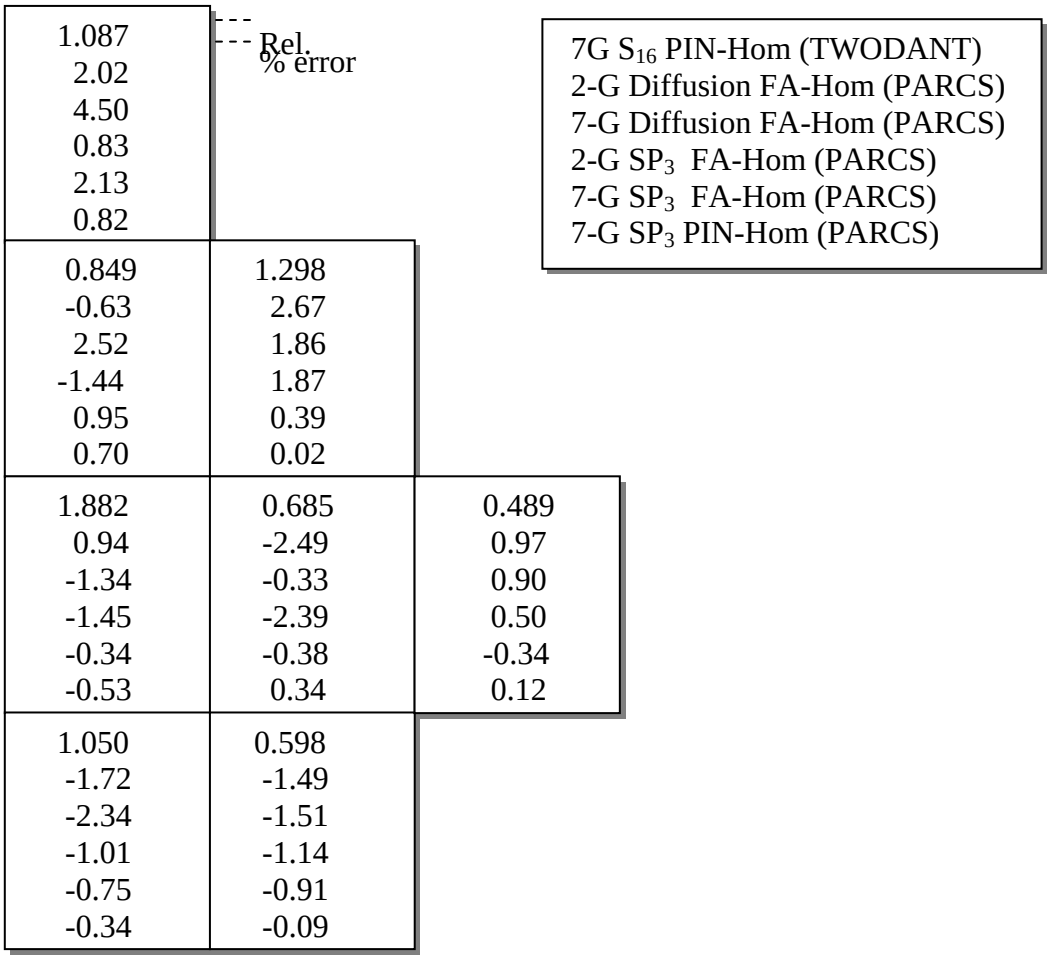

Figure 8.13 Comparison of Power Distributions in the Modified KAIST Benchmark Problem (MOX Core)

Table 8.12 Comparison of Eigenvalue and Powers in the Modified KAIST Benchmark Problem (UOX Core)

Code	Group	Method	Cross Section	**K-eff** Delta-K (pcm)	FA Power (% Diff.)	
					Average	Maximum
TWODANT	7	S_{16}	PIN-Hom	0.95169	0	0
PARCS	2	Diffusion	**FA-Hom**	114	2.42	4.53
	7			-297	1.52	5.22
	2	SP_3	FA-Hom	234	2.18	4.37
	7			110	0.83	3.04
	7	SP_3	PIN-Hom	65	0.26	0.90

* PIN-Hom : Pin-homogenized cross sections
* FA-Hom : FA-homogenized cross sections

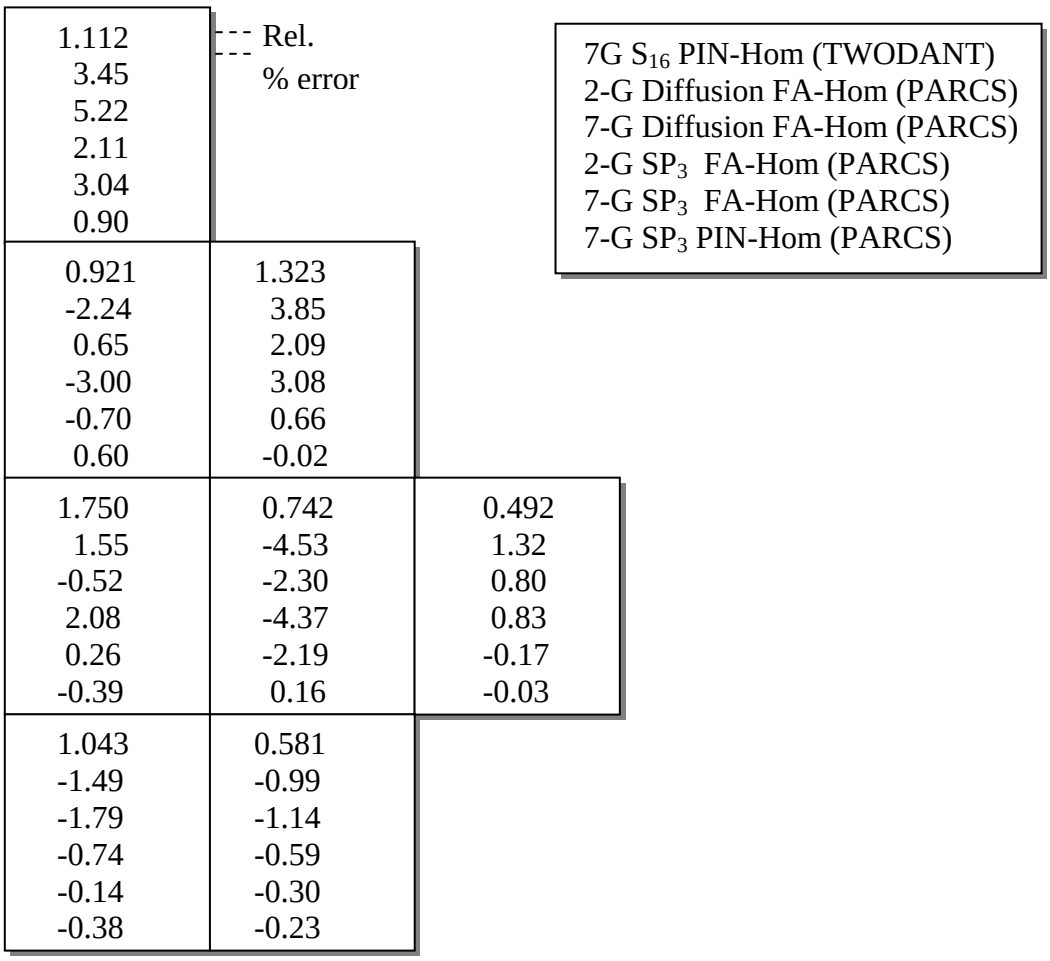

Figure 8.14 Comparison of Power Distributions in the Modified KAIST Benchmark Problem (UOX Core)

8.3.2 Transient

Two types of test cores are constructed for the transient calculations as shown in Figs. 8.15 and 8.16: MOX and UOX Cores. While the MOX core consists of a checkerboard loading of MOX and UOX fuel assemblies (FAs), the UOX core is composed of UOX FAs only. The control rod, which is inserted at the center FA, is ejected in 0.1 sec resulting in super-prompt criticality. The rod ejection is simulated by diluting absorbers in a 2-D geometry. First of all, the newly implemented transient neutronics and thermal-hydraulics (T/H) routines of PARCS have been verified against the ANM transient results of PARCS which have already been well benchmarked. The test cases are run with 2-group FA homogeneous cross sections since the original PARCS with ANM works only with 2-group homogeneous configurations. Fig. 8.17 shows very good agreement between them, which means that the new routines are properly implemented. As mentioned earlier, one of the biggest advantages of the two-level (global/local) acceleration scheme is to save computing time in transient calculations by reducing the number of local calculations depending upon the cross section change:

$$\Delta\Sigma_{\max} = \max\left|\frac{\Sigma_{rg}^{m,i+1} - \Sigma_{rg}^{m,i}}{\Sigma_{rg}^{m,i}}\right| < \varepsilon \qquad (8.3)$$

where $\Sigma_{rg}^{m,i}$ = removal cross section of node m at ith update of correction factors.

The correction factors changes significantly in the node in which the control rod is being removed. However, once the rod is removed, the correction factors changes very small. Fig. 8.18 illustrates the accuracy of using an adaptive update of correction factors, which is in very good agreement with the results without adaptation. In addition, Table 8.13 shows the saving of computation time with an adaptive update of correction factors. If the transient calculations are performed more than 0.6 sec, the CPU saving would be greater.

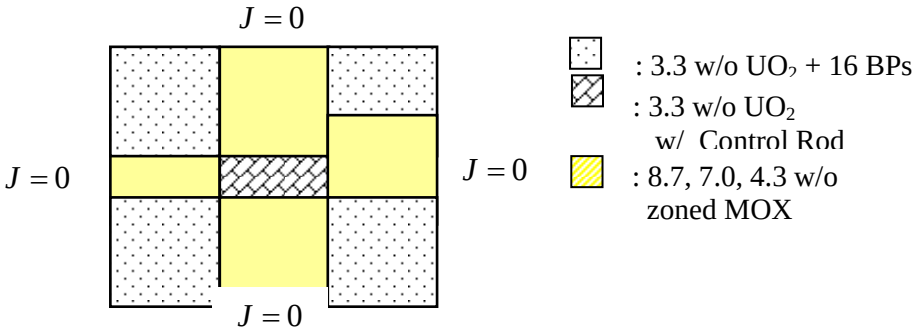

Figure 8.15 Configuration of 3x3 MOX Core for the Rod Ejection Transient Problem

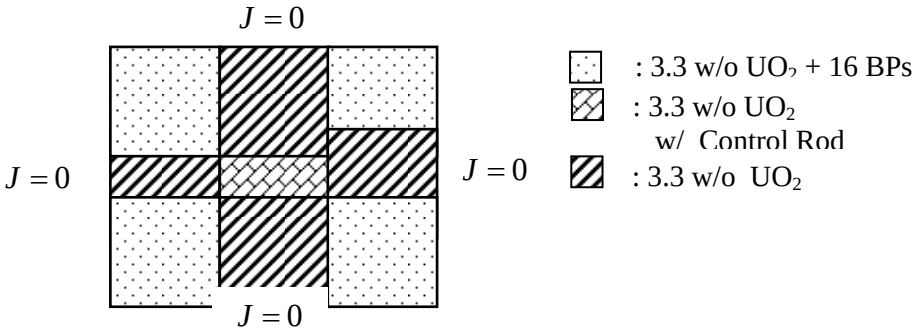

Figure 8.16 Configuration of 3x3 UOX Core for the Rod Ejection Transient Problem

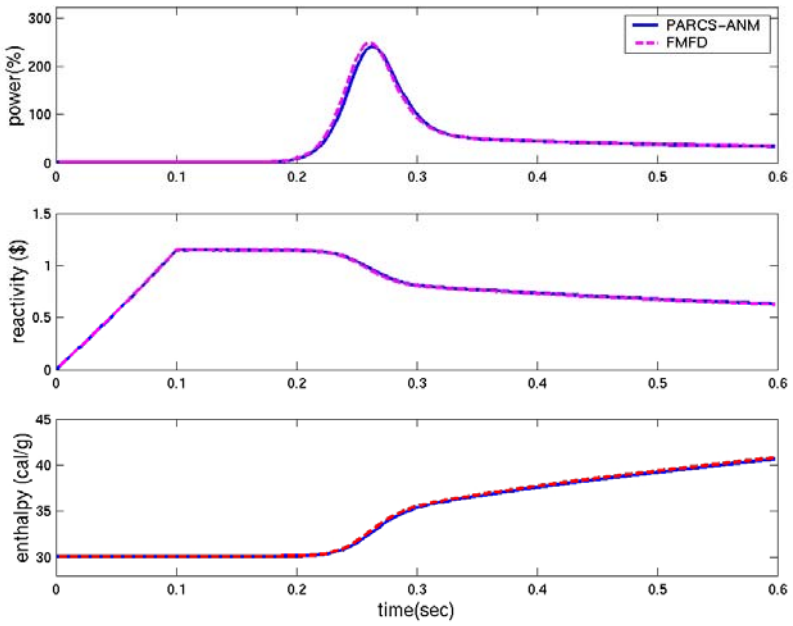

Figure 8.17 Comparison of Power, Reactivity, and Enthalpy with Time between PARCS-ANM and FMFD Diffusion in the MOX-Core Transient

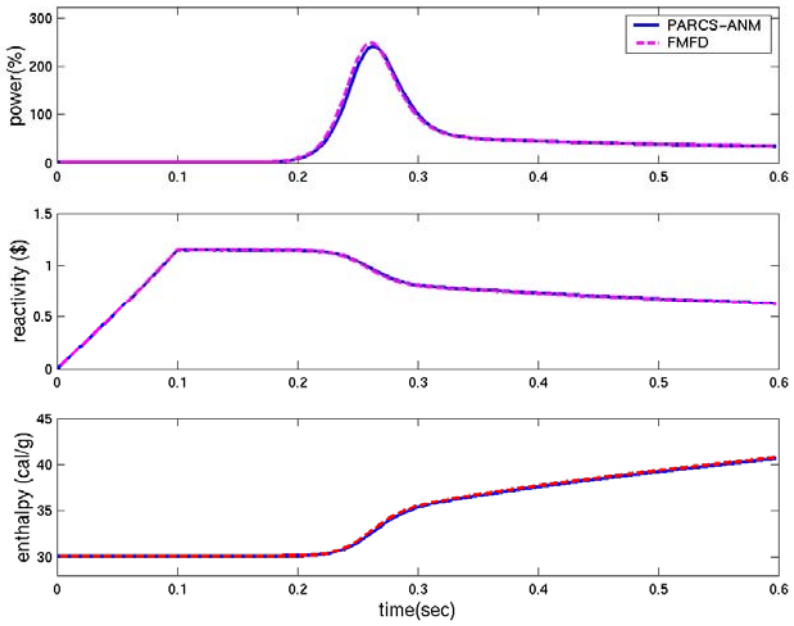

Figure 8.18 Comparison of Power, Reactivity, and Enthalpy with Time between PARCS-ANM and FMFD Diffusion w/ Adaptation in the MOX-Core Transient

Table 8.13 Reduction of Computation Time Due to Adaptation with Cross Section Change (Total elapsed time = 0.6 sec)

CORE	Method *	w/o Adaptation (sec)	w/ Adaptation (sec)	Ratio
MOX	Diffusion	219	41	0.19
	SP_3	393	123	0.31
UOX	Diffusion	226	42	0.19
	SP_3	348	71	0.20

* 2-group, FA-homogeneous, 2x2 meshes/pin
Note that the CPU reduction will become larger with greater total elapsed time

It is very worthwhile to compare the transient results of the two different cores, which have the same dynamic reactivities. As shown in Table 8.14, the MOX core has a smaller delayed neutron fraction and generation time, which causes the earlier core power peak. It is instructive to understand the trend using the simple point kinetics equations:

$$\dot{p}(t) = \frac{\rho(t) + \gamma \int_0^t \left(p(t') - p_0\right)\, dt' - \beta}{\Lambda} p(t) + \frac{1}{\Lambda} \sum_k \lambda_k \varsigma_k \,, \qquad (8.4)$$

where $\dot{\varsigma}(t) = -\lambda_k \varsigma_k(t) + \beta_k p(t)$.

In the super-prompt critical domain Eq. (8.4) at hot zero power conditions, the solution can be approximated as [Ott, 1989]:

$$p(t) = \exp\left(\frac{\rho_1 - \beta}{\Lambda} t\right) p_0 \,, \quad p_{\max} = -\frac{\rho_b^2}{2\Lambda\gamma} \,, \quad \overline{\Delta t} = \frac{4\Lambda}{\rho_1 - \beta} \,, \qquad (8.5)$$

where $\rho_b^2 = (\rho_1 - \beta)^2 - \dfrac{2\Lambda\gamma\rho_1}{\rho_1 - \beta} p_0 \approx (\rho_1 - \beta)^2$, $\rho_1 = \rho(t) + \gamma \int_0^t (p(t') - p_0)\, dt'$,

$\gamma < 0$ (thermal feedback coefficient).

The equation above implies that the height of the power peak is dependent upon $(\rho_1 / \beta - 1)^2$, Λ / β, and γ / β. In addition, the energy stored in the power peak becomes only dependent upon ρ_1 / β and γ / β as follows:

$$p_{\max} \overline{\Delta t} \approx -\frac{2(\rho_1 - \beta)}{\gamma} \tag{8.6}$$

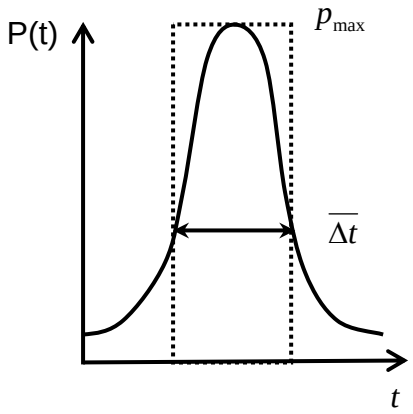

Figure 8.19 Power Pulse of the Superprompt-critical Transient

According to the MOX and UOX transient results with the same dynamic reactivities, the MOX core should have relatively earlier and smaller power peak and smaller stored energy. The trend can be estimated using Eqs. (8.5) and (8.6) with data in Table 8.14. These are shown in the comparison results in Fig. 8.20. More tests are performed with the same cores changing the methods from diffusion and SP_3 approximations using 2-group homogeneous cross sections.

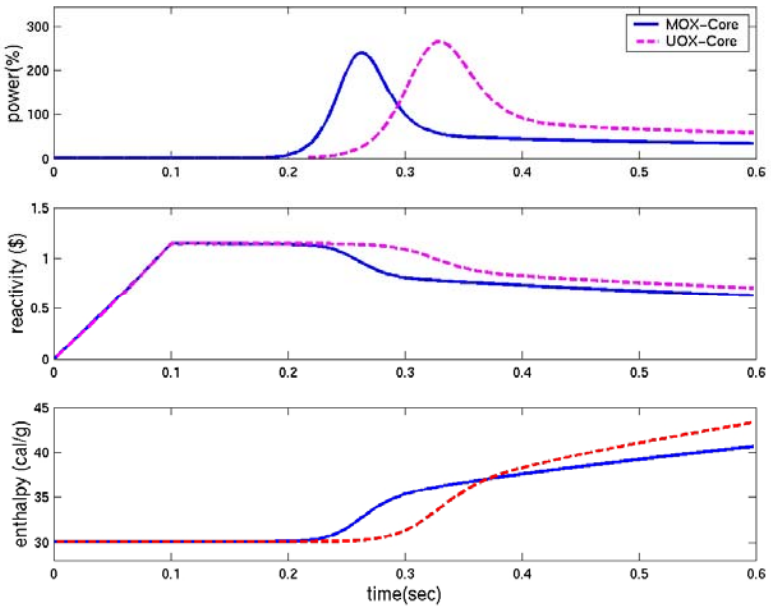

Figure 8.20 Comparison of Results between MOX and UOX Core Transients

Table 8.14 Transient Parameters of MOX and UOX Cores

PARAMETER	MOX	UOX	Ratio
Initial K-eff	1.00029	0.99998	-
Beta	0.0053	0.0076	1.43
Reactivity ($)	1.14	1.14	1
Λ	1.31×10^{-5}	2.16×10^{-5}	1.65
Λ / β	0.0025	0.0028	1.12
Doppler Coefficient (pcm/°C)(1)	-3.4	-3.1	0.91
$(1) / \beta$	-642	-408	0.64

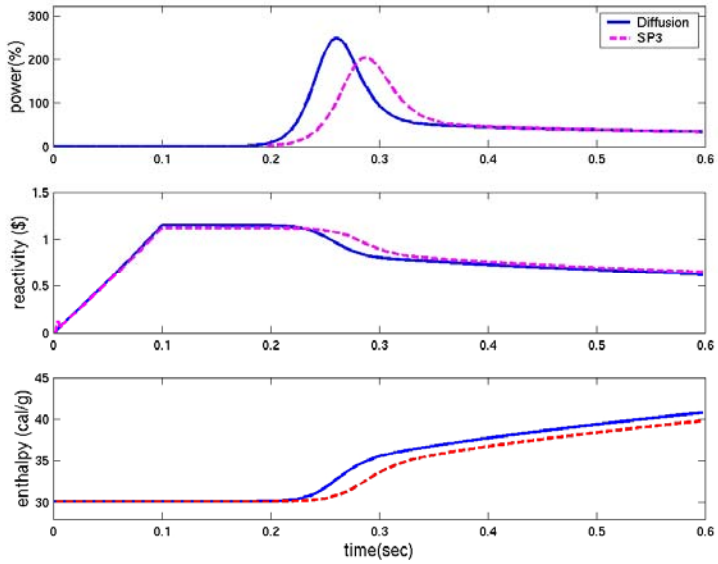

Figure 8.21 Comparison of Power, Reactivity, and Enthalpy with Time between Diffusion and SP_3 in the MOX-Core Transient

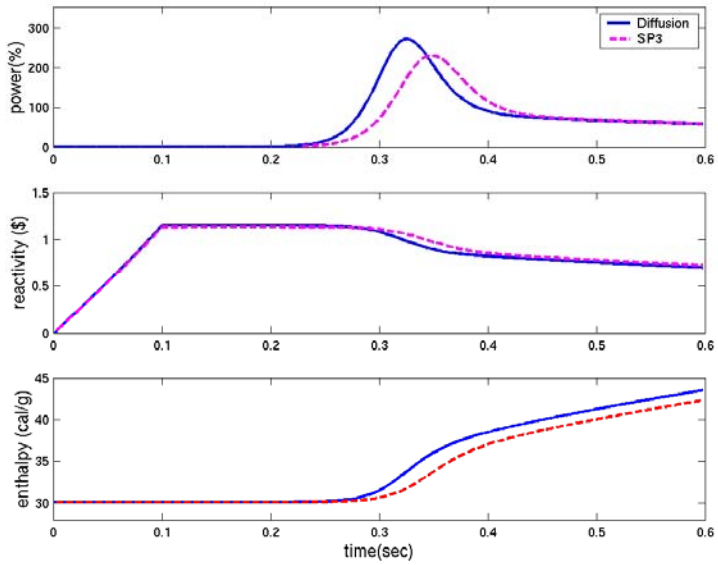

Figure 8.22 Comparison of Power, Reactivity, and Enthalpy with Time between Diffusion and SP_3 in the UOX-Core Transient

The different methods result in different control rod worth in the steady-state calculation, which significantly affects the transient results as shown Figs. 8.21 and 8.22. Even though the difference of delayed neutron fractions between 2-group FA-homogenous diffusion and multigroup pin-by-pin SP_3 calculations is one of the major effects for transient results, its investigation and analysis remain as future work.

8.4 Performance of Multigroup SP_3 Nodal Expansion Method

The conventional methods used to solve the NEM is to perform one-dimensional sweeping with numerical schemes such as the red-black Gauss-Seidel and then perform acceleration with coarse-mesh rebalancing, Chebyshev method, etc. In this work the multigroup NEM is solved within the framework of the global/local acceleration method, which was discussed in the previous sections. Even though one-dimesional sweeping works well with the global/local iteration for 2-group problems, it turns out to have poor convergence for multigroup SP_3 problems. This is the primary reason why the simultaneous matrix solution method is proposed as discussed in Section 5. Determining all directional currents, higher cofficients, and average flux of a node at a time makes it possibe to obtain a stable correction factors.

As explained in the SP_3 solution with the FMFD method, the 2-group diffusion equation is solved with CMFD in the global calculation whereas the multigroup SP_3 equation is solved with NEM in the local calculation. The 2^{nd} moments as a boundary condition for the local problem are determined from the previous iteration step. The restriction and prolongation of group information between 2-group CMFD and multigroup NEM are performed in the same way as explained in Section 6. The 13×13 matrix equation shown in Eq. (5.16) are solved using LU factorization.

The multigroup NEM for the SP_3 equation has been implemented into the PARCS code and tested using the modified KAIST benchmark problem as shown in Figs. 8.23 and 8.24. Figs. 8.25 and 8.26 show two-group moment shapes of FMFD SP_3 and nodal SP_3 along the top edge line of the core for the MOX benchmark, and Figs. 8.27 and 8.28 show the moments for the UOX benchmark. The 0^{th} moment comparisons show that the nodal SP_3 has good agreement with FMFD SP_3 at interfaces between different types of fuel assemblies, which enables the nodal solution to have good approximations of the eigenvalue and power distribution. However, the 2^{nd} moment results show that even though the trend in moment distribution is correct, the accuracy of the slope of the moment is not as good as the 0^{th} moment at interfaces. This implies that the 2^{nd} moments might not be sufficiently well approximated with a second-order polynomial, and future work will be to investigate the use of the exponential functions to estimate the steep change of the 2^{nd} moment at interfaces. Nevertheless, the nodal SP_3 results have very good accuracy because the influence of 2^{nd} moments on scalar fluxes and currents is relatively small. Figs. 8.29 through 8.34 illustrate the comparisons of moment distributions from multigroup SP_3 calculations.

Tables 8.15 and 8.16 show the comparison of eigenvalue and computing time between FMFD and nodal methods in the diffusion and SP_3 equations. As many researchers have shown, the NEM for the diffusion equation has very good agreement with the FMFD solutions. The SP_3 NEM also has good agreement with FMFD SP_3 results.

As expected, there is large reduction of about a factor of more than 100 in the calculation times in two-group. The reason why the CPU reduction is much smaller in 7-group is because the method of solving the local problems is changed in the 7-group cases. While one-dimensional sweeping is used in 2-group, the LU factorization to solve the 13×13 matrix shown in Eq. (5.16) is used in the 7-group cases. If the 2-group solver is changed to the LU factorization for the 13x13 matrix, the CPU difference will be smaller. As future work, the LU factorization will be changed to more efficient numerical methods and the computing time will then be reduced.

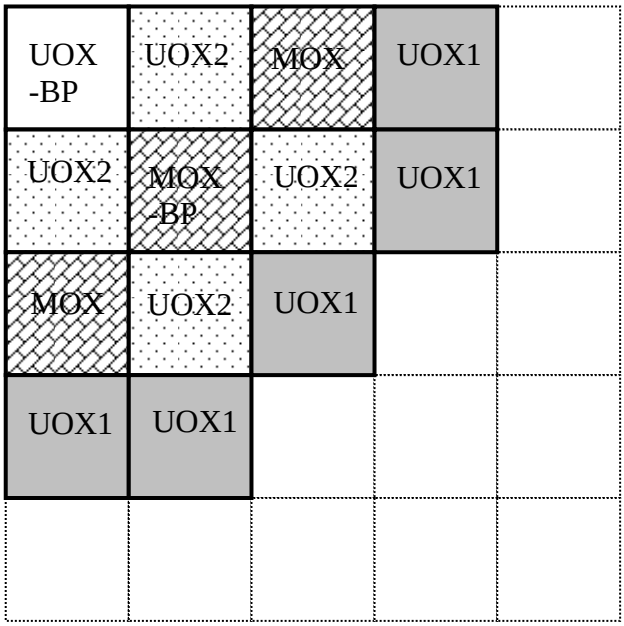

Figure 8.23 MOX Core Solved with the Multigroup SP_3 NEM

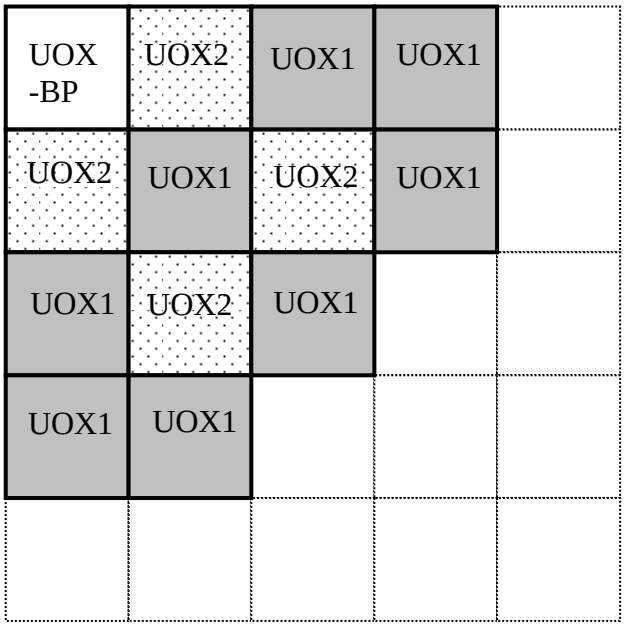

Figure 8.24 UOX Core Solved with the Multigroup SP_3 NEM

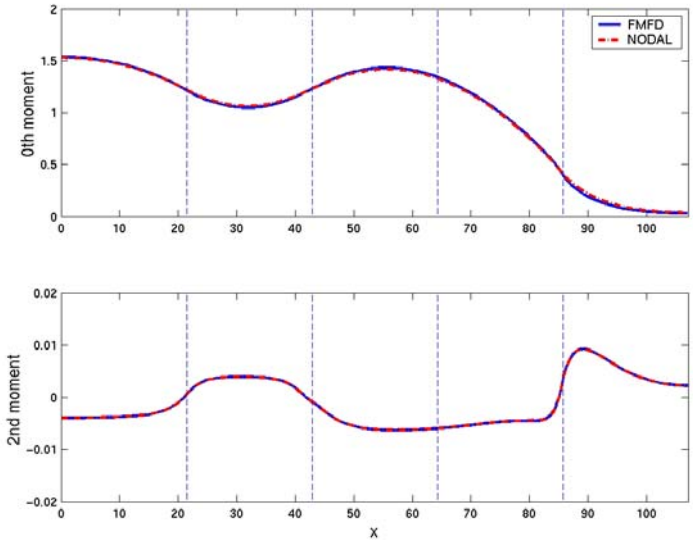

Figure 8.25 Fast Group Moments along the Top Boundary Line in the UOX Benchmark

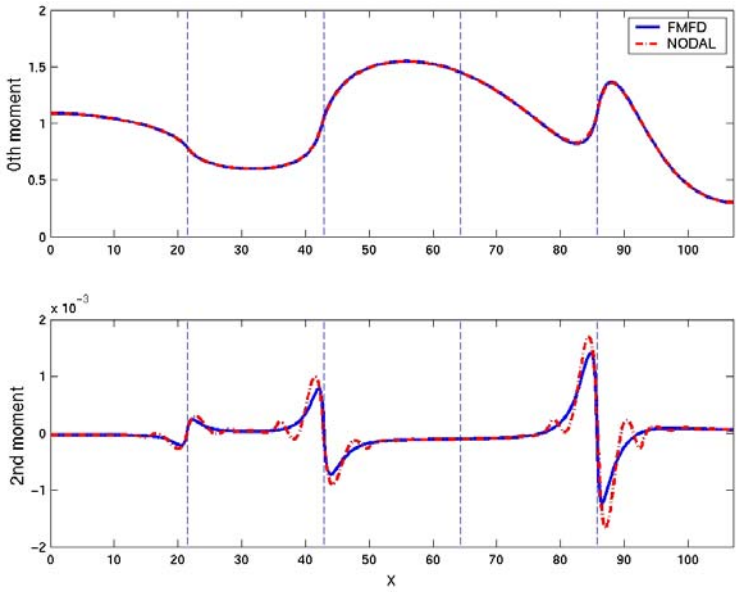

Figure 8.26 Thermal Group Moments along the Top Boundary Line in the UOX Benchmark

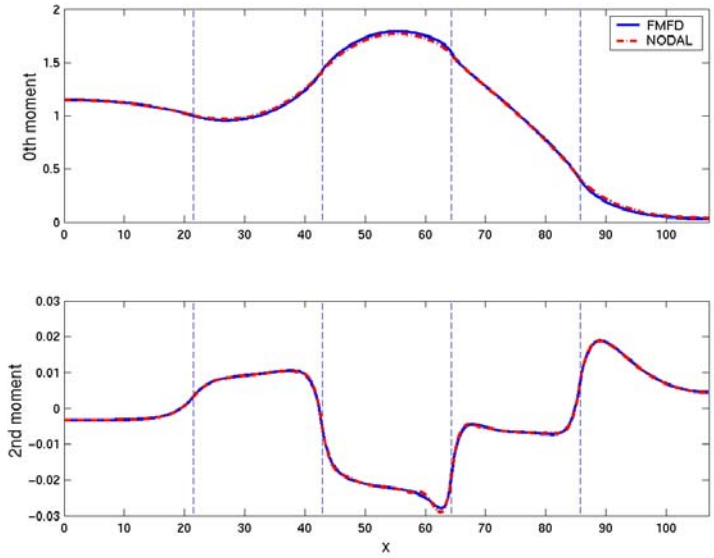

Figure 8.27 Fast Group Moments in 2-Group along the Top Boundary Line in the MOX Benchmark

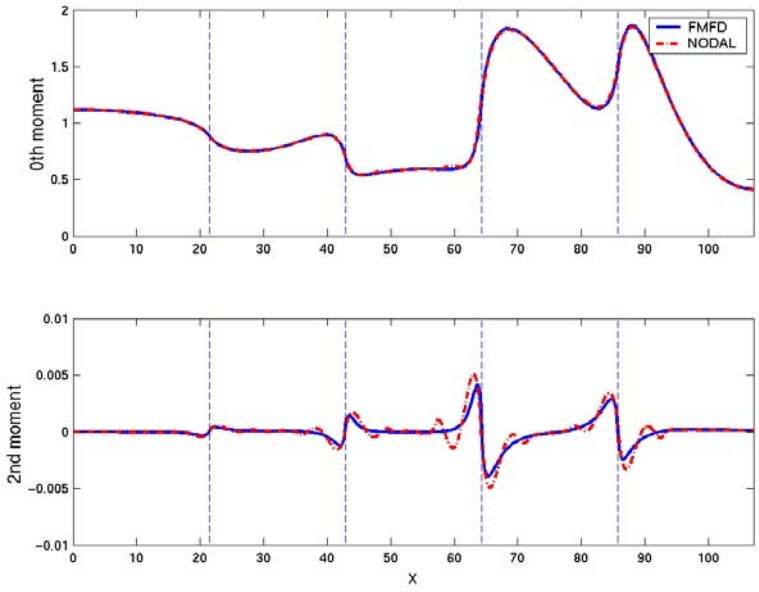

Figure 8.28 Thermal Group Moments in 2-Group along the Top Boundary Line in the MOX Benchmark

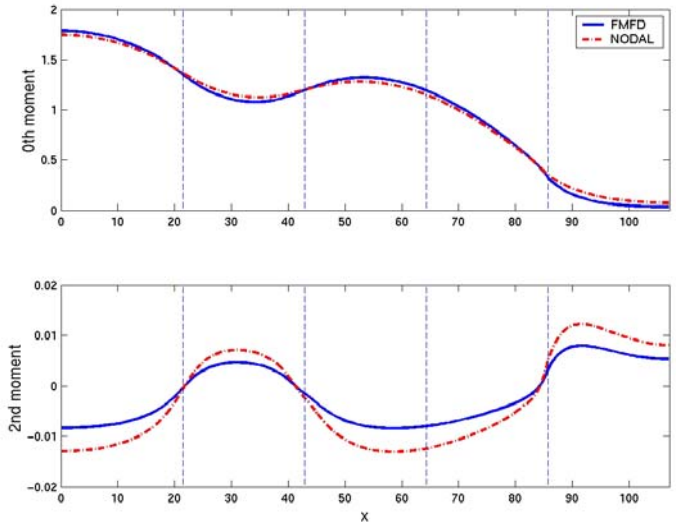

Figure 8.29 Group-1 Moments of 7-Group Solution along the Top Boundary Line in the UOX Benchmark

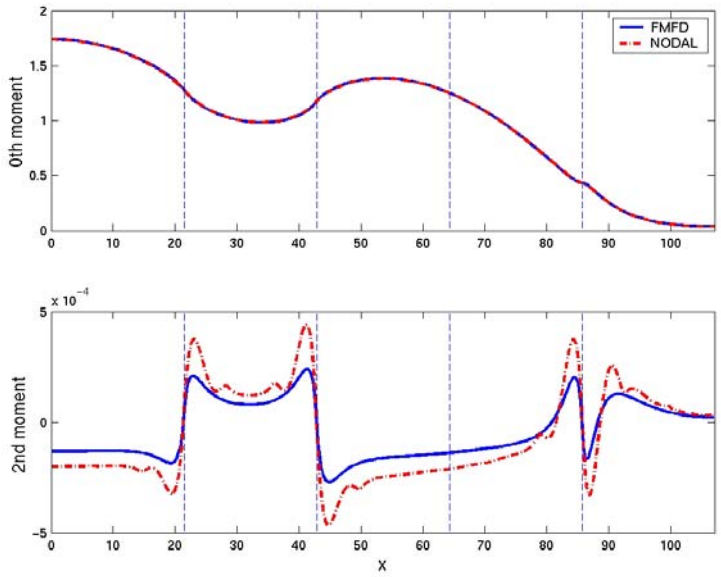

Figure 8.30 Group-4 Moments of 7-Group Solution along the Top Boundary Line in the UOX Benchmark

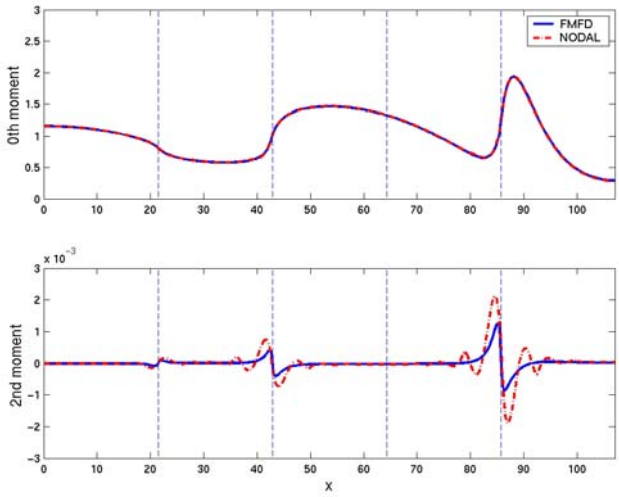

Figure 8.31 Group-7 Moments of 7-Group Solution along the Top Boundary Line in the UOX Benchmark

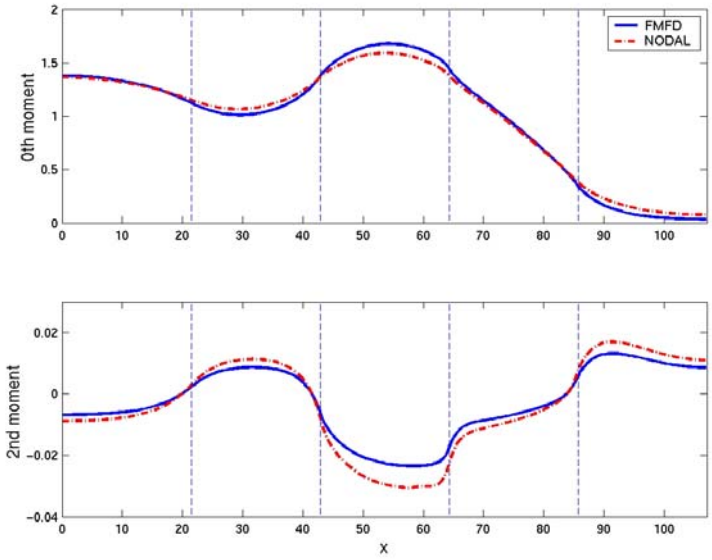

Figure 8.32 Group-1 Moments of 7-Group Solution along the Top Boundary Line in the MOX Benchmark

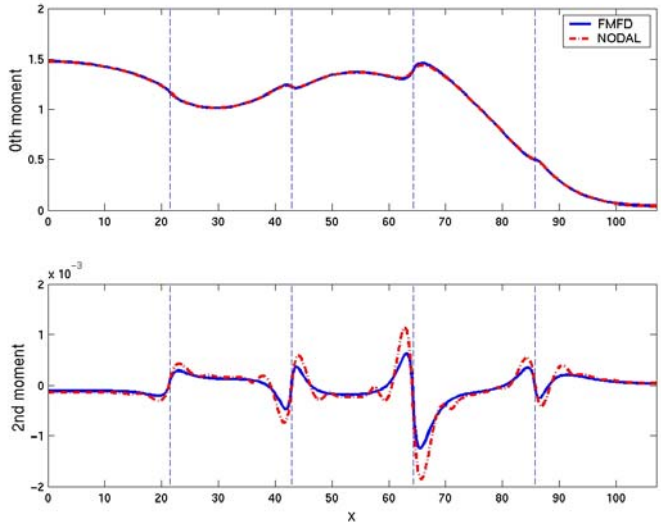

Figure 8.33 Group-4 Moments of 7-Group Solution along the Top Boundary Line in the MOX Benchmark

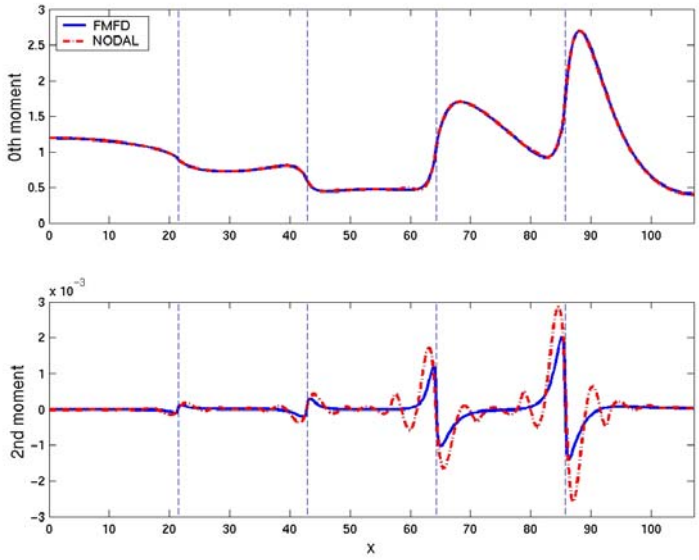

Figure 8.34 Group-7 Moments of 7-Group Solution along the Top Boundary Line in the MOX Benchmark

Table 8.15 Comparison of Eigenvalue and Computation Time between FMFD and Nodal SP_3 Methods for the MOX Benchmark Problem

Grp	Item	Diffusion		Delta-K	RMS	SP_3		Delta-K	RMS
		FMFD	NODAL	(Ratio)	(Max)	FMFD	NODAL	(Ratio)	(Max)
2	k-eff	0.97579	0.97581	2	0.06 (0.10)	0.97795	0.97794	-1	0.05 (0.08)
	G/L Iter	18	5	-		19	8	-	
	CPU(s)	42.1	0.2	(211)		67.0	0.5	(134)	
7	k-eff	0.98466	0.98468	2	0.09 (0.19)	0.98778	0.98781	3	0.11 (0.24)
	G/L Iter	16	17	-		17	16	-	
	CPU(s)	145.6	5.6	(26)		390.7	10.6	(37)	

1) Calculation mesh: FMFD – 51×51/pin, NODAL – 3×3/FA
2) Note that since 2-group cross sections are not generated in consistence with 7-group cross sections, their results in eigenvalues and powers are not comparable each other.
3) No upscattering cross sections are considered in 7-group calculations
4) SUN Ultra2, 450 MHz

Table 8.16 Comparison of Eigenvalue and Computation Time between FMFD and Nodal SP_3 Methods for the UOX Benchmark Problem

Group	Item	Diffusion		Delta-K	RMS Error of Power	SP_3		Delta-K	RMS Error of Power
		FMFD	NODAL	(Ratio)	(Max)	FMFD	NODAL	(Ratio)	(Max)
2	k-eff	0.93819	0.93820	1	0.07	0.93989	0.93988	-1	0.04
	G/L Iter	18	6	-	(0.14)	18	8	-	(0.09)
	CPU(s)	37.8	0.3	(126)		62.9	0.5	(126)	
7	k-eff	0.95619	0.95619	0	0.07	0.95847	0.95852	5	0.08
	G/L Iter	21	22	-	(0.14)	23	23	-	(0.14)
	CPU(s)	208.0	8.1	(26)		392.6	19.5	(20)	

1) Calculation mesh: FMFD – 51×51/pin, NODAL – 3×3/FA
2) Note that since 2-group cross sections are not generated in consistence with 7-group cross sections, their results in eigenvalues and powers are not comparable each other.
3) No upscattering cross sections are considered in 7-group calculations
4) SUN Ultra2, 450 MHz

8.5 Performance of the Adaptive Method

Since the multigroup pin-by-pin SP_3 calculation with the FMFD method still has large computation time compared to the conventional approach using the advanced nodal method with 2-group FA homogenized cross sections, the adaptive method is experimented here, in which the different methods are used in the same core calculation. For example, the multigroup pin-by-pin SP_3 method is used in the regions in need, and nodal methods, which are computationally efficient, are used in the other regions. This adaptive method was verified against the modified KAIST benchmark problem with the choise of methods shown in Figs. 8.35 and 8.36.

As shown in Fig. 8.35, the SP_3 method is mainly assigned to MOX regions and interface regions between fuel assemblies and reflector where the transport effect is expected to be dominant. Since the total computation time is so small, it is not easy to make conclusion. According to the results shown in Table 8.17, however, Case-3 is a kind of optimum choice in terms of accuracy and computation time as can be expected, which SP_3 is assigned to MOX FAs and reflector nodes adjacent to fuel assemblies. Fig. 8.36 and Table 8.18 show performance depending upon the choice of methods with pin-by-pin FMFD and nodal methods in which only 2 group cross sections are used. Cases 2 through 6 list a spectrum of change of accuracy and computation time. Based upon the results, Case 5 is most desirable in terms of both accuracy and computatin time.

It will be interesting to investigate how to optimize the choice of methods. Furthermore, to show significant performance improvement of the adaptive method, the multigroup and pin-by-pin SP_3 methods need to be involved. It remains as one of possible future extensions of this report.

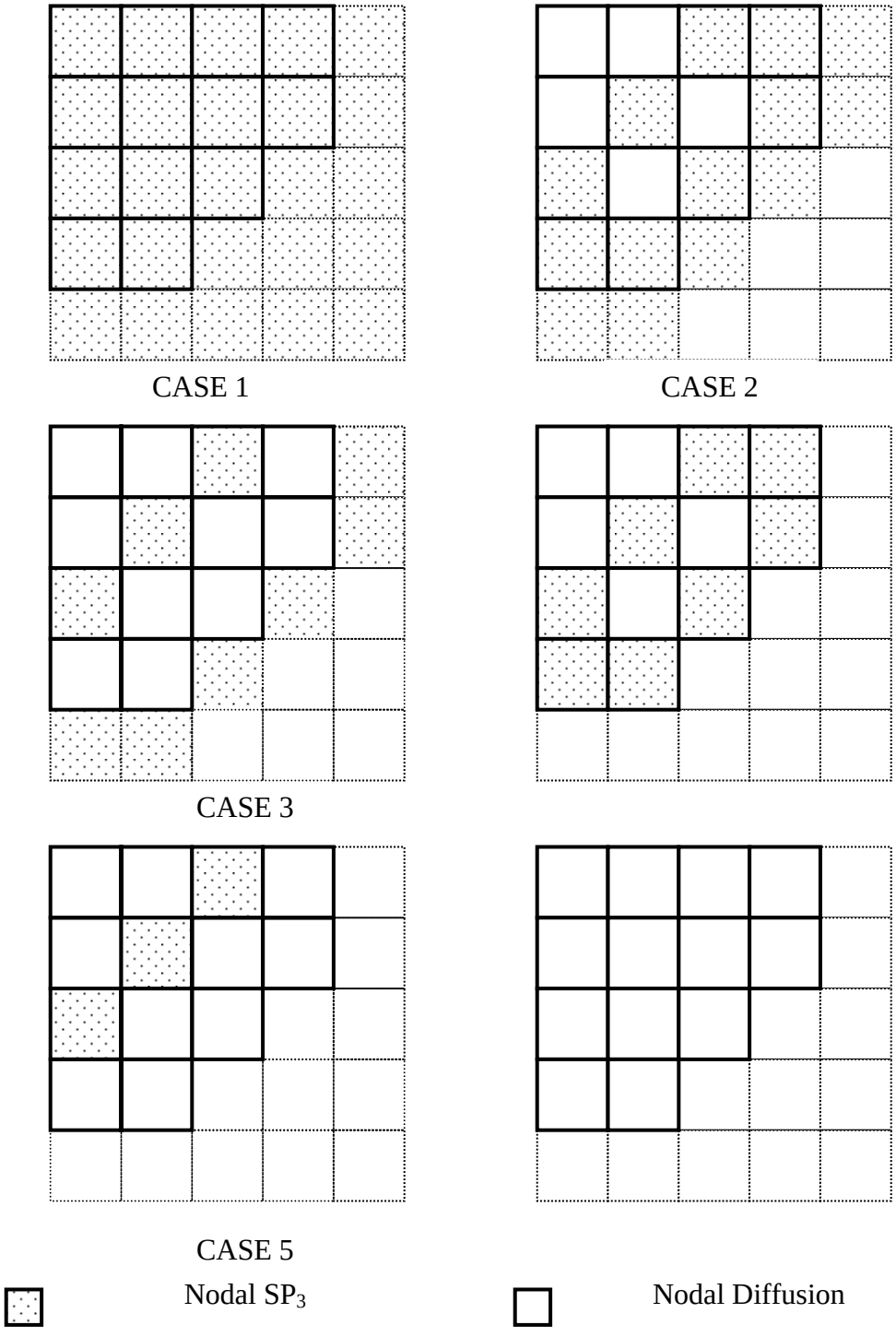

Figure 8.35 Assignment of Solvers in the Adaptive Method with Nodal Methods

Table 8.17 Comparison of Eigenvalue and Power with Choice of Different Methods in 2-Group FA-Homogeneous Problem (Use of Nodal Methods Only)

CASE	FMFD	NODAL		K-eff (Delta-K, pcm)	% Error of Power RMS (Max)	CPU (sec)
	SP_3	SP_3	Diff			
Ref	25	0	0	0.97795	-	72.2
1	0	25	0	(-1)	0.04 (0.09)	3.1
2	0	14	11	(-27)	0.38 (0.82)	2.8
3	0	9	16	(-37)	0.69 (0.84)	2.5
4	0	8	17	(-72)	0.48 (0.85)	2.5
5	0	3	22	(-87)	1.03 (1.49)	2.4
6	0	0	25	(-214)	1.19 (1.99)	2.0

* FMFD = 51x51/pin, NODAL = 3x3/FA
* criterion = 10^{-6}
* SUN Ultra2, 450 MHz

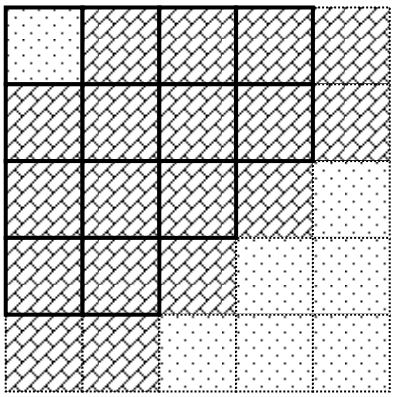

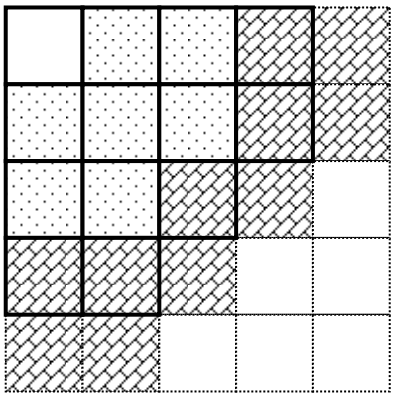

CASE 2

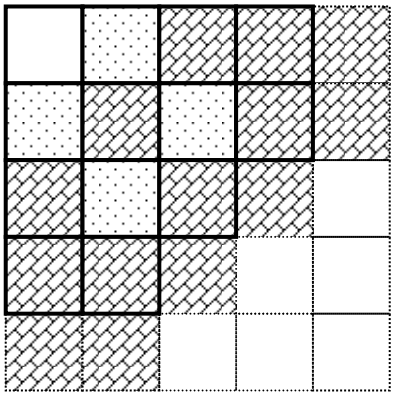

CASE 4

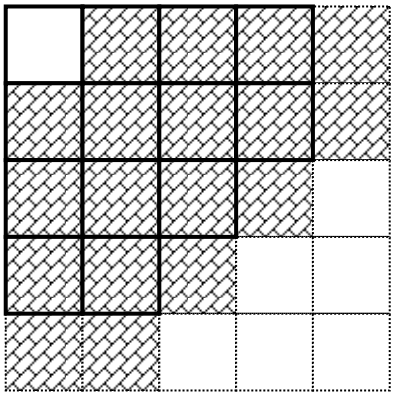

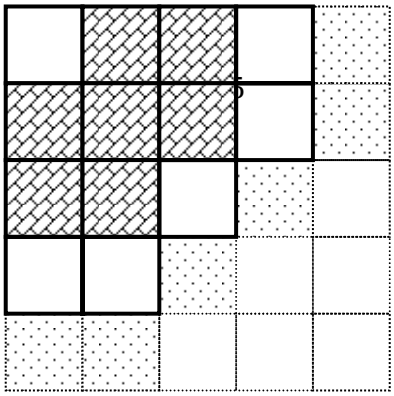

CASE 7 = CASE 6 in Fig. 8.35

Nodal Diffusion (Reflector)

Figure 8.36 Assignment of Solvers in the Adaptive Method with Nodal and FMFD Methods

Table 8.18 Comparison of Eigenvalue and Power with Choice of Different Methods in 2-Group FA-Heterogeneous Problem (Use of Nodal and FMFD Methods)

CASE	FMFD	NODAL		K-eff (Delta-K, pcm)	% Error of Power RMS (Max)	CPU (sec)
	SP_3	SP_3	Diff			
Ref	25	0	0	0.96440	-	44.7
1	18	7	0	(7)	0.06 (0.14)	33.6
2	18	0	7	(6)	0.06 (0.14)	32.3
3	14	4	7	(88)	0.95 (1.90)	26.9
4	11	7	7	(43)	0.85 (1.57)	22.4
5	7	6	12	(-3)	0.22 (0.41)	14.4
6	0	25	0	(83)	0.83 (1.64)	3.4
7	0	0	25	(-101)	1.03 (2.59)	2.0

* FMFD = 3x3/pin, NODAL = 3x3/FA
* criterion = 10^{-6}
* SUN Ultra2, 450 MHz

9. SUMMARY AND CONCLUSIONS

The sources of error involved in the solution of the Boltzmann transport equation, such as spatial discretization, spatial homogenization, group collapsing, and transport, were qualitatively and quantitatively evaluated for the solution of core neutronics problems in LWRs. Basically, all errors occur due to differences in spectrum conditions between group constants generated in lattice calculation and used in core calculation. For example, if all group constants are generated under the actual spectrum conditions, very accurate solutions can be obtained. However, it is in fact impossible to know the actual spectrum conditions when generating group constants. Based upon test calculations described in Section 2, it was found that heterogeneous multigroup transport calculations are necessary to accurately predict eigenvalue and fuel pin powers for tightly coupled MOX loaded cores. Multigroup transport calculations with pin-by-pin configurations are relatively less sensitive to the spectrum condition in which group constants are provided. Since the multigroup transport equation for pin-by-pin core configurations requires a large amount of computation time, it is formulated within a framework of the multi-level acceleration method, which enhances the computational efficiency for both eigenvalue and fixed source problems.

The local spatial calculation is performed using the fine-mesh finite difference (FMFD) method instead of the traditional nodal method since the heterogeneity inside fuel assemblies can be treated directly. In addition, the so-called “one-node two-factor” scheme (one-node local calculation resulting in two correction factors at each side of a node) in the global/local multi-level acceleration is adopted instead of the “two-node one-factor” scheme (two adjacent local node calculations resulting in one correction factor at the interface). The “one-node two-factor” scheme has advantages in terms of computational efficiency and in terms of treatment of heterogeneous configurations. The simplified P_3 approximation (SP_3) is used as a transport solver because of its favorable characteristics in terms of accuracy and computing time. The heterogeneous configuration with pin-homogenized cross sections is also adopted to minimize the spatial homogenization error and especially to improve estimates of pin powers. In order to reduce the computation time and enhance the convergence rate, the two-group diffusion calculation with homogenized cross sections is maintained at the global level while the multigroup pin-by-pin SP_3 calculation is performed only at the local level. In addition, adaptive methods are implemented, which enable the use of solvers with different levels of complexity within the same core calculation. For the adaptive method, the multigroup nodal expansion method (NEM) for the SP_3 approximation has been developed and investigated. In the efficient formulation of NEM for SP_3, the definition of partial moments is modified appropriately.

The methodologies developed in this report have been verified for steady-state and transient calculations using the OECD L336 benchmark and the modified KAIST benchmark problems, both of which included MOX fuels and were solved using 7-group homogenized cell cross sections. The results show that the multi-level acceleration method for the SP_3

approximation is successful for steady-state conditions in terms of both accuracy and computation time. It was also observed that the global/local multi-level scheme for the multigroup SP_3 formulation is more efficient for the transient fixed source problem since correction factors for the CMFD calculation can be reused during mild transient periods without being explicitly recalculated. The multigroup SP_3 NEM, which was used in the adaptive method, has very good agreement in 2-group and 7-group test problems. The adaptive method also showed expected performance in terms of accuracy and computation time depending upon the choice of methods.

The principal original contributions of this work are the formulation of pin-by-pin multigroup SP_3 approximation within a framework of the multi-level global/local acceleration approach for the steady-state and transient conditions, the development of multigroup NEM for SP_3, and the development of the adaptive techniques for the methods proposed here. In the future, the multigroup pin-by-pin SP_3 method should be verified with more sophisticated reference calculations, such as full core calculations with the Lattice codes. The cell-homogenization factors, such as the superhomogenization (SPH) factors, will then need to be considered. In addition, the performance of the multi-level acceleration method needs to be compared more systematically with other advanced acceleration techniques.

As for transient calculations, it would be also worthwhile to compare kinetics parameters determined using the conventional methods and those obtained from the pin-by-pin multigroup SP_3 calculations, and to analyze their effects on transient behaviors in terms of power peak and energy deposition. The multigroup pin-by-pin SP_3 should be extended to three dimensions for more realistic simulation of rod ejection transients. In order to save computation time in three-dimensional calculations, nodal methods can be used in the z-direction, since compositions are normally homogeneous in the z-direction. The transverse leakage shapes for the pin-by-pin configuration then need to be appropriately established, which would be different from the conventional approximations of the transverse leakage shapes for the FA-homogeneous configuration. As for the nodal expansion method for SP_3, the polynomial approximation of the second moments and their transverse leakage shapes need to be improved for better accuracy with coarser meshes. Nodal methods for diffusion and SP_3 approximations also need to be investigated together with the equivalence theory, since they will have different discontinuity factors to preserve reference currents at assembly interfaces. Even though the adaptive method was tested with the “one-node two-factor” scheme in this work, it will be interesting to perform the adaptive calculations with the “two-node one-factor” scheme since multigroup or transport effects are actually dominant at interfaces between two different assemblies or interfaces between fuel assemblies and reflector. The choice of appropriate methods in the adaptive method will have to be optimized based upon systematic error analysis in association with the specific core.

10. List of References for PART I

[Adams, 1992] M. L. Adams and W. R. Martin, "Diffusion Synthetic Acceleration of Discontinuous Finite Element Transport Iterations," Nucl. Sci. Eng., 111, 145-167 (1992).

[Alcouffe, 1977] R. E. Alcouffe, "Diffusion Synthetic Acceleration Methods for the Diamond-Differenced Discrete-Ordinates Equations," Nucl. Sci. Eng., 64, 344-355 (1977).

[Alcouffe, 1995] R. E. Alcouffe, R. S. Baker, F. W. Brinkley, D. R. Marr, R. D. O'Dell, and W. F. Walters, "DANTSYS: A Diffusion Accelerated Neutral Particle Transport Code System," LA-12969-M, LANL (1995).

[Anghel, 1987] V. N. P. Anghel, "Coarse-mesh Diffusion Acceleration Technique for Transport Calculation," Nucl. Sci. Eng., 97, 249-256 (1987).

[Aragones, 1986] J. M. Aragones, C. Ahnert, "A Linear Discontinuous Finite Difference Formulation for Synthetic Coarse-Mesh Few-Group Diffusion Calculation," Nucl. Sci. Eng., 94, 309 (1986).

[Brantley, 2000] P. S. Brantley, E. W. Larsen, "Variational Derivation of The Simplified P_3 Approximation," Joint Int. conf. on Mathematical Methods and Supercomputing for Nuclear Application, Saratoga, 1, 910-919 (1997).

[Brantley, 2000] P. S. Brantley, E. W. Larsen, "The Simplified P_3 Approximation," Nucl. Sci. Eng., 134, 1-21 (2000).

[Cavarec, 1994] C. Cavarec, J. F. Perron, D. Verwaerde, J. P. West, "Benchmark Calculations of Power Distribution within Assemblies," HT-12/94006 A, NEA/NSC/DOC 28, EDF (1994).

[Chao, 1998] Y.A. Chao, Y. A. Shatilla, T. Ida, Y. Tahara, "Challenges to Nodal Diffusion Methods for Cores with Mixed Oxide Fuel", Proc. Int. Conf. on the Physics of Nuclear Science and Technology, Long Island, NY, 9-14 (1998).

[Cho, 1996] N. Z. Cho, S. G. Hong, "CRX: A Transport Theory Code for Cell and Assembly Calculations Based on Characteristic Method," Proc. Int. Conf. on the Physics of Reactors, Mitto, Japan, 1A, 250 (1996).

[Cho, 2000] N. Z. Cho, G. S. Lee, S. G. Hong, C. K. Jo, K. T. Lee, "Whole-Core Heterogeneous Transport Calculations and Their Comparison with Diffusion Results," Trans. Am. Nucl. Soc., Winter Mtg., Washington D.C., 292-294 (2000).

[Downar, 2000] T. J. Downar, C. H. Lee, G. Jiang, "An Assessment of Advanced Nodal Methods for MOX Fuel Analysis in Light Water Reactors," PHYSOR 2000, May 7-12, Pittsburgh, Pennsylvania (2000).

[Duderstadt, 1979] J. J. Duderstadt, *Transport Theory*, A Wiley-Interscience Publication, (1979).
[Esser, 1993] P. D. Esser, K. S. Smith, "A Semianalytic Two-Group Nodal Model for SIMULATE-3, " Trans. Am. Nucl. Soc., San Diego, California, 68, 220-222 (1993).

[Fedon, 1999] C. Fedon-Magnaud, "Pin-by-Pin Transport Calculation with CRONOS Reactor Code, " Proc. of Mathematics and Computation, Reactor Physics and Environmental Analysis in Nuclear Applications, Madrid, Spain, 2, 1278-1287 (1999).

[Finnemann, 1977] H. Finnemann, F. Bennewitz, M. R. Wagner, "Interface Current Techniques for Multidimensional Reactor Calculations, " Atomkernenergie, 30, 123-128 (1977).

[Finnemann, 1979] H. Finnemann, H. Raum, "Nodal Expansion Method for the Analysis of Space-Time Effects in LWRs, " Proc. Specialists' Mtg. on Calculation of 3-D Rating Dist. in Operating Reactors, Paris, Nov. (1979).

[Fischer, 1981] H. D. Fischer, H. Finnemann, "The Nodal Integration Method – A Diverse Solver for Neutron Diffusion Problems, " Atomkernenergie, 39, 229 (1981).

[Hebert, 1991] A. Hebert, P. Benoist, "A Consistent Technique for the Global Homogenization of a Pressurized Water Reactor Assembly," Nucl. Sci. Eng., 109, 360 (1991).

[Hebert, 1993] A. Hebert, "A Consistent Technique for the Pin-by-Pin Homogenization of a Pressurized Water Reactor Assembly," Nucl. Sci. Eng., 113, 227-238 (1993).

[Henry, 1975] A. F. Henry, *Nuclear Reactor Analysis*, the MIT press (1975).

[Jiang, 2000] G. Jiang, "Multigroup Spatial Kinetics for MOX-fueled LWRs Based on Harmornic Analytic Nodal Method," PhD thesis, Purdue University (2000).

[Jiang, 2000] G. Jiang, "Mutigroup, Spatial Kinetics for MOX-Fueled LWRs Based on Harmornic Analytic Nodal Method, " Ph.D. Thesis, Purdue University, (2000).

[Joo, 1997] H. G. Joo, G. Jiang, T. J. Downar, "A Hybrid ANM/NEM Interface Current Technique for the Nonlinear Nodal Calculation, " Proc. ANS Conf. Math. Comp., Saratoga, NY, Oct., (1997).

[Joo, 1998] H. G. Joo, D. A. Barber, G. Jiang, T. J. Downar, "PARCS: Purdue Advanced Reactor Core Simulator," PU/NE-98-26 (1998).

[Kavenoky, 1980] A. Kavenoky, "The SPH Homogenization Method," Proc. Specialists' Mtg. Homogenization Methods in Reactor Physics, Lugano, Switzerland, IAEA-TECDOC-231, 181 (1980).

[Khattab, 1997] K. M. Khattab, "The Generalized P_N Synthetic Acceleration Method for Linear Transport Problems with Highly Anisotropic Scattering," Nucl. Sci. Eng., 125, 171-177 (1997)

[Koebke, 1980] K. Koebke, "A New Approach to Homogenization and Group Condensing," Proc. IAEA Specialists' Mtg. Homogenization Methods in Reactor Physics, Lugano, Switzerland, IAEA-TECDOC-231, 303 (1978).

[Kopp, 1963] H. J. Kopp, "Synthetic Method Solution of the Transport Equation," Nucl. Sci. Eng., 17, 65-74 (1963)

[Larsen, 1984] E. W. Larsen, "Diffusion-Synthetic Acceleration Methods for Discrete Ordinates Problems," Transp. Theory Stat. Phys., 13, 1-2, 107-126 (1984).

[Larsen, 1986] E. W. Larsen and W. F. Miller, Jr., "A Two-Step Acceleration Method for Transport Problems," Trans. Am. Nucl. Soc., 52, 416-417 (1986).

[Larsen, 1987] E.W. Larsen, J.E. Morel, W.F. Miller, Jr., "Asymptotic Solutions of Numerical Transport Problems in Optically Thick, Diffusive Regimes," J. Comp. Phys., 69, 283-324 (1987).

[Larsen, 1992] E. W. Larsen, "The Asymptotic Diffusion Limit of Discretized Transport Problems," Nucl. Sci. Eng., 112, 336-346 (1992).

[Larsen, 1996] E. W. Larsen and J. E. Morel and J. M. McGhee, "Asymptotic Derivation of the Multigroup P1 and Simplified PN equations with Anisotropic Scattering," Nucl. Sci. Eng., 123, 328-342 (1996)

[Lautard, 1991] J. J. Lautard, S. Loubiere, C. Fedonmagnaud, "Three Dimensional Pin by Pin Core Diffusion Calculation," Proc. Int. Topl. Mtg. Advances in Mathematics, Computations, and Reactor Physics, Pittsburgh, Pennsylvania, 2, 6.1 1-1 (1991).

[Lawrence, 1986] R. Lawrence, "Progress in Nodal Methods for the Solution of the Neutron Diffusion and Transport Equations, " Nucl. Sci. Eng., 123, 403-414 (1986).

[Lee, 2000] C. H. Lee, T. J. Downar, "Nonlinear Formulation for Multigroup Simplified P_3," Trans. Am. Nucl. Soc., Winter Mtg., Washington D.C., 297-299 (2000).

[Lefevbre, 1991] J. Lefevbre, et al., "Benchmark Calculations of Power Distributions within Assemblies," NEACRP-L-336, October (1991).

[Lewis, 1993] E. E. Lewis, *Computational Methods of Neutron Transport*, American Nuclear Society, Inc., (1993).

[Lewis, 1998] E. Lewis, G. Palmiotti, "A Finite Subelement Formulation of the Variational Nodal Method," ANS Trans., **7**9, 144 (1998).

[Mengelle, 1999] S. Mengelle, A. Nicolas, E. Richebois, "A New Power Reactor 3D Transport Calculation Scheme using the CRONOS2 and APOLLO2 Codes," Proc. Int. Conf. Mathematical and Computation, Reactor Physics and Environmental Analysis in Nuclear Applications, Madrid, 2, 1047-1054 (1999).

[Miller, 1986] W.F. Miller, Jr., E.W. Larsen, "Modified Diffusion Synthetic Acceleration Algorithms," Nucl. Sci. Eng. 93, 403 (1986).

[Miller, 1991] W. F. Miller, Jr., "An Analysis of the Finite Differenced, Even-Parity, Discrete Ordinates Equations in Slab Geometry," Nucl. Sci. Eng., 108, 247-266, (1991).

[Moon, 1999] K. S. Moon, N. Z. Cho, J. M. Noh, S. G. Hong, "Acceleration of the Analytic Function Expansion Nodal Method by Two-Factor Two-Node Nonlinear Iteration," Nucl. Sci. Eng., 132, 194-202 (1999).

[Morel, 1993] J. E. Morel and J. E. Dendy, Jr. and T. A. Wareing, "Diffusion-Accelerated Solution of the Two-Dimensional S_N Equations with Bilinear-Discontinuous Differencing," Nucl. Sci. Eng., 115, 304-319 (1993).

[Morel, 1994] J. E. Morel, J. M. McGhee, "A Fission-Source Acceleration Technique for Time-Dependent Even-Parity S_N Calculations, " Nucl. Sci. Eng., 116, 73-85 (1994).

[Morel, 1995] J. E. Morel and J. M. McGhee, "A Diffusion-Synthetic Acceleration Technique for the Even-Parity S_N Equations with Anisotropic Scattering," Nucl. Sci. Eng., 120, 147-164 (1995).

[Noh, 1993] J. M. Noh, N. Z. Cho. "A new diffusion nodal method based on analytic basis function expansion," Trans. Am. Nucl. Soc,, 69, 462-463 (1993).

[Noh, 1996] T. Noh, W. F. Miller, Jr., "The Even-Parity and Simplified Even-Parity Transport Equations in Two-Dimensional x-y Geometry," Nucl. Sci. Eng., 123, 38-56, (1996).
[Ott, 1989] K. O. Ott, W. A. Bezella, *Introductory Nuclear Reactor Statics*, American Nuclear Society (1989).

[Palmiotti, 1995] G. Palmiotti, E. Lewis, C. Carrico, "VARIANT: VARIational Anisotropic Nodal Transport for Multidimensional Cartesian and Hexagonal Geometry Calculation," ANL-95/40 (1995).

[Palmtag, 1997] S. Palmtag, "Advanced Nodal Methods for MOX Fuel Analysis," Ph.D thesis, MIT (1997).

[Palmtag, 1998] S. Palmtag, K. S. Smith, "Two-Group Spectral corrections for MOX Calculations," Proc. Int. Conf. Physics of Nuclear Science and Technology, Long Island, NY (1998).

[Rahnema, 1990] F. Rahnema, "Influence of Flux gradients on Local and Global Reactivities in BWRs," Proc. Int. Conf. Physics of Reactors: Operation, Design and Computation, Marseille, France (1990).

[Ramone, 1997] G. L. Ramone, M. L. Adams, P. F. Nowak, "A Transport Synthetic Acceleration Method for Transport Iterations," Nucl. Sci. Eng., 125, 257-283 (1997).

[Reed, 1971] W. H. Reed, "The Effectiveness of Acceleration Techniques for Iterative Methods in Transport Theory," Nucl. Sci. Eng., 45, 245-254 (1971).

[Ruggieri, 1995] J. M. Ruggieri, J. Y. Doriath, P. Gouriou, P. J. Finck, "Mixed Transport-Diffusion Method and Local Refinement Using Variational Nodal Method," Proc. Int. Conf., Mathematics and Computations, Reactor Physics, and Environmental Analyses, Portland, 2, 951-960 (1995).

[Ruggieri, 1996] J. M. Ruggieri, J. Y. Doriath, P. Gouriou, P. J. Finck, "Accounting for Strong Localized Heterogeneities and Local Transport Effect in Core Calculation," Nucl. Sci. Eng., 124, 82-88 (1996).

[Sartori, 1991] E. Satori, "Final Specification of Benchmark NEACRP-L-336," Letter NBD/91/1402/avt, OECD (1991).

[Shatilla, 1997] Y. Shatilla, "Westinghouse Advanced Nodal Code with Pin-power Reconstruction for MOX Applications, " Trans. Am. Nucl. Sci., Orlando, FL., 76, 179 (1997).

[Shin, 1998] U. Shin, W. F. Miller, Jr., "The Time-Dependent Simplified P_2 Equations: Asymptotic Analyses and Numerical Experiments, " Nucl. Sci. Eng., 128, 27-46 (1998).
[Shin, 1999] H. C. Shin, Y. H. Kim, Y. B. Kim, "One-Node Coarse-Mesh Finite Difference Algorithm for Fine-Mesh Finite Difference Operator," Trans. Am. Nucl. Soc., 81, 150-151 (1999).

[Smith, 1983] K. S. Smith, "Nodal Method Storage Reduction by Nonlinear Iteration," Trans. Am. Nucl. Soc., 44, 265 (1983).

[Smith, 1986] K. S. Smith, "Assembly Homogenization Techniques of Light Water Reactor Analysis," Prog. Nucl. Energy, 17, 303 (1986).

[Smith, 1986] K. S. Smith, "Multidimensional Nodal Transport Using the Simplified P_L Method," Trans. Am. Nucl. Soc., 52, 427-30 (1986).

[Smith, 1994] K. S. Smith, "Practical and Efficient Iterative Method for LWR Fuel Assembly Homogenization," Trans. Am. Nucl. Sci., 71, 238-241 (1994).

[Smith, 1997] K. Smith, "MOX Analysis Methods for SIMULATE-03, " Trans. Am. Nucl. Soc., Orlando, FL., 76, 181 (1997).

[Smith, 2000] M. Smith, N. Tsoulfanidis, E. Lewis, G. Palmiotti, T. Taiwo, "Whole-Core Neutron Transport Calculations Without Cross Section Homogenization," ICONE-8 (2000).

[Stamm'ler, 1983] R. Stamm'ler, *Methods of Steady-State Reactor Physics in Nuclear Design*, Academic Press, (1983).

[Taiwo, 1998] T. Taiwo, et al., "Development of Three-dimensional Transport Analysis Capability for LWR MOX Analysis," Trans. Am. Nucl. Soc., 79 (1998).

[Tatsumi, 1997] M. Tatsumi, A Yamamoto, "SCOPE: A Scalable and Flexible Parallel Algorithm Based on Object-Oriented Approach for Core Calculations," Proc. Joint Int. Conf. On Mathematical Methods and Supercomputing for Nuclear Applications, Saratoga, Spring, New York, 1, 191-202 (1997).

[Tatsumi, 1999] M. Tatsumi, A. Yamamoto, "Advanced Reactor Core Analysis by the Object-Oriented 3-D Fine Mesh Transport Calculation on Parallel/Distributed Environment, " Proc. of Mathematics and Computation, Reactor Physics and Environmental Analysis in Nuclear Applications, Madrid, Spain, 1288, Sept. (1999).

[Tatsumi, 2000] M. Tatsumi, A. Yamamoto, “A Study on Effects of Pin Cell Homogenization in an Actual Reactor Core Geomtry,” PHYSOR 2000, May 7-12, Pittsburgh, Pennsylvania (2000).

[Tomasevic, 1996] D. I. Tomasevic, E. W. Larsen, “The Simplified P_2 Approximation,” Nucl. Sci. Eng., 122, 309-325 (1996).

[Villarino, 1992] E. A. Villarino, R. J. Stamm'ler, A. A. Ferri, “HELIOS: Angularly Dependent Collision Probabilities,” Nucl. Sci. Eng., 112, 16-31 (1992).

[Yavuz, 1988] M. Yavuz, E. W. Larsen, “Diffusion Synthetic Acceleration for S_N Problems with Reflecting Boundaries,” Trans. Am. Nucl. Soc., 56, 305 (1988).

PART II: ADAPTIVE METHODS FOR THE VARIATIONAL NODAL METHOD

The variational nodal method has found substantial use in both diffusion theory and higher-order spherical harmonics approximations. It has been available in both two- and three-dimensional Cartesian and hexagonal geometries. However, the need sometimes arises for two-dimensional *R-Z* geometry calculations, particularly for scoping studies. The following describes the theoretical basis for the method implemented in the ANL code VARIANT.

1.0 Theory

The variational nodal method is a primal hybrid finite element representation of the even-parity form of the transport equation. In the hybrid formulation, the problem domain V is decomposed into subdomains V_ν (also called elements or nodes):

$$V = \sum_\nu V_\nu . \tag{1}$$

Within each node, the even-parity form of the transport equation is solved in space ($\vec{r}$) and angle ($\hat{\Omega}$):

$$-\hat{\Omega}\cdot\vec{\nabla}\sigma^{-1}\hat{\Omega}\cdot\vec{\nabla}\psi^+(\vec{r},\hat{\Omega})+\sigma\ \psi^+(\vec{r},\hat{\Omega}) = \sigma_s\int d\hat{\Omega}'\psi^+(\vec{r},\hat{\Omega}')+s(\vec{r}), \qquad \vec{r}\in V_\nu \tag{2}$$

where ψ^+ is the even parity flux component, σ and σ_s the total and scattering cross sections and *s* the group source. The odd-parity flux ψ^-, which is related to ψ^+ by

$$\hat{\Omega}\cdot\vec{\nabla}\psi^+(\vec{r},\hat{\Omega})+\sigma\psi^-(\vec{r},\hat{\Omega}) = 0, \qquad \vec{r}\in\Gamma_\nu \tag{3}$$

is defined only along the node interface Γ_ν as a Lagrange multiplier.

The functional for the variational nodal method is given as a superposition of nodal contributions:

$$F[\psi^+,\psi^-] = \sum_\nu F_\nu[\psi^+,\psi^-], \tag{4}$$

where

$$F_\nu[\psi^+,\psi^-]=\int_\nu dV\left\{\int d\Omega[\sigma^{-1}(\hat{\Omega}\cdot\vec{\nabla}\psi^+)^2+\sigma\psi^{+2}]-\sigma_s\phi^2-2\phi s\right\}+2\int_\nu d\Gamma\int d\Omega\hat{\Omega}\cdot\hat{n}\psi^+\psi^-, \quad (5)$$

and ϕ is the scalar flux. This functional must be stationary with respect to arbitrary variations $\tilde{\psi}^+$ and $\tilde{\psi}^-$ about the true solutions ψ^+ and ψ^-. Thus, we make the replacements $\psi^+\to\psi^++\delta\tilde{\psi}^+$ and $\psi^-\to\psi^-+\varepsilon\tilde{\psi}^-$ where δ and ε are small positive constants, and require the linear terms in δ and ε to vanish. Setting the linear term in δ to zero yields the weak form of Eq. (2):

$$\int_\nu dV\int d\Omega[\sigma^{-1}(\hat{\Omega}\cdot\vec{\nabla}\tilde{\psi}^+)(\hat{\Omega}\cdot\vec{\nabla}\psi^+)+\tilde{\psi}^+(\sigma\psi^+-\sigma_s\phi-s)]+\int_\nu d\Gamma\int d\Omega\hat{\Omega}\cdot\hat{n}\tilde{\psi}^+\psi^-=0, \quad (6)$$

and applying the divergence theorem yields

$$\int_\nu dV\int d\Omega\tilde{\psi}^+(-\hat{\Omega}\cdot\vec{\nabla}\sigma^{-1}\hat{\Omega}\cdot\vec{\nabla}\psi^++\sigma\psi^+-\sigma_s\phi-s)+\int_\nu d\Gamma\int d\Omega\hat{\Omega}\cdot\hat{n}\tilde{\psi}^+(\psi^-+\sigma^{-1}\hat{\Omega}\cdot\vec{\nabla}\psi^+)=0. \quad (7)$$

Clearly, Eq. (2) must be satisfied if the volume integral is to vanish for arbitrary $\tilde{\psi}^+$, and Eq. (3) must be met at the interface for the surface integral to vanish. The continuity conditions across nodal interfaces may be stated as follows. Since the Lagrange multiplier ψ^- and its variation $\tilde{\psi}^-$ are uniquely defined at the interface, two conditions are imposed. First, the surface integral in Eq. (7) imposes continuity on $\sigma^{-1}\hat{\Omega}\cdot\vec{\nabla}\psi^+$. Second, requiring the linear term in ε to vanish yields for each nodal interface, say between nodes V_ν and $V_{\nu'}$, a condition of the form

$$\int_\nu d\Gamma\int d\Omega\hat{\Omega}\cdot\hat{n}\tilde{\psi}^-(\psi^+-\psi'^+)=0, \quad (8)$$

since $\hat{n}_\nu=-\hat{n}_{\nu'}$. Thus ψ^+ must be continuous across the interface.

2.0 Cylindrical Coordinates (r, z)

The *R-Z* cylindrical coordinates system is shown in Figure 1, together with an angular-direction coordinates system used to define the particle direction $\hat{\Omega}$. In this system, a spatial point is defined by its (r, z) coordinate and

$$\hat{\Omega}=\Omega_r\hat{r}+\Omega_\omega\hat{\omega}+\Omega_z\hat{z}, \quad (9)$$

where

$$\Omega_r=(1-\mu^2)^{1/2}\cos\omega,$$
$$\Omega_\omega=(1-\mu^2)^{1/2}\sin\omega, \quad (10)$$

$$\Omega_z = \mu$$

with $\mu = \cos\theta$. The $\hat{\Omega}\cdot\vec{\nabla}$ may be determined by [O'Dell, 1987], [Lewis, 1984].

$$\hat{\Omega}\cdot\vec{\nabla} = \Omega_r \frac{\partial}{\partial r} - \frac{1}{r}\Omega_\omega \frac{\partial}{\partial \omega} + \Omega_z \frac{\partial}{\partial z}, \tag{11}$$

and the incremental angle is defined as $d\Omega = (4\pi)^{-1} d\mu d\omega$.

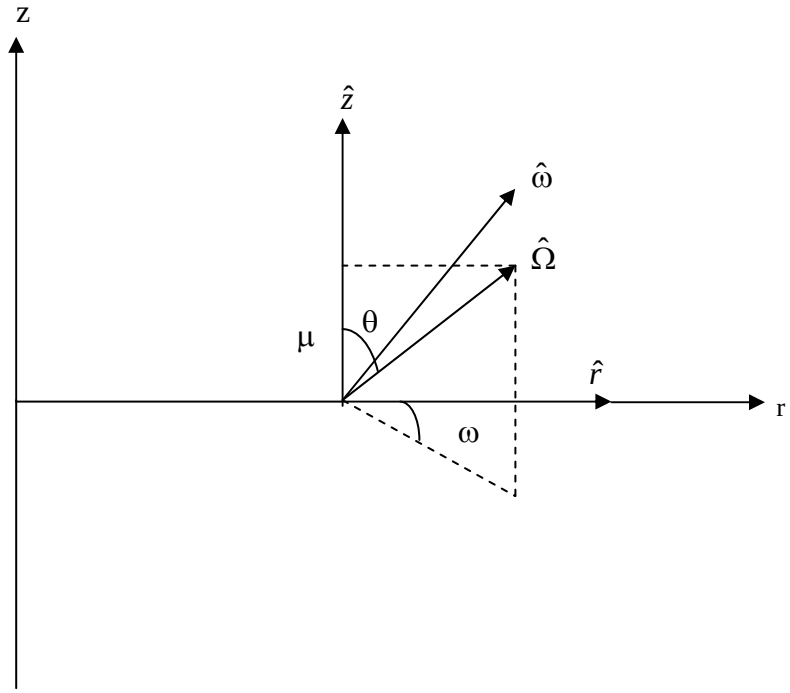

Fig. 1 **Cylindrical Coordinates**

3.0 Discretization

We begin by considering a rectangular node in *r, z* bounded on left and right by $r_l \le r \le r_r$ and on bottom and top by $z_b \le z \le z_t$ as shown in Figure 2. We expand the even-parity flux coefficients within the node as

$$\boldsymbol{\psi}^+(r,z,\hat{\Omega}) = \mathbf{g}^T(\hat{\Omega}) \otimes \mathbf{f}^T(r,z)\boldsymbol{\xi}_v. \qquad r_l \le r \le r_r, z_b \le z \le z_t \tag{12}$$

Here ⊗ denotes the Kronecker product, and $\mathbf{g}(\hat{\Omega})$ is vector of even-order spherical harmonics with M terms obey the orthonormal condition

$$\int d\Omega \mathbf{g}(\hat{\Omega})\mathbf{g}^T(\hat{\Omega}) = \mathbf{I}_M . \tag{13}$$

The spatial trial functions $\mathbf{f}(r,z)$ are complete polynomials. They are Legendre polynomials in z and also constructed to be orthogonal in r, so that

$$\frac{1}{V_v}\int_v dV \mathbf{f}(r,z)\mathbf{f}^T(r,z) = \mathbf{I}_I , \tag{14}$$

In R-Z geometry, $V_v = 2\pi(r_r^2 - r_l^2)(z_t - z_b)$ and

$$\int_v dV(\cdot) = 2\pi\int_{r_l}^{r_r} drr\int_{z_b}^{z_t} dz(\cdot) \tag{15}$$

The vector ξ_v in Eq, (12) contains the unknown coefficients.

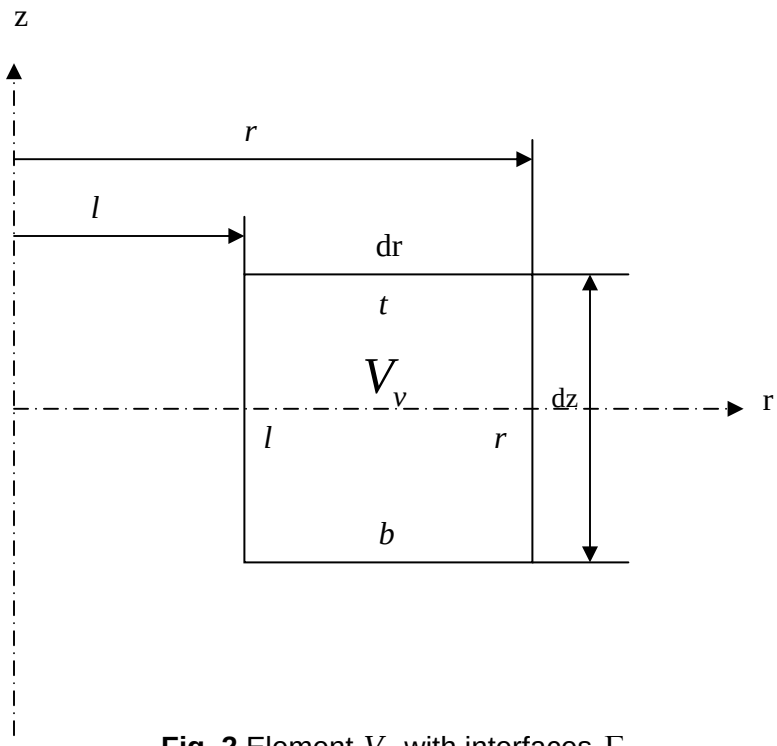

Fig. 2 Element V_v with interfaces Γ_v

Along the node interfaces, we make the expansions

$$\psi^{-}(\vec{r},\hat{\Omega}) = \mathbf{k}_{\gamma}^{T}(\hat{\Omega}) \otimes h_{\gamma}^{T}(z)\chi_{\gamma}^{'}, \qquad \vec{r} \in \Gamma_{r},\Gamma_{l}$$

and (16)

$$\psi^{-}(\vec{r},\hat{\Omega}) = \mathbf{k}_{\gamma}^{T}(\hat{\Omega}) \otimes h_{\gamma}^{T}(z)\chi_{\gamma}^{'}, \qquad \vec{r} \in \Gamma_{t},\Gamma_{b}$$

where $\mathbf{k}_{\gamma}(\hat{\Omega})$ is vector of odd-order spherical harmonics in which the angular coordinates have been rotated such that the polar angle, $\mu = \hat{\Omega} \cdot \hat{n}_{\gamma}$, is taken with respect to the surface normal. They obey the orthonormal conditions

$$\int d\Omega \mathbf{k}_{\gamma}(\hat{\Omega})\mathbf{k}_{\gamma}^{T}(\hat{\Omega}) = \mathbf{I}_{N}$$

and $\gamma = r,t,l,b$ (17)

$$\int d\Omega \mathbf{g}(\hat{\Omega})\mathbf{k}_{\gamma}^{T}(\hat{\Omega}) = \mathbf{0}$$

The spatial trial functions $\mathbf{h}_{\gamma}$ are set sets of orthogonal polynomials defined along the interfaces.

The source and the scalar flux may be approximated as

$$\mathbf{s} = \mathbf{w}\mathrm{s}(r,z) \tag{18}$$

and $r_{l} \le r \le r_{r}, z_{b} \le z \le z_{t}$

$$\phi(\vec{r}) = \mathbf{w}^{T} \otimes \mathbf{f}^{T}(r,z)\boldsymbol{\xi}_{\nu} \tag{19}$$

with $[\mathbf{w}]_{m} = \delta_{m1}$.

The nodal volumes corresponding to the response matrices will be toroids with rectangular cross sections in the r, z plane. The central nodes, however, are cylinders with three surfaces. The centerline symmetry condition that

$$\lim_{r \to o} \psi^{\pm}(\vec{r},\hat{\Omega}) = \psi^{\pm}(z,\theta) \tag{20}$$

requires that the central nodes contain two sets of trial functions for ψ^{+} and for ψ^{-} when spherical harmonics are employed. Only even functions in *r* are included in the spatial trial function sets for the Y_{l0} terms, which are independent of ω, causing the radial derivative vanishes at *r* = 0; only odd functions of *r* are included for the ω dependent Y_{lm}, $m \neq 0$ terms, causing them to vanish at the origin. With these stipulations, the singularities that would otherwise be

encountered in applying the operator of Eq. (11) are removed. Note, also, that unlike Cartesian geometry, each response matrix in the radial direction is unique, even though the cross sections and the widths and heights of the nodes are same.

4.0 Response Matrix Formulation

Response matrices are obtained from the foregoing space-angle trial functions by inserting them into Eqs. (4) and (5). This reduces the functional to the algebraic form:

$$F = \sum_{\nu} F_{\nu}[\boldsymbol{\zeta}_{\nu}, \boldsymbol{\chi}_{\nu}] \tag{21}$$

and

$$F_{\nu}[\boldsymbol{\zeta}_{\nu}, \boldsymbol{\chi}_{\nu}] = \boldsymbol{\zeta}_{\nu}^{T}\mathbf{A}_{\nu}\boldsymbol{\zeta}_{\nu} - 2\boldsymbol{\zeta}_{\nu}^{T}\mathbf{s}_{\nu} + 2\boldsymbol{\zeta}_{\nu}^{T}\mathbf{M}_{\nu}\boldsymbol{\chi}_{\nu}. \tag{22}$$

The matrix $\mathbf{A_V}$ is given as

$$\mathbf{A}_{\nu} = \sigma_{\nu}^{-1}\mathbf{H}_{kk'} \otimes \int_{\nu} dV\left(\nabla_{k}\mathbf{f}\right)\left(\nabla_{k'}\mathbf{f}^{T}\right) + \left(\sigma_{\nu}\mathbf{I}_{M} - \sigma_{s\nu}\mathbf{w}\mathbf{w}^{T}\right) \otimes V_{\nu}\mathbf{I}_{I}, \tag{23}$$

where repeated subscripts k or k' indicates summation with $k, k' = r, \omega, z$, and

$$\begin{aligned} \nabla_{r}\mathbf{f} &= \partial\mathbf{f}/\partial r, \\ \nabla_{\omega}\mathbf{f} &= \mathbf{f}/r, \\ \nabla_{z}\mathbf{f} &= \partial\mathbf{f}/\partial z. \end{aligned} \tag{24}$$

The incremental spatial volume is given by $dV = 2\pi r dr dz$.

Each of the elements of $\mathbf{A_V}$ is given in terms of integrals over known spatial or angular trial functions:

$$\mathbf{H}_{kk'} = \int d\Omega \Omega_{k}\Omega_{k'}\breve{\mathbf{g}}_{k}\breve{\mathbf{g}}_{k'}^{T}, \tag{25}$$

where

$$\begin{aligned} \breve{\mathbf{g}}_{r,z} &= \mathbf{g}, \\ \breve{\mathbf{g}}_{\omega} &= -\partial\mathbf{g}/\partial\omega. \end{aligned} \tag{26}$$

The source is

$$\mathbf{s}_{\nu} = \int_{\nu} dV \mathbf{s} \otimes \mathbf{f}. \tag{27}$$

The surface coefficients are partitioned according to the four interfaces:

$$\boldsymbol{\chi}_\nu = \begin{bmatrix} \boldsymbol{\chi}'_r \\ \boldsymbol{\chi}'_t \\ \boldsymbol{\chi}'_l \\ \boldsymbol{\chi}'_b \end{bmatrix} \tag{28}$$

The $\mathbf{M}_\nu$ matrix is then given as

$$\mathbf{M}_\nu = \left[\mathbf{M}'_r, \mathbf{M}'_t, \mathbf{M}'_l, \mathbf{M}'_b\right], \tag{29}$$

$$\mathbf{M}'_\gamma = \mathbf{E}_\gamma \otimes \mathbf{D}_\gamma, \qquad \gamma = r,t,l,b \tag{30}$$

where

$$\vec{\mathbf{E}}_\gamma = \int d\Omega \hat{\Omega} \cdot \hat{n}_\gamma \mathbf{g}(\hat{\Omega}) \mathbf{k}_\gamma^T(\hat{\Omega}), \tag{31}$$

and

$$\begin{aligned} \mathbf{D}_\gamma &= 2\pi r_\gamma \int_{z_b}^{z_t} dz \mathbf{f}(r_\gamma, z) \mathbf{h}_\gamma^T(z), \qquad \gamma = r,l \\ \mathbf{D}_\gamma &= 2\pi \int_{r_l}^{r_r} dr r \mathbf{f}(r, z_\gamma) \mathbf{h}_\gamma^T(r). \qquad \gamma = t,b \end{aligned} \tag{32}$$

We may now obtain a set of algebraic equations by requiring the discretized functional to be stationary. To examine arbitrary variations about the solutions, we make the replacements $\boldsymbol{\zeta}_\nu \to \boldsymbol{\zeta}_\nu + \delta\tilde{\boldsymbol{\zeta}}_\nu$ and $\boldsymbol{\chi}_\nu \to \boldsymbol{\chi}_\nu + \delta\tilde{\boldsymbol{\chi}}_\nu$ in Eqs. (21) and (22). Requiring the linear term in δ to vanish yields

$$\mathbf{A}_\nu \boldsymbol{\zeta}_\nu + \mathbf{M}_\nu \boldsymbol{\chi}_\nu = \mathbf{s}_\nu. \tag{33}$$

Requiring the linear term in ε to vanish imposes continuity across nodal interfaces of the moments defined by

$$\boldsymbol{\psi}_\nu = \mathbf{M}_\nu^T \boldsymbol{\zeta}_\nu. \tag{34}$$

We may solve Eq. (33) for $\boldsymbol{\zeta}_\nu$,

$$\boldsymbol{\zeta}_\nu = \mathbf{A}_\nu^{-1} \mathbf{s}_\nu - \mathbf{A}_\nu^{-1} \mathbf{M}_\nu \boldsymbol{\chi}_\nu, \tag{35}$$

and combine the result with Eq. (34) to obtain

$$\boldsymbol{\psi}_\nu = \mathbf{M}_\nu^T \mathbf{A}_\nu^{-1} \mathbf{s}_\nu - \mathbf{M}_\nu^T \mathbf{A}_\nu^{-1} \mathbf{M}_\nu \boldsymbol{\chi}_\nu. \tag{36}$$

At this point, we have written the even-parity flux moments $\boldsymbol{\psi}_\nu$ at the node interface in terms of the source and the odd-parity interface moments $\boldsymbol{\chi}_\nu$, while imposing the continuity of both of

these moments between neighboring nodes. The final step is to transform variables such that Eq. (36) may be written in terms of a response matrix. Introducing the partial current-like variables

$$\mathbf{j}_\nu^{\pm} = \tfrac{1}{4}\boldsymbol{\psi}_\nu \pm \tfrac{1}{2}\boldsymbol{\chi}_\nu \tag{37}$$

into Eq. (39) and (40) then yields response matrix equation for each node:

$$\mathbf{j}_\nu^{+} = \mathbf{R}_\nu \mathbf{j}_\nu^{-} + \mathbf{B}_\nu \mathbf{s}_\nu, \tag{38}$$

where $\mathbf{R}_\nu = \left(\tfrac{1}{2}\mathbf{M}_\nu^T \mathbf{A}_\nu^{-1}\mathbf{M}_\nu + \mathbf{I}\right)^{-1}\left(\tfrac{1}{2}\mathbf{M}_\nu^T \mathbf{A}_\nu^{-1}\mathbf{M}_\nu - \mathbf{I}\right)$ and $\mathbf{B}_\nu = \left(\tfrac{1}{2}\mathbf{M}_\nu^T \mathbf{A}_\nu^{-1}\mathbf{M}_\nu + \mathbf{I}\right)^{-1}\tfrac{1}{2}\mathbf{M}_\nu^T \mathbf{A}_\nu^{-1}$.

5.0 Results I: VARIANT Steady-State

The *R-Z* formalism is being implemented as a modification of the multigroup VARIANT code at Argonne National Laboratory, for both diffusion theory and higher-order spherical harmonics calculations. Both fixed source and eigenvalue options are included. To test the fixed source capability the well-known Iron-water problem [Gelbard, 1972] has been recast from *X-Y* to *R-Z* geometry, with all dimensions and cross sections remaining the same. Figures 3 and 4 show P_1 and P_3 results close to the vacuum boundaries. Fine meshes with $\Delta r = \Delta z = 1$ cm, and a coarse mesh, with $\Delta r = \Delta z = 3$ cm, are presented. For comparison, fine mesh x-y calculations are also included. The substantial transport effects are, as expected, present in *R-Z* as well as *X-Y* geometry.

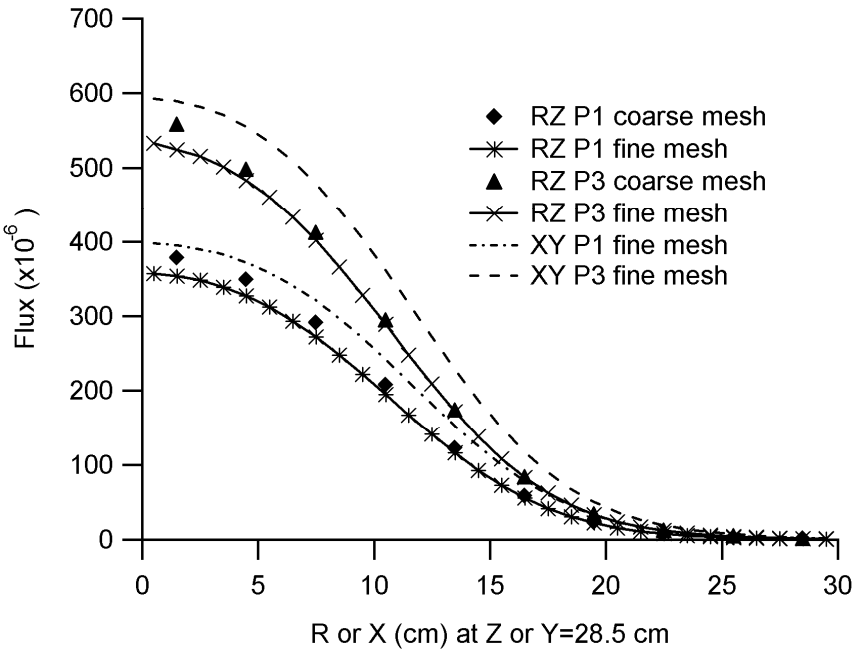

Fig. 3 Flux distribution close to the vacuum boundary on the top for the Iron-water problem

To examine spatial truncation errors, we utilize two-group eigenvalue problems. Table 1 provides P_1 eigenvalue results using two group MOX fuel and water cross sections. The core is 40 cm in radius and 80 cm in height surrounded by radial and axial reflectors 20 cm thick. A reflected boundary condition is used to reduce the modeling to the upper half of the core. The eigenvalue is tabulated vs. both *h* and *p* refinement. Aside from the coarsest nodes, the accuracy increases faster with *p* refinement (i.e. increasing the polynomial order in the interface approximation) than in reducing the mesh size in *h* refinement. Moreover, both CPU time and memory requirements increase substantially with mesh size reduction, but much less so with increased polynomial order.

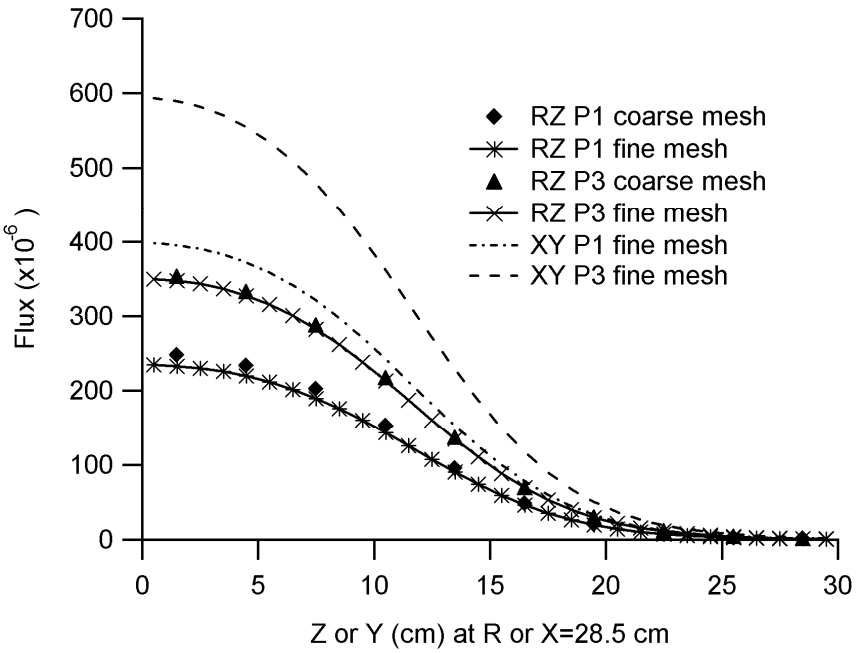

Fig. 4 Flux distribution close to the vacuum boundary on the right for the Iron-water problem

Interface / Δr & Δz	Flat	Linear	Quadratic
10cm	0.95450 (1.21×10^{-1}%)	0.95349 (1.47×10^{-2}%)	0.95349 (1.47×10^{-2}%)
4cm	0.95351 (1.68×10^{-2}%)	0.95335 (0.00%)	0.95335 (0.00%)
2cm	0.95339 (3.15×10^{-3}%)	0.95335 (0.00%)	0.95335 (0.00%)
1cm	0.95336 (1.05×10^{-3}%)	0.95335 (0.00%)	0.95335 (0.00%)

Table 1 Comparison of *h*-refinement and *p*-refinement for Two-Region Eigenvalue Problem

6.0 Results II: VARIANT and PARCS TRANSIENT

As shown in Fig. 5, a three-dimensional 3x3 fuel assembly mini core was constructed using data from the OECD/NEA and U.S. NRC PWR MOX/UO2 core transient benchmark [Kozlowski, 2003]. The mini-core consists of 4 MOX and 5 UOX assemblies, and 22 planes including top/bottom reflectors. The homogenized 2-/4-/8-group cross sections are provided for assembly-wise and/or pin-wise meshes in a PMAXS format. A superprompt critical reactivity insertion is simulated by a control rod which is inserted in the center UOX fuel assembly and fully ejected within 0.1 seconds.

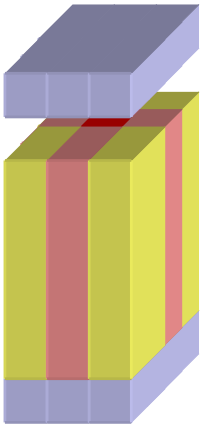

Fig. 5 3x3 Fuel Assembly Mini-Core.

State steady calculations are summarized in Table 2. The ANL code VARIANT [Palmiotti, 1994] is used as a reference solution. The transient power is shown in Fig. 6 which shows consistency between the higher order PARCS and VARIANT results.

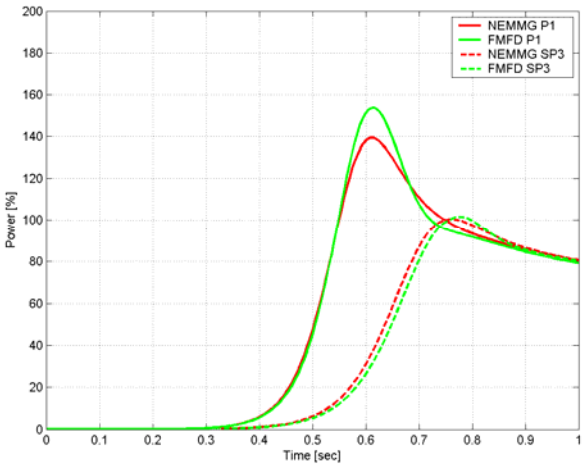

Fig. 6 Rod Ejection Transient

7.0 List of References for PART II

[O'Dell, 1987] R. Douglas O'Dell and Raymond E. Alcouffe, "Transport Calculation for Nuclear Analyses: Theory and Guidelines for Effective Use of Transport Codes," Los Alamos National Laboratory LA-10983-MS, 1987

[Lewis, 1984] E. E. Lewis and W. F. Miller, Jr., "Computational Methods of Neutron Transport," John Wiley & Sons, New York, 1984

[Gelbard, 1972] E. M. Gelbard, "Argonne Code Center: Benchmark Problem Book," ANL-7416 Supplement 1 Mathematics and Computers, Argonne National Laboratory, 1972

[Palmiotti, 1995] G. Palmiotti, E. E. Lewis & C. B. Carrico, "VARIANT: VARIational Anisotropic Nodal Transport for Multidimensional Cartesian and Hexagonal Geometry Calculation," Argonne National Laboratory ANL-95/40, 1995.

[Downar, 2002] T. J. Downar, et. al., "PARCS: Purdue Advanced Reactor Core Simulator," PHYSOR 2002, Seoul, Korea, Oct. 7-10 (2002).

[Lee, 2002] Chang-Ho Lee, Tomasz Kozlowski, and Thomas J. Downar, "Analysis of Control Rod Ejection Accident in MOX and MOX/UOX Cores with Time-Dependent Multigroup Pin-by-Pin SP_3 Methods," PHYSOR 2002, Seoul, Korea (2002).

[Brantley, 2000] L. S. Brantley, E. W. Larsen, "The Simplified P_3 Approximation," *Nucl. Sci. Eng.*, **134**, 1-21 (2000).

[Lee, 2004a] D. Lee, T.J. Downar, and Y. Kim, "A Nodal and Finite Difference Hybrid Method for Pin-by-Pin Heterogenous Three-Dimensional Light Water Reactor Diffusion Calculations," *Nucl. Sci. Eng.*, **146**, 319-339 (2004).

[Lee, 2001] Hyun Chul Lee, "Unified Nodal Method for Static and Transient Analysis of Power Reactor," PhD Thesis, Seoul National University, Seoul Korea (2001).

[Lee, 2004b] D. Lee, T. Downar, C. Lee, and H.C. Lee, "A 2D/1D approach for Multi-Group Three-dimensional Simplified P3 Analysis Based on Unified Nodal Method in PARCS," in preparation.

[Yamamoto, 2004] Akio YAMAMOTO, Masahiro TATSUMI, Yasunori KITAMURA, and Yoshihiro YAMANE, "Improvement of the SPH Method for Multi-assembly Calculations," *PHYSOR 2004*, Chicago, Illinois, April 25-29 (2004).

[Kozlowski, 2004] Tomasz Kozlowski, Deokjung Lee, and Thomas J. Downar, "The Use of an Artificial Neural Network for On-Line Prediction of Pin-Cell Discontinuity Factors in PARCS," *PHYSOR 2004*, Chicago, USA, April 25 - 29 (2004).

[Yamamoto, 2004] Akio Yamamoto, "A Simple and Efficient Control Rod Cusping Model For Three-Dimensional Pin-by-Pin Core Calculations," *Nucl. Tech.*, **145**, pp.11-17 (2004).

[Kozlowski, 2003] Tomasz Kozlowski and Thomas J. Downar, "OECD/NEA AND U.S. NRC PWR MOX/UO2 Core Transient Benchmark," Final Specifications, Revision 2, December 2003.

[Finnemann, 1991] H. FINNEMANN and A. GALATI, "NEACRP 3-D LWR Core Transient Benchmark," NEACRP-L-335, October 1991.

[Alsaed, 1998] A. A. ALSAED and M. L. ADAMS, "Disposition of Weapons-Grade Plutonium Westinghouse Reactors," ANRCP-1998-1, March 1998, http://www.pu.org.

[Akimushkin, 2002] S. AKIMUSHKIN, et. al., "Valication of a Pin-by-Pin Heterogeneous Method Agains LWR MOX Benchmarks," PHYSOR 2002.

[Joo, 2002] H. G. JOO, et. al., "Dynamic Implementation of the Equivalence Theory in the Heterogeneous Whole Core Transport Calculation," PHYSOR 2002.

Plans for Next Quarter: Project has been completed

Patents: N/A.

Publications/Presentations:

[Lee, 2002] Chang-Ho Lee, Tomasz Kozlowski, and Thomas J. Downar, "Analysis of Control Rod Ejection Accident in MOX and MOX/UOX Cores with Time-Dependent Multigroup Pin-by-Pin SP_3 Methods," PHYSOR 2002, Seoul, Korea (2002).

[Lee, 2004a] D. Lee, T.J. Downar, and Y. Kim, "A Nodal and Finite Difference Hybrid Method for Pin-by-Pin Heterogenous Three-Dimensional Light Water Reactor Diffusion Calculations," *Nucl. Sci. Eng.*, **146**, 319-339 (2004).

[Lee, 2005b] D. Lee, T. Downar, C. Lee, and H.C. Lee, "A 2D/1D approach for Multi-Group Three-dimensional Simplified P3 Analysis Based on Unified Nodal Method in PARCS," in preparation.

Milestone Status Table:

Task / Milestone Description	Planned Completion	Actual Completion	Comments
1. Adaptive Methods	6/02	7/02	
2. Error Estimation	3/03	4/03	
3. Preconditioner	6/03	6/03	
4. Code Integration	9/03		Delayed while method was reformulated
5. Benchmarking	1/04	8/04	
6. Code Verification	6/04	10/04	
7. Preparation of Final Report		8/05	**Completed**